Mid-slope Site U1380[1]

R.N. Harris, A. Sakaguchi, K. Petronotis, A.T. Baxter, R. Berg, A. Burkett, D. Charpentier, J. Choi, P. Diz Ferreiro, M. Hamahashi, Y. Hashimoto, K. Heydolph, L. Jovane, M. Kastner, W. Kurz, S.O. Kutterolf, Y. Li, A. Malinverno, K.M. Martin, C. Millan, D.B. Nascimento, S. Saito, M.I. Sandoval Gutierrez, E.J. Screaton, C.E. Smith-Duque, E.A. Solomon, S.M. Straub, W. Tanikawa, M.E. Torres, H. Uchimura, P. Vannucchi, Y. Yamamoto, Q. Yan, and X. Zhao[2]

Chapter contents

[1] Harris, R.N., Sakaguchi, A., Petronotis, K., Baxter, A.T., Berg, R., Burkett, A., Charpentier, D., Choi, J., Diz Ferreiro, P., Hamahashi, M., Hashimoto, Y., Heydolph, K., Jovane, L., Kastner, M., Kurz, W., Kutterolf, S.O., Li, Y., Malinverno, A., Martin, K.M., Millan, C., Nascimento, D.B., Saito, S., Sandoval Gutierrez, M.I., Screaton, E.J., Smith-Duque, C.E., Solomon, E.A., Straub, S.M., Tanikawa, W., Torres, M.E., Uchimura, H., Vannucchi, P., Yamamoto, Y., Yan, Q., and Zhao, X., 2013. Mid-slope Site U1380. *In* Harris, R.N., Sakaguchi, A., Petronotis, K., and the Expedition 344 Scientists, *Proc IODP,* 344: College Station, TX (Integrated Ocean Drilling Program). doi:10.2204/iodp.proc.344.106.2013
[2] Expedition 344 Scientists' addresses.

Background and objectives

A primary objective of Integrated Ocean Drilling Program (IODP) Expedition 344 was to understand the processes that generate earthquakes along the subduction thrust at erosive plate margins. Fundamental to this objective is determining the nature of the upper plate seaward of the seismogenic zone. Site U1380 is located in the upper plate seaward of the seismogenic zone.

Site U1380 is located on the middle slope of the Costa Rica margin along seismic Line BGR99-7 at common midpoint 2350 (Figs. F1, F2). At Site U1380, the margin consists of a 550 m thick section of slope sediments overlying upper plate framework rock. This site was selected for a number of reasons. First, interplate earthquakes and geodetic measurements indicate that this site is seaward of the updip extent of seismicity and that the plate interface is not locked. Second, the seismic section shows that this site is above the seaward edge of high-amplitude landward-dipping reflectors. Third, this site is on the flank of a local high in framework rock that minimizes drilling time through the overlying sediment. Hole U1380A was drilled during IODP Expedition 334 as an alternative to Site U1378 when drilling conditions prevented further progress. During Expedition 334, at ~480 mbsf, poor drilling conditions necessitated terminating Hole U1380A prior to reaching the framework rock (Expedition 334 Scientists, 2012c). The primary goals for revisiting this site were to determine the nature, composition, and physical properties of the upper plate framework rock; to understand the nature of the landward-dipping seismic reflectors; and to estimate the state of stress.

Operations

Transit to Site U1380

After an 11.4 nmi transit from Site U1381, the vessel stabilized over Site U1380 at 1715 h on 27 October 2012. The initial position was at the coordinates of Hole U1380A (8°35.9976′N, 84°4.4032′W), which was drilled during Expedition 334 in 2011 (proposed Site CRIS-10A). The vessel was then repositioned 20 m east of those coordinates. The position reference used for dynamic positioning was a combination of GPS signals and an acoustic positioning beacon, which was deployed at 1730 h on 27 October and recovered at 2310 h on 13 November.

doi:10.2204/iodp.proc.344.106.2013

Hole U1380B

Hole U1380B was established to conduct a jet-in test to determine the length of 16 inch casing that could be jetted into the formation with a reentry cone. Upon arrival, the jet-in bottom-hole assembly (BHA) was assembled with a 14¾ inch bit and lowered to 312.8 meters below rig floor (mbrf). The subsea camera was deployed, and the seafloor was tagged with the drill string to verify the water depth. Hole U1380B was spudded at 0118 h on 28 October 2012 (8°35.9952′N, 84°4.3908′W; 502.7 m water depth). After 11.25 h, the 14¾ inch bit had been jetted into the formation 50 m. The BHA was then pulled out of the hole, and the bit cleared the seafloor at 1310 h on 28 October, ending Hole U1380B.

Hole U1380C

The reentry cone was moved to the center of the moonpool, and a 48 m long string of 16 inch casing was assembled. The casing string was then picked up with the Dril-Quip running tool and lowered and latched into the reentry cone centered in the moonpool. Once the reentry system and casing were assembled (Fig. **F3**), the stinger that is run below the casing running tool was assembled and run inside the casing. The Dril-Quip running tool was made up and inserted into the casing hanger, and the assembly was lowered to the seafloor. The top drive was picked up, and the 16 inch casing string was jetted into the formation. Hole U1380C was spudded at 1145 h on 29 October 2012 (8°35.9879′N, 84°4.3918′W; 502.7 m water depth). After 9.5 h of jetting operations, the reentry cone landed on the seafloor. The subsea camera system was run to bottom, and the running tool was released and lifted clear of the reentry cone. The bit was pulled out of the hole, clearing the rig floor at 0155 h on 30 October. The next step was to drill a hole for the 10¾ inch casing, so a 14¾ inch drilling assembly was made up and run into the hole. The subsea camera system was deployed, the top drive was picked up, and after 20 min of positioning the vessel, Hole U1380C was reentered at 0550 h on 30 October.

Drilling began at 48 meters below seafloor (mbsf) and continued over the next 22.8 h to a total depth of 438 mbsf. Two high-viscosity mud sweeps were pumped, and the hole was checked for fill. After finding 3 m of fill, the hole was washed back to bottom and another high viscosity mud sweep was pumped. After cleaning the hole as much as practical, a wiper trip was performed. The bit was pulled back with the top drive to 260 mbsf. Excessive overpull and high torque were experienced while the bit was between 338 and 396 mbsf. The top drive was then set back, and the bit was pulled back to just above the casing shoe. The bit was then lowered back into the open hole section, and a hard tag (weight loss) was experienced at 289 mbsf. The drill string was pulled back 20 m, and the top drive was picked up. The hole was then washed and reamed back to bottom, where 3 m of fill was encountered.

After reaching total depth, two 50 bbl mud sweeps were pumped. Given the hole problems experienced on the first wiper trip, we conducted another wiper trip. The top drive was left in place, and the bit was pulled back to 289 mbsf. Overpull of 10,000–15,000 lb was experienced in the same interval as before. After reaching 289 mbsf, the top drive was set back and the bit was pulled back to just above the casing shoe. While running back to bottom, the first hard tag was experienced at 337 mbsf. The drill string was pulled back, and the top drive was picked up. The hole was then reamed back to bottom (438 mbsf), where 25 m of hard fill was encountered. The fill could not be washed through and had to be drilled and circulated out. Another two high-viscosity mud sweeps were pumped, and another wiper trip was performed. The same tight hole conditions were experienced between ~395 and 340 mbsf. The top drive was set back, and the pipe was tripped back to just above the 16 inch casing shoe. Running back into the hole with the bit, a hard tag was experienced again at 347 mbsf. The top drive was again picked up, and an attempt was made to jet into the hole without rotation. At 366 mbsf, 40,000 lb of overpull and 500 A of torque were experienced. We continued to run back in the hole with and without rotation to 425 mbsf. At that point, we decided to attempt to stabilize the formation with cement from 396 mbsf to ~50 m higher. Sixty-five barrels of cement were mixed, pumped, and displaced at 2045 h on 1 November. After pumping the cement, the drill string was pulled up above the theoretical top of the cement and 2.5 times the volume of the drill sting was pumped with seawater to flush any remaining cement from the drill string. The pipe was then pulled all the way back to just above the casing shoe and circulated again, this time with three times the volume of the drill string at 100 spm.

After waiting on the cement to cure for 9.8 h, we attempted to run back into the hole with the bit. Tight hole conditions were noted at 153–163 and 175 mbsf. At 175 mbsf, the top drive was picked up and we washed and reamed back to 347 mbsf, where we encountered the top of the cement plug. The cement plug was drilled out from 347 to 395 mbsf, and the rest of the hole was reamed back to 438 mbsf. Two high-viscosity mud sweeps were pumped at the bottom of the hole, and the drill string was pulled back to 328 mbsf with no pump and no rotation. We then washed down with no rotation from 328 to 406 mbsf.

The maximum weight on bit experienced was 10,000–15,000 lb. At 406 mbsf, we began washing and rotating back to bottom. Two 50 bbl high-viscosity mud sweeps were pumped to clean up the hole, and the hole was displaced with 225 bbl of heavy (10.5 ppg) mud. We then pulled out of the hole with the top drive, and the drill string was pulled clear to surface to run casing. The 14¾ inch bit was laid out, and the Dril-Quip casing running tool was made up to the casing hanger and one stand and set back in the derrick. The drill floor was rigged up for running casing, and a short safety meeting with the crew took place. The 10¾ inch casing length that was selected was 406 m. This was made up of 29 joints of 10¾ inch casing, one shoe joint, and one pup joint on the 10¾ inch casing hanger. The 10¾ inch casing string was landed on the moonpool doors and secured, and the running tool was released. The casing stinger was then made up and spaced out. The running tool and the remainder of the casing BHA were made up, and the casing was run to just above the seafloor. The subsea camera was run down the casing string.

After positioning the vessel for reentry, Hole U1380C was reentered at 0745 h on 4 November. The subsea camera was recovered, and the casing was run into the hole to 179.3 mbsf, where tight hole conditions were experienced. The casing was pulled back to 150.3 mbsf, and the top drive was picked up and installed. Over the next 14 h, the casing was slowly worked into the open hole by applying weight while pumping with the top drive. The final depth of the casing shoe was within 18 m of the landing depth when the casing refused to advance any further. The casing eventually became stuck, and it required ~120,000 lb of overpull to free the casing from the formation. The casing was then pulled back to the surface, clearing the top of the reentry cone at 0035 h on 5 November. Using the casing elevator, the casing was landed on the moonpool doors at 0110 h. The running tool was released from the casing, and we made a decision to try to reenter the hole with a 9⅞ inch tricone bit and an underreamer assembly to clean out the hole. The idea was to not disassemble the casing while the hole was being prepared, which would allow us to run the casing quickly after the hole was cleaned to depth. The 9⅞ inch bit and the underreamer were picked up and deployed through the casing string in the moonpool. The casing was picked up with the running tool to deploy the subsea camera. The camera was then run to bottom, and the vessel was positioned for reentry. Hole U1380C was quickly reentered, and the bit was run to just below the bottom of the 16 inch casing. The top drive was picked up and reaming began from 51.4 mbsf.

At 216.7 mbsf, at 0045 h on 6 November, the driller experienced erratic drilling torque and then observed the loss of that erratic torque while adjusting his drilling parameters. A later review of the rig instrumentation data clearly showed not only erratic torque but an increase of weight in the hook load of ~40,000 lb. The driller reacted by changing his drilling parameters to try to find the cause of the erratic torque. After shutting the pumps down completely, the erratic torque vanished, as did the additional hook load weight. Restarting the pumps again with rotation resulted in not even the reaming torque that was present before the event. At that time, the tool pusher and the driller assumed that the underreamer had stopped functioning. The decision was made to pull out of the hole and inspect the drilling assembly. The bit cleared the reentry cone at 0229 h and was pulled to the rig floor at 0440 h. The bit and the underreamer appeared intact, with no obvious signs of damage. A test of the underreamer failed to energize the arms, and we made a decision to pick up a second underreamer and go back to reaming the hole to bottom.

The drilling BHA with the new underreamer was picked up and run to 371.2 mbrf. At that time, the casing hanger was picked up with the running tool to deploy the subsea camera. As the tool pusher began running the camera to bottom, he discovered that the casing string had parted just below the vessel. We realized that the erratic drilling parameters observed earlier in the day had been caused by the casing string parting and free falling into the hole. The casing reentered the reentry cone, made its way down the drill string, and landed on the rotating underreamer arms at 216.7 mbsf. The additional weight of the casing string caused the erratic torque when the casing shoe landed on the rotating underreamer arms. When the driller shut down the mud pumps, the underreamer arms closed and the casing continued its downhole trip. The subsea camera was run down the drill pipe to survey the possible damage to the reentry system and casing. The expectation was that the casing would have come to a stop with a portion of the casing extending out from the reentry cone. The initial underwater survey indicated that the casing had continued its downward journey and that the entire casing string was inside the existing hole.

After discussions on board, we decided to reenter the hole and determine if the hole was salvageable. The vessel was positioned for reentry, and Hole U1380C was reentered at 1357 h on 6 November. The camera was pulled to the surface, and careful observation near the surface indicated that only one complete joint plus the casing hanger (15.2 m total length) remained hanging below the ship. By subtracting that from the full length of the casing string we

determined that 390.6 m of casing had landed inside the hole. The only question remaining was the condition of the casing. It was quickly determined that the top of the 10¾ inch casing string was very likely inside the 16 inch casing string. The drill bit was lowered without any significant resistance from inside the 16 inch casing to 336 mbsf. At that point, we applied 30,000–40,000 lb of weight, but no downward progress resulted from our efforts. After discussions with drilling and science staff, we decided to pull out of the hole and pick up a coring BHA with a rotary core barrel (RCB) bit. The subsea camera was deployed, and the hole was reentered at 0900 h on 7 November. The bit encountered a possible tag at ~8 mbsf, which we interpreted to be the top of the casing. If confirmed, the bottom of the casing should be found at ~398 mbsf; if so, the casing would be covering the problematic zone in the hole. The bit was lowered to 336 mbsf, and drilling proceeded carefully from 336 to 438 mbsf without problems. The hole was then circulated clean, the wash core barrel was pulled, and an RCB core barrel was dropped. RCB coring commenced at 1745 h on 7 November and continued without interruption until 2400 h on 10 November, reaching a total depth of 800 mbsf. Nonmagnetic RCB core barrels were used starting with Core 344-U1380C-11R. In an effort to improve recovery, we started cutting and pulling half cores with Core 25R. This dramatically improved core recovery, and coring by half cores continued. The total cored interval in Hole U1380C was 362.0 m with 202.4 m recovered for an overall recovery of 56% (Table T1). At the conclusion of coring, the hole was swept clean with a 40 bbl sweep of high-viscosity mud.

In preparation for logging, the drill string was pulled out of the hole to a depth just above the seafloor, clearing the reentry cone at 0720 h on 11 November. The subsea camera was deployed, and the bit was successfully released on the seafloor at 0855 h. Hole U1380C was reentered at 1005 h, the subsea camera was recovered, and the end of the drill pipe was placed at 336 mbsf. After holding a safety meeting on the rig floor, the triple combination (triple combo)–Ultrasonic Borehole Imager (UBI) logging string was rigged up and run into the hole at 1530 h. However, the logging tools were unable to advance past 398 mbsf, which coincided with the estimated depth of the casing shoe. The tools were pulled from the hole, and the drill pipe was advanced to 467 mbsf without difficulty. The drill pipe was then pulled back to 394 mbsf, and a reconfigured triple combo string without the UBI was picked up and run into the hole at 2310 h. This time the logging tools made it to 458 mbsf before encountering an obstruction. A review of the logs showed that the casing might have slipped down inside the hole (Fig. F4). The logging tools were pulled back to the surface, and the hole was checked to 496 mbsf with the end of the pipe, where an obstruction was encountered. The pipe was pulled back to 457 mbsf with 20,000 lb of overpull. In order to better clean the hole for logging, the drill string was pulled all the way out of the hole, reaching the rig floor at 0725 h on 12 November. A BHA with a used RCB bit was deployed. The subsea camera was deployed, and Hole U1380C was reentered at 1015 h. The drill pipe was advanced to 65 mbsf, where it encountered a slight obstruction. This depth was recorded as the new possible top of the 10¾ inch casing string, which would place the casing shoe at 455 mbsf. The pipe was eventually run in the hole to 496 mbsf, and the hole was washed down from 496 to 781 mbsf in 15.75 h. The hole was swept clean with a 40 bbl sweep of high-viscosity mud, and a second sweep of 20 bbl was pumped. The RCB bit was released in the hole at 768 mbsf, and the hole was again displaced with 230 bbl of heavy mud. In preparation for logging, the end of the drill string was placed at 443 mbsf. The triple combo logging tool string was rigged up for the third time and run into the hole at 1310 h on 13 November. However, the logging tools encountered a similar obstruction as before at 462 mbsf. After several attempts to get the tools to reenter the open hole, the tools were pulled back to the surface and rigged down. The drill pipe was lowered into the hole for one last depth check but encountered an obstruction at 438 mbsf. At that point all attempts to log Hole U1380C were abandoned, and the hole was plugged with a 10 bbl cement plug. The drill string was pulled from the hole, clearing the rig floor at 0055 h on 14 November. The rig floor was secured for transit, ending Hole U1380C and Site U1380.

Lithostratigraphy and petrology

Hole U1380C was drilled to investigate the lithostratigraphy and structural geology of the lower portions of the upper slope sequence and the uppermost portions of the basement, as interpreted in multichannel seismic reflection data. This hole deepens Site U1380, drilled during Expedition 334, and complements adjacent Site U1378, where only the upper part (539.9 mbsf) of the slope sediment was drilled during Expedition 334. After deploying casing and washing down to 438 mbsf, we reached the target depth at 800 mbsf and recovered 362 m of sedimentary rocks (Cores 344-U1380C-2R through 52R). Overall core recovery was moderate at 56%. The majority of the sedimentary sequence consists of clayey siltstone and silty claystone (~59% and ~24.5%, respectively), with common interlayered centimeter- to

decimeter-sized beds of fine- to medium-grained sandstone (~14.5%). The siltstone sedimentary sequence is disrupted by coarse-grained, shell-rich sandstone; two conglomerates (~1%); and 25 tuff layers (<1%) dispersed throughout the sedimentary sequence. Three lithostratigraphic units are distinguished based on lithologic compositional changes (Fig. F5; Table T2).

Unit I extends from 438 to 552.72 mbsf (Sections 344-U1380C-2R-1 to 13R-7, 55 cm) and is characterized by massive dark greenish gray silty clay and three sandstone-rich horizons with centimeter- to decimeter-sized sandy layers. These sandy layers increase in abundance, thickness, and grain size with depth. Matrix components comprise lithic fragments (sedimentary and magmatic), feldspar, glass shards, and amphibole. Biogenic components include rare nannofossils, diatoms, and foraminifers.

Unit II extends from 552.72 to 771.62 mbsf (Sections 344-U1380C-13R-7, 55 cm, to 47R-3, 106 cm) and is visually defined by a relatively sharp lithologic change to greenish gray clayey siltstone with intercalated sandstone and conglomerate layers. Unit II is further divided into two subunits based on compositional and depositional variations. Subunit IIA is characterized by poorly to weakly consolidated sand beds that contain abundant to common shell fragments. The matrix also contains abundant lithic fragments, feldspar, and zeolites, but the main mineralogical variation is the higher abundance of amphibole in this subunit. Low recovery hinders the precise measurement of the thickness of Subunit IIA (~11.38 m), but we assume that the missing material is composed of the same loose sand as the recovered sections. The lithologic boundary between Subunit IIA and IIB in Core 344-U1380C-15R (564.10 mbsf) was not recovered. Subunit IIB is very dark greenish gray clayey siltstone characterized by two fining-upward sequences of centimeter- to decimeter-thick medium- to coarse-grained sandstones and fine conglomerates. Matrix and sandstone components are predominantly terrigenous lithic fragments (magmatic more common than sedimentary), feldspar, glass, and rare heavy minerals. Biogenic material is mostly absent, and none was observed toward the bottom of the unit. Highly altered tuff layers in the lower parts of Cores 344-U1380C-30R (688.04 mbsf) and 47R (770.56 mbsf) are characterized by color changes from dark greenish gray clayey siltstone to reddish brown calcareous siltstone and by variations in the matrix mineralogy.

Both subunits are characterized by normally graded sandstone beds that are often laminated, with abundant sapropel fragments that form several centimeter-thick conspicuous horizons between the laminae. The conglomerates are very thickly bedded and contain poorly sorted, pebble-sized, matrix-supported lithic fragments. Upper contacts between fine- and coarse-grained sediments, when observed, are mostly gradational, whereas the lower contacts are erosional and commonly contain rip-up clasts, load casts, and sand lenses.

Unit III extends from 781.75 to 800 mbsf (Cores 344-U1380C-47R through 52R) and is a fine-grained silty claystone with rare but thick (as thick as 1.20 m) intercalated fine- to coarse-grained sandstones. The matrix contains mostly terrigenous material dominated by lithic fragments and feldspar but is nearly devoid of biogenic material.

Description of units

The 362 m long sedimentary sequence (Cores 344-U1380C-2R through 52R) recovered in Hole U1380C is assigned to three lithostratigraphic units (Fig. F5; Table T2).

Unit I

Interval: Sections 344-U1380C-2R-1, 0 cm, to 13R-7, 55 cm
Thickness: 114.72 m
Depth: 438.00–552.72 mbsf
Age: late? Pliocene to late Pleistocene
Lithology: silty clay with fine sandstone

Unit I is dark greenish gray silty clay with minor sandstone layers and four well-lithified (0.5–2 cm thick) tuff layers disseminated between Cores 344-U1380C-7R and 13R (Fig. F6). The clay sediment is moderately to highly bioturbated and well consolidated. The sandy layers are calcite cemented and occur throughout the unit as centimeter- to decimeter-thick beds that increase in abundance, thickness, and grain size with depth. Three sandstone horizons occur between 470 and 480 mbsf (Cores 344-U1380C-5R and 6R), 495 and 510 mbsf (Cores 8R and 9R), and 548 and 553 mbsf (Cores 12R and 13R). In these horizons, many sandstone beds exhibit rounded rip-up clay clasts at their base, features commonly associated with frequent erosional contacts at their base. Framboidal pyrite is macro- and microscopically ubiquitous throughout Unit I.

The main matrix components of Unit I are terrigenous and dominated by clay. Smear slides indicate that the most common accessory grains in the silty clay include feldspar and lithic (sedimentary and magmatic) fragments. Trace components include amphibole, calcite, biotite, chlorite, glass shards, and opaque minerals. The sandstone horizons are composed of feldspar and lithic fragments; however, unlike the silty clay, the sedimentary lithic component

is much larger than the igneous component. Glass, amphibole, and pyroxene are rare. Rare biogenic components include nannofossils, diatoms, and foraminifer fragments.

Unit II

Interval: Sections 344-U1380C-13R-7, 55 cm, to 47R-3, 106 cm
Thickness: 218.9 m
Depth: 552.72–771.62 mbsf
Age: late Pliocene to early Pleistocene
Lithology: clayey siltstone with medium to coarse sandstone

Unit II is clayey siltstone with interlayered sandstone and minor conglomerates. Unit II is divided into two subunits based on compositional changes. Subunit IIA contains abundant amphibole and feldspar, whereas clay is mostly absent. The sandstone layers contain abundant shell fragments and are very poorly consolidated. Subunit IIB lacks amphibole, and feldspar abundance is much diminished relative to Subunit IIA. Zeolite abundance, in contrast, increases substantially.

Unit II contains 21 disseminated tuff layers. A horizon between Cores 344-U1380C-29R and 31R contains 16 layers that range from 1 to 14 cm thick. Five more layers ranging from 2 to 47 cm thick are found in Core 344-U1380C-47R. These two tuff intervals, characterized by a reddish brown color, occur between 688.04 and 695.10 mbsf and 770.56 and 771.62 mbsf. Similarity of color and composition (with anorthite-rich feldspar and pyroxene) within these intervals imply that these are highly altered tuff layers. Physical properties and paleomagnetic data are consistent with this observation (see **"Physical properties"** and **"Paleomagnetism"**).

Subunit IIA (552.72–564.10 mbsf)

Subunit IIA consists of very dark greenish gray medium- to coarse-grained sandstone that contains abundant shell fragments (Fig. **F7**) intercalated with minor well-lithified and moderately bioturbated clayey siltstone layers. Occasional thin sandstone horizons are well lithified by calcite cement; however, most are poorly consolidated. The sand layers are commonly massive (as thick as several decimeters), but some beds exhibit millimeter-scale lamination. Shells, shell fragments, and lithic fragments are abundant and conspicuous components within the sandstone.

Smear slides indicate the sandstone components of Subunit IIA are terrigenous with abundant lithic fragments (sedimentary and magmatic), feldspar, amphibole, glass shards, and chlorite. Trace mineral phases include pyroxene, calcite, and opaque minerals. The siltstone matrix composition is similar to that of the sandstone, albeit with minor abundance variations of the major mineral phases. Biogenic components include common nannofossils, rare diatoms, and rare foraminifers; however, overall abundance in the sand is lower than in the siltstone.

Subunit IIB (564.10–771.62 mbsf)

Subunit IIB consists of two fining-upward sequences (564.1–687.5 and 695.1–770.5 mbsf) of very dark greenish gray clayey siltstone that is moderately bioturbated and intercalated with sandstone and minor conglomerate beds (Fig. **F8**). The sandstone layers are abundant and massive (as thick as 80 cm) and are normally graded; they become thicker and coarser with depth, and many are also laminated. The siltstone, sandstone, and conglomerate layers are moderately well lithified by calcite cement. Bioturbation is moderate in the siltstone lithologies and is not observed in the sandstone. This unit is moderately to highly fractured by drilling.

In general, the fine sandstone and siltstone layers are well sorted, whereas the coarse-grained sandstone and conglomerate layers are poorly sorted. The clayey siltstone often contains reworked sandstone lenses and, occasionally, sedimentary dikes that cut across bedding planes. Load casts and convolute bedding, due to synsedimentary liquefaction, were observed at the transition between the conglomerate and siltstone layers (Fig. **F9**). The sandstone beds exhibit erosive contacts at their base and mostly gradational contacts into the overlying sediments. Toward the bottom of the sequence, rip-up siltstone clasts and fragmented (as large as 8 cm) calcite-cemented breccia are more frequent. The abundance of shell fragments in Subunit IIB is reduced toward the base of the unit. In contrast, sporadic wood fragments and sapropel increase with depth and form thin horizons along the sandstone bedding planes (Fig. **F10**). Conglomerate layers contain subrounded to subangular pebble-sized clasts composed of volcanoclastic and plutonic material, sedimentary clasts, and rip-up siltstone clasts (Fig. **F11**).

Siltstone and sandstone smear slides indicate that the dominant matrix composition is volcanogenic and sedimentary lithic fragments, along with common feldspar and glass. Accessory phases include calcite, chlorite, amphibole, and pyroxene. The biogenic components decline precipitously and are absent in the lowermost part of Subunit IIB. The conglomerate beds are matrix supported and contain the same clast and mineral assemblage as the siltstone and sandstone.

Unit III

Interval: Sections 344-U1380C-47R-CC, 0 cm, to 52R-CC, 19 cm
Thickness: 18.25 m
Depth: 771.62–800 mbsf
Age: late Pliocene
Lithology: silty claystone

Unit III is massive, well-lithified, very dark greenish gray silty claystone with intercalated sandstone layers (Fig. F12). The silty claystone contains common calcite-cemented horizons. Sandstone beds in Unit III are less common than in Units I and II but are generally thicker (as thick as 1.20 m).

Smear slides indicate that the most abundant components in the siltstone and sandstone layers are lithic fragments (sedimentary and magmatic) and feldspar. Zeolites are common, whereas amphibole, chlorite, calcite, and opaque minerals are present as accessory minerals. Microfossil components continue to be very rare to nearly absent.

X-ray diffraction analyses

Preliminary X-ray diffraction analysis of sediment samples from Hole U1380C suggests that there is little variation in composition within each lithostratigraphic unit (Fig. F13).

X-ray diffractograms of Unit I indicate that the major mineral components are phyllosilicates, including chlorite and smectite, quartz, plagioclase, and calcite. Zeolites (laumontite and heulandite) and pyrite are also present in all samples, whereas amphibole (hornblende) peaks are sporadically observed.

Stronger variation in mineral composition is noticed between silty clay samples that were collected from Unit I and Unit II sediment. Smectite and pyrite peaks are not observed in the upper part of Unit II, and plagioclase is less apparent. Hornblende is present in significant amounts in all samples from the upper part of Unit II. Analcime, a zeolite-like mineral, is present as a major mineral in Unit II, whereas it is not observed in Unit I.

Samples from Subunit IIA produced spectra dominated by zeolites (analcime, laumontite, and heulandite), calcite, quartz, plagioclase, hornblende, and chlorite.

X-ray diffractograms of samples from Subunit IIB indicate that the major mineral components are zeolites (analcime and heulandite), quartz, calcite, plagioclase, and chlorite. Laumontite is present in the upper part of Subunit IIB but decreases with depth and is absent below 710 mbsf. Smectite and pyrite are minor components. Tuff layers in Subunit IIB present different general patterns with respect to the rest of the sediment; they contain more zeolite (with laumontite events in both horizons), a different plagioclase composition, and an enrichment in hornblende.

X-ray diffractograms of Unit III indicate that the major mineral components are quartz, plagioclase, analcime, calcite, and chlorite. Heulandite and pyrite are minor phases.

Depositional environment

Lithostratigraphic Unit I is a continuation of the sediment cored in Hole U1380A during Expedition 334 and resamples the same lithologic features. Lithologic comparison to sites from Expedition 334 reveals a good correlation between Unit I from Hole U1380C (Expedition 344) and Unit II from Hole U1378B (Expedition 334). This correlation is based on the similar occurrence of general lithology (e.g., sandy layers increasing in thickness and abundance toward the bottom of units), as well as the similar terrigenous composition of the sediment as observed in smear slides.

The sedimentary succession recovered from Hole U1380C is probably an alternating terrestrially sourced, turbiditic upper slope (Units I and III) to shelf (Unit II) sequence, eventually being influenced by deltaic-derived sediments. This system has fed the depositional area with coarser, organic-rich (wood) sediment, alternating with fine-grained sediment during undisturbed sedimentation conditions (i.e., overbank facies). The frequent erosional bottom contacts of the sandstone and conglomerates, the rip-up clasts observed at sandstone to siltstone contacts, the subrounded to subangular shape of the clasts, and the occasional fragments of interbedded coal attest to the proximity of the source area. The dynamic depositional environment is also well documented by the varying grain sizes that range as large as pebbled sized conglomerates, especially in Unit II, and the cyclic increasing abundances of sandstone throughout the sedimentary sequence.

Two large-scale fining-upward cycles (100 m thick sediment packages) in Unit II may be evidence for relative tectonically or climatically controlled sea level changes and/or the repeated migration of the depositional area into the active or deactivated channel systems typical of deltaic depositional areas. Unit III seems to represent a return to an upper slope system but is too thin to provide more detailed constraints and/or interpretations.

Paleontology and biostratigraphy

The microfossil content of core catcher samples from Hole U1380C was examined. Because radiolarians

were not present in core catcher samples, biostratigraphic zones were determined by nannofossil content. Benthic foraminifers were used to characterize paleoenvironmental changes at Site U1380.

Calcareous nannofossils

Calcareous nannofossils were observed in 49 of the 52 examined core catcher samples. Three core catcher samples are barren (Samples 344-U1380C-18R-CC, 31R-CC, and 41R-CC). Overall nannofossil preservation is moderate to poor, with abundances ranging from few to rare.

Four biostratigraphic zones were identified. The interval from 439.47 to 460.26 mbsf is assigned to nannofossil Zones NN19–NN21, based on the presence of *Gephyrocapsa oceanica* in Sample 344-U1380C-2R-CC. The second interval, between Samples 344-U1380C-5R-CC and 8R-CC, is assigned to Zone NN19, based on the presence of *Pseudoemiliania lacunosa*. The third zone, NN18, is defined by the first downhole occurrence of *Discoaster brouweri*, which appears in Sample 344-U1380C-9R-CC. *Calcidiscus leptoporus*, *D. brouweri*, *G. oceanica*, *P. lacunosa*, and *Helicosphaera carteri* are indicative species of this assemblage (Table **T3**). A fourth biostratigraphic zone is tentatively proposed and encompasses Samples 344-U1380C-51R-CC and 52R-CC (791–797 mbsf). It is assigned to Zones NN15–NN17, based on the last occurrence of *Discoaster pentaradiatus*, the first occurrence of *P. lacunosa* in Sample 344-U1380C-51R-CC, and the first occurrence of *Discoaster asymmetricus* in Sample 52R-CC. However, as the boundary between Zones NN18 and NN15–NN17 is located between Samples 344-U1380C-50R-CC and 51R-CC, the oldest sediment is assumed to be closer to the upper Zone NN17 boundary (~2.4 Ma). Based on this assumption, the sediment accumulation rate for Zone NN18 (272 mbsf) is estimated to be 590 m/m.y.

Benthic foraminifers

Benthic foraminifers were studied in 44 of the 52 core catcher samples (Table **T4**). All samples were indurated and treated with H_2O_2 before sieving (see **"Paleontology and biostratigraphy"** in the "Methods" chapter [Harris et al., 2013b]). Despite the large amount of material examined, the abundance of benthic foraminifers varies from few (Samples 344-U1380-2R-CC through 9R-CC) to present (Samples 31R-CC through 52R-CC). Benthic foraminifers are absent in Sample 344-U1380C-32R-CC. Planktonic foraminifers are rare throughout all samples; therefore, the planktonic to benthic ratio could not be accurately determined.

Preservation ranges from moderate where abundance is high to poor where foraminifers are present or rare (Table **T4**). Several samples are very poorly preserved. Samples 344-U1380C-10R-CC and 11R-CC show clear signs of carbonate dissolution. Samples 344-U1380C-13R-CC and 14R-CC contain ~95% broken and/or abraded benthic foraminifers, corresponding to Subunit IIA (Fig. **F14**).

Overall, benthic foraminifer assemblages are characterized by several indicative species, including *Uvigerina peregrina*, *Cibicidoides pachyderma*, *Epistominella smithi*, several species of the genus *Brizalina* (Table **T4**), and *Hansenisca altiformis*. These species are also present in samples from Hole U1381C (see **"Paleontology and biostratigraphy"** in the "Input Site U1381" chapter [Harris et al., 2013a]). Less common species include *Globocassidulina* sp., *Planulina ornata*, *Stainforthia complanata*, and *Sphaeroidina bulloides*. Benthic foraminifer percentages were only calculated on samples that contained at least 100 individuals (Fig. **F14**). However, because of the low abundance and poor preservation of individuals, these percentages should be treated with caution. Benthic foraminifer assemblage changes downhole are relatively subtle. *U. peregrina* and *E. smithi* are more frequent in Unit I, whereas *C. pachyderma* and *H. altiformis* are more common in Unit II. *E. smithi* is a species extensively described in oxygen minimum zones around the world (Sen Gupta and Machain-Castillo, 1993), and *U. peregrina* is known to live in environments with moderate to high organic carbon fluxes at the seafloor (Fontanier et al., 2003). The presence of these species, together with the relative high abundance of *Brizalina* spp., also typical of high productive settings (Sen Gupta and Machain-Castillo, 1993), suggests an environment rich in organic carbon with periods of low bottom water oxygenation. In the upper part of Unit II, the increase of the epifaunal–shallow infaunal *C. pachyderma* and the relatively oligotrophic *H. altiformis* may suggest a change in oxygen levels at the seafloor coupled with less organic carbon. Changes in the water column depth cannot be inferred with confidence from the data reported here because of the low abundance and poor preservation of foraminifers, coupled with the subtle assemblage changes downhole.

Structural geology

The primary objective of structural geology studies during Expedition 344 was to describe and document the style, geometry, and kinematics of structures observed in the cores. Site U1380, located on the middle slope of the Costa Rica forearc, offshore the Osa Peninsula, was drilled for the first time during Expedition 334. Hole U1380A was drilled to 397.0 mbsf with a cored interval of 52.37 m. During Expedition 344, Site U1380 was reoccupied. Coring

in Hole U1380C began at 438 mbsf and continued to 800 mbsf. Bedding dips vary from subhorizontal to moderately steep, with a mean dip of ~20°. Moderate to strong foliation is present between 496 and 551 mbsf (Fig. F15). A total of 154 fault planes were identified throughout the cored interval. Areas of particularly localized faulting and intense fracturing and brecciation were defined as fault zones. The sense of shear was determined mainly by slicken steps and the attitude of fault planes. Fault planes were divided into normal, reverse, and strike-slip faults. Because of intense fracturing and drilling disturbance through the entire hole, only a few orientation data were paleomagnetically corrected (Fig. F16). Paleomagnetically corrected bedding planes show a general strike northwest–southeast with gentle dipping angles between 10° and 30° northeast and southwest, respectively. Although data are slightly scattered, fault kinematics analyses inferred a normal fault stress regime with σ_1 and σ_3 oriented vertically and in a northeast–southwest direction (Fig. F16).

Structures in slope sediment

The general deformational fabrics of the slope sediment cored in Hole U1380C allow us to distinguish two structural domains: Domain I ranges from Core 344-U1380C-2R (438 mbsf) to Section 13R-6, 46 cm (551.48 mbsf), and Domain II ranges from Section 13R-6, 46 cm (551.48 mbsf), through Core 52R (797.42 mbsf).

Domain I (438–551.48 mbsf)

Abundant faults and fractures (the latter without obvious displacement) and relatively steeply dipping bedding planes characterize the upper part of Hole U1380C. This interval is characterized by the downward progressive development of a penetrative planar fabric that partly forms foliation overprinting the sedimentary structures. This development can be observed from Core 344-U1380C-7R to Section 13R-6, 46 cm, where the sediment mass easily splits along foliation surfaces. The progressive increase in foliation intensity involves both closer spacing and a dominant planar geometry of its surfaces downhole toward 551.48 mbsf. Hand lens observations show that the most intense foliation develops in Core 344-U1380C-13R (Fig. F17) where the surfaces are characterized by the preferred alignment of platy minerals. In the upper part of the interval, the orientation of foliation is mostly parallel to bedding/laminations (Fig. F15). Moving downhole toward 551.48 mbsf, foliation becomes less steep (4°–5°) but bedding maintains a moderate to steep dip (30°). The foliated interval (496.37–548.98 mbsf) is also characterized by deformation bands and veins. Core 344-U1380C-13R records the simultaneous occurrence of posttilting of both deformation bands and veins.

Fault planes show normal, strike-slip, and reverse sense of shear. Reverse faults increase in abundance downhole toward Core 344-U1380C-13R, where they are as abundant as normal faults. In Core 344-U1380C-13R, we also observe intense brecciation. The brecciated domains are composed of centimeter- to subcentimeter-sized angular fragments aligned along a preferred orientation and with polished surfaces. We interpret these foliated brecciated domains to be fault zones. The bottom of Domain I coincides with the strong reflector identified in seismic Line BGR99-7, located at ~550 mbsf (Fig. F1).

Domain II (551.48–797.42 mbsf)

The lower part of Hole U1380C is characterized by a downhole trend of decreasing bedding dip angles. Dip angles change from an average of 40° above 630 mbsf to an average of 10° in the lowermost 100 m of the hole. The decrease in bedding dip values is not linear but shows steps associated with brecciated zones at ≈620–625, ≈697–705, ≈750–755, ≈760–764, ≈770–773, ≈775–778, and ≈790–793 mbsf (Fig. F15). The zones between 750 and 778 mbsf define a particularly tectonized interval where bedding dip angles are higher than immediately above and below. This interval also corresponds to a relative increased frequency of faults. Faults with both a normal and reverse sense of shear are common throughout the structural domain and equally present, and their abundance increases downhole. Strike-slip faults increase in abundance downhole as well.

Domain II includes well-consolidated sediment (see **"Physical properties"**). Mud and sand dikes are injected upward into cemented intervals, occasionally leading to formation of a jigsaw-puzzle structure indicative of in situ brecciation. Mineral veins, mostly calcite, are also identified in the cemented interval in this domain. These structures indicate that high fluid pressure was generated just below the consolidated interval.

The paleomagnetically corrected bedding planes generally strike northwest–southeast, almost parallel to the trench axis (Fig. F16B). The beddings dip gently between 10° and 30° both northeast and southwest, corresponding to the landward and trenchward directions, respectively. Fault kinematics analyses were conducted based on paleomagnetic data using the "FaultKin" software (Allmendinger, 2011; **www.geo.cornell.edu/geology/faculty/RWA/programs/faultkin-5-beta.html**) (Fig. F16B). A normal fault stress regime with σ_1 and σ_3 oriented to the vertical and northeast–southwest, respectively, is inferred from the analyses. This indicates an extension stress

regime that is quite similar to that at Site U1379 (Expedition 334 Scientists, 2012b).

Geochemistry

Inorganic geochemistry

We collected 25 whole-round samples (15–40 cm long) on the catwalk at a frequency of 1–4 samples per core through Core 344-U1380C-17R. After washing and installing casing, the first interstitial water sample was collected. These whole-round samples were thoroughly cleaned to remove drilling contamination prior to squeezing. The cleaned samples were placed in Ti squeezers and squeezed at gauge forces up to 30,000 lb. The inner diameter of the Ti squeezers is 9 cm; thus, the maximum squeezing pressure was 3043 psi (~21 MPa). The pore fluid was collected in syringes and passed through a 0.2 µm filter prior to analysis. The volume of pore fluid recovered varied with lithology and burial depth from 2 mL to a maximum of 25 mL. Specific aliquots were used for shipboard analyses, and the remaining fluid was sampled for shore-based analyses (see **"Geochemistry"** in the "Methods" chapter (Harris et al., 2013b).

Sediment samples from Core 344-U1380C-18R to the bottom of the hole were compacted or cemented, and squeezing at gauge forces <30,000 lb did not yield pore fluid. Therefore, 12 whole-round sediment samples with lengths ranging from 20 to 30 cm were collected between 613 and 788 mbsf for shore-based handling and analyses. These samples were cleaned in the same manner as the shipboard interstitial water samples and stored in double vacuum-sealed bags.

Two additional 25 to 30 cm long whole rounds were acquired from Sections 344-U1380C-3R-5 and 9R-3 for He isotope analyses. These samples were handled in the lower tween deck to avoid contamination with gas tank He present in the Chemistry Laboratory. They were stored and cleaned in a N_2 glove bag at 4°C, squeezed as described above, and stored in Cu tubes that were crimped tightly.

Below the sulfate–methane transition zone, sulfate is depleted in the pore fluids and any sulfate present in a sample is a result of contamination with surface seawater that was pumped down the hole while drilling. Based on the sulfate concentration of each interstitial water sample, we used the chemical composition of the surface seawater to correct each analysis for contamination. The chemical composition of the surface seawater used during drilling at this site is listed in Tables **T5** and **T6.** Raw data for the major element concentrations in pore water are listed in Table **T5,** and in Table **T7** we list the sulfate-corrected concentration data. Similarly, Tables **T6** and **T8** list the uncorrected and corrected minor element concentrations, respectively. Only the sulfate-corrected data are illustrated in Figures **F18, F19,** and **F20.**

For gas analyses, 61 headspace samples were collected using a 5 mL cut-off syringe directly adjacent to the pore water. Samples were analyzed following protocols described in **"Geochemistry"** in the "Methods" chapter (Harris et al., 2013b), using a gas chromatograph equipped with a flame ionization detector and on the natural gas analyzer.

In addition to the fluid samples, 65 sediment samples were collected from the working half of the core, adjacent to the pore water samples. These samples were freeze-dried, ground, and analyzed for inorganic carbon (IC) and total carbon (TC) concentrations. The data are listed in Table **T9.**

Salinity, chloride, and alkalis (sodium and potassium)

Downhole profiles of salinity, chloride, sodium, and potassium in Hole U1380C are shown in Figure **F18,** which also includes data collected in Holes U1378B and U1380A during Expedition 334 for comparison (Expedition 334 Scientists, 2012a, 2012c). Salinity values at Site U1378 decrease steadily from seawater value (35) at the seafloor to ~18 at the base of the hole. Salinity values measured in Hole U1380C are consistent with those measured at Site U1378 and vary between 20.5 and 23.5. These low values suggest the presence of a fresher fluid resulting from mineral dehydration reactions at depth. Chloride concentrations at Site U1378 also decrease steadily with depth, reaching a minimum value of ~358 mM at the base of the hole, and are also well below the modern seawater value (559 mM). Concentrations measured in Hole U1380C are consistent with those measured at the base of Site U1378 and range between 371 and 392 mM. These concentrations are 36%–30% fresher (depleted in chloride) than modern seawater and change only slowly with depth below ~500 mbsf. Overall, Cl values are consistent with those observed at equivalent depths at Site U1378 and in Hole U1380A. The in situ temperature within this depth range is too cold to support local clay dehydration (Expedition 334 Scientists, 2012a, 2012c; see **"Physical properties"**); thus, the Cl data suggest interaction with a fluid that has migrated from a region with temperatures >60°C, high enough to support clay dehydration (Perry and Hower, 1970; Bekins et al., 1994, and references therein).

Sodium concentrations range between 294 and 330 mM throughout the cored section (Fig. **F18**), which corresponds to 39%–30% freshening of seawater and is consistent with the dilution values obtained for Cl. The near-constant Na/Cl molar ratio

with depth suggests that the depletion in pore fluid Na is almost entirely related to dilution rather than mineral-fluid reactions. In addition to being influenced by the same freshening signal observed in the Cl and salinity data, potassium concentrations decrease with depth from 5.95 mM at 452 mbsf to 1.94 mM at 584 mbsf in Hole U1380C, indicating that K is involved in fluid-mineral reactions, likely the smectite to illite transformation. This reaction requires a minimum temperature of ~50°–60°C. The observed temperature gradient measured at Site U1378 is 51.4°C/km (Expedition 334 Scientists, 2012a; see **"Physical properties"**), yielding an in situ temperature of ~25°–32°C in the depth range of the Hole U1380C chemical profiles. This temperature range is below the minimum required for the transformation of smectite to illite, supporting the interpretation that the recovered fluids have interacted with a deeper fluid source.

Alkalinity, sulfate, ammonium, phosphate, calcium, and magnesium

The depth interval cored at this site is well below the sulfate–methane transition zone, so no sulfate should be present in the pore fluids, making sulfate an excellent tracer for contamination with surface seawater that was used as drilling fluid. Sulfate concentrations measured after thoroughly cleaning the samples prior to squeezing range from 1.2 to 2.4 mM (Table **T5**). These data were used to correct the pore fluid concentrations reported in Tables **T7** and **T8.**

Because of the low volumes of pore fluid recovered through the depth interval cored and the rather large pore fluid volume (3 mL) required for shipboard alkalinity analysis, only select samples were analyzed for alkalinity. Alkalinity values are rather low in the depth range cored in Hole U1380C, having a maximum value of 7.20 mM at 473 mbsf and decreasing with depth to 1.53 mM at 522 mbsf (Table **T7;** Fig. **F19**).

Organic matter diagenesis in the upper sediment section is observed in the ammonium concentration-depth profile of Site U1378 (Fig. **F19**) (Expedition 334 Scientists, 2012a), where ammonium values reach a maximum of ~8 mM at ~320 mbsf and then decrease to 4.74 mM at the top of the equivalent section drilled in Hole U1380C. Similar to alkalinity, the ammonium concentrations continue to decrease nearly linearly with depth to 1.98 mM in the deepest sample analyzed at 584 mbsf.

In the uppermost part of the drilled section at this site (~450 mbsf) both Ca and Mg concentrations are depleted relative to the corresponding seawater values of 10.55 and 54.0 mM, respectively. The depletions are caused by carbonate diagenesis and some volcanic tephra alteration reactions in the upper sediment section as seen in the adjacent Site U1378 data (Fig. **F19**) (Expedition 334 Scientists, 2012a). Proceeding from ~450 mbsf to the deepest sample analyzed, Ca concentrations steeply increase by 23 mM, from 8.14 to 31.2 mM, a value that represents almost three times the seawater concentration. In contrast, Mg concentrations decrease with depth by 18 mM, from 18.5 to 0.40 mM, at a Ca:Mg ratio close to 1:1. The increase in Ca and decrease in Mg with depth likely reflect diffusional interaction with a deeper fluid that reacted with volcanic tephra and/or oceanic basement at elevated temperatures. This observation, coupled with the low K values discussed above, suggests that the reaction temperature is <150°C.

Strontium, lithium, manganese, silica, boron, and barium

Downhole distributions of Sr, Li, Mn, Si, B, and Ba are shown in Figure **F20,** which includes data collected from Hole U1378B during Expedition 334 (M.E. Torres et al., unpubl. data) for comparison.

Sr concentrations increase downhole from 44 µM at ~450 mbsf (~50% of modern seawater value) to a maximum of 75 µM (~86% seawater value) at ~550 mbsf. This zone of increasing Sr concentrations correlates with the base of a shear zone that extends from ~480 to 550 mbsf (see **"Structural geology"**). Sr concentrations decrease sharply to ~63 µM in the lowermost ~30 m sampled and squeezed onboard for interstitial water (552–584 mbsf). Shore-based Sr isotope ratio determinations may help to identify the various reactions that are responsible for the observed Sr concentration-depth profile.

Li concentrations measured in samples from Site U1378 are lower than seawater values (26 µM) and are relatively constant from ~20 to 450 mbsf (Fig. **F20**) (M.E. Torres et al., unpubl. data). At Site U1378, Li concentrations increase below 450 mbsf to a maximum value of 59 µM at 489 mbsf and then decrease slightly to the base of the hole. In Hole U1380C, the Li concentration is already 80 µM at 452 mbsf and remains elevated between this depth and 540 mbsf, ranging from 58 to 69 µM. Below this depth, Li concentrations decrease sharply to ~10 µM at 584 mbsf. The zone of elevated Li concentrations correlates with the broad shear zone extending from ~480 to 550 mbsf (see **"Structural geology"**), as well as the horizon with depleted Cl and Ca concentrations, elevated Sr concentrations, and the only interval where thermogenic hydrocarbons (propane, butane, and pentane) were observed at this site (Fig. **F21**). Based on smectite-seawater hydrothermal experiments (You and Gieskes, 2001; Wei et al., 2010), the Li concentrations indicate fluid-rock reaction at source

temperatures greater than ~80°C. Furthermore, temperatures within the shear zone are too low to support in situ formation of thermogenic hydrocarbons. Collectively, the Cl, Li, and hydrocarbon data clearly indicate that fluid migration along this horizon originated from a source depth where temperatures are >90°C. The decrease in Li concentrations below the shear zone reflects the presence of a fluid at depth that has interacted with volcanic material and/or oceanic basement at a lower temperature. This is also indicated by the decrease in Mg concentrations and increase in Ca concentrations below the uncomformity at 550 mbsf. This fluid is likely sourced at temperatures <80°C but >60°C, as Cl is depleted (indicating clay dehydration reactions) and there are no thermogenic hydrocarbons present (Figs. **F20, F21, F22**).

Mn concentrations in pore fluids sampled from Hole U1380C are variable and range from 0.11 to 1.4 µM. B concentrations are below the modern seawater value and vary between ~58 and 187 µM, with the band of lowest concentrations in the broad shear zone that extends from ~480 to 550 mbsf (see **"Structural geology"**), where Cl concentrations are depleted and Ca and Sr concentrations are elevated.

Si concentrations in Hole U1380C are rather low and relatively constant with depth, ranging from 96 to 163 µM, indicating that the solubility of quartz in the sand, instead of feldspars or clay minerals, controls Si concentrations in the pore fluids.

Ba concentrations are relatively low and constant with depth, ranging from 1.22 to 2.82 µM. No obvious trends are observed in the Ba concentration-depth profile in Hole U1380C, and the data are consistent with values obtained for the equivalent depth range in Hole U1378B (M.E. Torres et al., unpubl. data).

Organic geochemistry

Organic geochemistry data for Hole U1380C are listed in Tables **T9** and **T10** and plotted in Figures **F21** and **F22.** In the headspace gases, methane concentrations range from 900 to 43,000 ppmv. Ethane concentrations range between 2 and 32 ppmv. Heavy hydrocarbons (C_{3+}) were only detected between 452 and 552 mbsf (Section 344-U1380C-13R-7). No heavy hydrocarbons were detected below 552 mbsf. The C_1/C_{2+} ratio was <400 above 551.9 mbsf, and below that depth values are consistently >400. This finding likely indicates that the hydrocarbons above 552 mbsf have a thermogenic component consistent with the Cl and Li concentration profiles, whereas the sediments below 552 mbsf are predominantly from biogenic sources.

Organic and IC distributions are illustrated in Figure **F23.** TC increases from <0.9 to ~2.5 wt% at 553 mbsf; below that depth, TC ranges between 0.4 and 1.4 wt%. This remarkable concentration change is consistent with the observed changes from lithostratigraphic Unit I to Unit II (see **"Lithostratigraphy and petrology"**). IC also increases from ~0.1 to <1.5 wt% down to the lithostratigraphic Unit I/II boundary and then decreases to 0.2 wt% below that depth. The total organic carbon concentration also has a marked change in concentration at this boundary, from 0.9–1.4 to 0.1–0.8 wt%.

Physical properties

At Site U1380, physical property measurements were made to help characterize the lithostratigraphic units. After sediment cores reached thermal equilibrium with ambient temperature at ~20°C, gamma ray attenuation (GRA) density, magnetic susceptibility, and *P*-wave velocity were measured using the Whole-Round Multisensor Logger (WRMSL). After WRMSL scanning, the whole-round sections were logged for natural gamma radiation (NGR). Following core splitting, a digital imaging logger and a color spectrophotometer were used to collect images of the split surfaces, and magnetic susceptibility was measured on the archive-half cores. Moisture and density (MAD) were measured on discrete samples collected from the working halves of the split sediment cores, generally once per section. Half-space thermal conductivity, *P*-wave velocity, and strength were measured on the working halves of split cores, generally one to two per core, depending on recovered length and condition. To examine overall trends from the seafloor to total depth, we also used data from Site U1378, which was drilled during Expedition 334 and is located ~1 km from Site U1380.

Density and porosity

Bulk density values in Hole U1380C were determined from both GRA measurements on whole-round cores and mass/volume measurements on discrete samples from the working halves of split cores (see **"Physical properties"** in the "Methods" chapter [Harris et al., 2013b]). In general, wet bulk density values determined from discrete samples are higher than the whole-round GRA measurements, and both sets of measurements show similar downhole trends (Figs. **F24, F25A**). Grain density measurements were determined from mass/volume measurements on dry discrete samples within the sedimentary sequence. Grain density values averaged 2.7 g/cm^3 (Fig. **F25B**). Porosity was determined from mass/volume measurements on discrete sediment samples using MAD Method C (see **"Physical properties"** in the "Methods" chapter [Harris et al., 2013b]). Bulk density and

porosity data appear to follow a steady compaction trend from the surface to ~550 mbsf, with porosities yielding a best-fit exponential relationship of porosity = 0.68exp(–0.0008 × depth), where depth is in mbsf. Between 550 and 555 mbsf, bulk density increases from ~2.0 to 2.1 g/cm^3 and porosity decreases from 43% to 35%, falling below the compaction trend (Fig. F25C). This decrease may reflect lithologic changes or differences in burial history at the Unit I/II boundary (see "Lithostratigraphy and petrology"). At 700 mbsf, bulk densities peak at 2.2 g/cm^3 and porosities reach their lowest values of 25% to 26%.

Magnetic susceptibility

Volumetric magnetic susceptibilities were measured using the WRMSL, and point measurements were made on the Section Half Multisensor Logger (SHMSL) for all recovered sediments from Hole U1380C. Magnetic susceptibility values measured with these two methods show similar patterns (Fig. F26). Magnetic susceptibility is relatively low (generally <50 IU) between 400 and 550 mbsf (Unit I), consistent with the observed abundance of noniron-bearing clays.

Between 550 and 700 mbsf (uppermost 150 m of Unit II), magnetic susceptibility values are more variable, ranging from ~40 to >500 IU. Most positive excursions seem to be associated with coarser grained material, and the highest excursions are associated with recovered tephra layers near 690 mbsf. Between 700 and 770 mbsf (the rest of Unit II), magnetic susceptibility is consistently low (40–50 IU), despite the continued occurrence of coarse-grained layers. Unit III (below 770 mbsf) is characterized by positive excursions in magnetic susceptibility, similar to the upper portion of Unit II. Section 344-U1380C-49R-2 (~780 mbsf) contained metal fragments from the core catcher, creating a spike exceeding 4000 IU in the WRMSL data. These fragments were removed before running the section through the SHMSL.

Natural gamma radiation

NGR counting periods were 10 min. Measurement spacing was fixed at 20 cm for Sections 344-U1380C-2R-2 (~440 mbsf) through 12R-9 (~545 mbsf) and at 10 cm for Sections 344-U1380C-13R-1 to the bottom of the hole. Total NGR results above 480 mbsf are consistent with NGR data from Hole U1380A obtained during Expedition 334 (Fig. F27), generally ranging between 15 and 25 cps. NGR values increase with depth between 480 and 550 mbsf (Unit I/II boundary) ranging as high as 30 cps, decrease at this lithologic boundary, and are relatively constant throughout Units II and III, generally ranging between 15 and 20 cps. The highest counts, as high as 38 cps, were observed at the lowermost part of Unit I, and the lowest counts, around 10 cps, were observed between 650 and 700 mbsf.

P-wave velocity

P-wave velocity in Hole U1380C was measured on the working halves of sediment split cores using the *P*-wave caliper measurement (Fig. F28). *P*-wave velocity averages 1700 m/s in Unit I, increasing from ~1650 m/s at ~450 mbsf to ~1900 m/s at 550 mbsf. Just below the Unit I/II boundary, *P*-wave velocity jumps to ~2000 m/s and increases to ~2250 m/s at the bottom of Unit II. Conspicuously higher *P*-wave velocities up to 2500 m/s were observed at 700 mbsf and are associated with calcareous silt (Cores 344-U1380C-30R and 31R). In Unit III, *P*-wave velocity is ~2350 m/s.

Thermal conductivity

Thermal conductivity measurements were conducted on split cores using the half-space method (see "Physical properties" in the "Methods" chapter [Harris et al., 2013b]). In general, thermal conductivity values in Hole U1380C agree with values in Hole U1378B using the same half-space method (Fig. F29A). Thermal conductivity varies inversely with porosity (Fig. F25C). Thermal conductivity increases with depth from 450 to 550 mbsf, steps to higher values at the Unit I/II boundary, and then increases slightly with depth to 720 mbsf. Thermal conductivity decreases at 720 mbsf, remains nearly constant to 771 mbsf, and increases at the Unit II/III boundary. Overall thermal conductivity ranges from 0.81 to 1.64 W/(m·K). The mean and standard deviation of thermal conductivity are 1.31 and 0.145 W/(m·K), respectively.

Downhole temperature and heat flow

The temperature-depth relation was evaluated using the Bullard (1939) method (see "Physical properties" in the "Methods" chapter [Harris et al., 2013b]) and the measured temperatures and the estimated heat flow value of 0.0442 W/m^2 from Hole U1378B (Expedition 334 Scientists, 2012a). We compared results using two models for the variation of thermal conductivity with depth, k (z). The first model assumes a linear increase of thermal conductivity with depth given by a least-squares fit (Model 1); the second is based on the thermal resistance determined from each measured conductivity value (Model 2). Mudline temperatures measured in Hole U1378B average 12.3°C, which is higher than the shallowest in situ temperature measurement (9.94°C at 33 mbsf). It is likely that these elevated mudline temperatures reflect warming by circulation of surface seawater

during drilling. As a result, bottom water temperatures were estimated by a least-squares method for each model of thermal conductivities. Models 1 and 2 yielded values of 7.64° and 7.76°C, respectively, for the sediment/water interface and 41.32° and 41.59°C, respectively, at the bottom of Hole U1380C (Fig. F29B).

Sediment strength

Compressive sediment strength was measured using a third-party needle penetrometer (see "Physical properties" in the "Methods" chapter [Harris et al., 2013b]). Three measurements were taken near the *P*-wave velocity measurement in each section (Fig. F30). Above ~550 mbsf, compressive strength varies from ~340 to 1100 kPa. Below ~550 mbsf, results become more variable, ranging between ~220 and ~6000 kPa, but generally increase with depth. No distinct change occurs at the Unit I/II boundary. An apparently cemented sample at ~605 mbsf shows an extremely high value of 12000 kPa.

Color spectrophotometry

Results from color reflectance measurements are presented in Figure F31. Reflectance L* values generally vary between ~23 and ~45 throughout Hole U1380C, with scattered values as low as 14.5 to as high as 67. Reflectance a* and b* values show a clear shift at 496 mbsf. Reflectance a* values above 496 mbsf vary between ~2 and ~7, whereas below ~496 mbsf, values vary between –3 and 3, with several values ranging up to ~22. Reflectance b* values vary between –17 and –8 above ~496 mbsf, whereas values below ~496 mbsf generally range between –7 and 4.

Core-seismic correlation

Although it is not possible to provide an interval velocity profile and a synthetic seismogram because poor hole conditions prevented completion of logging operations (see "Operations"), three potential horizons of core-seismic correlation were identified (Fig. F32). The largest change in all physical property values except color reflectance occurs at the boundary between Units I and II, where the major seismic reflector at the top of the acoustic basement lies at 550 mbsf. The second major change in physical properties occurs at ~700 mbsf and is identified by a strong positive spike of magnetic susceptibility, a positive spike of *P*-wave velocity, and a slight negative excursion of NGR. This horizon could correlate to a strong landward-dipping reflector at ~700 mbsf. The other notable change in both magnetic susceptibility and *P*-wave velocity at the Unit II/III boundary could correlate to a moderately strong seismic reflector at 770 mbsf. These results suggest that the conspicuous seismic reflectors are due to lithologic changes.

Paleomagnetism

We measured the natural remanent magnetization (NRM) of all archive-half core sections (Cores 344-U1380C-11R through 52R) and 60 discrete samples taken from the working halves. We subjected archive-half cores to alternating field (AF) demagnetization up to 30 mT and measured them with the pass-through superconducting rock magnetometer (SRM) at 2.5 cm intervals. Discrete samples were subjected to stepwise thermal and AF demagnetization up to 475°C and 120 mT, respectively, to isolate the characteristic remanent magnetization (ChRM). Discrete samples were also measured with the SRM.

Natural remanent magnetization of sedimentary cores

Downhole variations of paleomagnetic data obtained from Hole U1380C are shown in Figure F33. In general, we find that the magnetic properties of the recovered sediments are relatively uniform, with insignificant variations downhole. In Cores 344-U1380C-2R through 13R, silty clay and claystone with fine sandstone in Unit I (438.00–552.72 mbsf; see "Lithostratigraphy and petrology") have an NRM intensity between 1.9×10^{-4} and 8.6×10^{-1} A/m, with a mean of 6.2×10^{-3} A/m. NRM intensity for the clayey siltstone, coarse, shell-rich sand, and sandstone in Unit II (552.72–771.62 mbsf) is somewhat higher than in Unit I (ranging from 2.1×10^{-4} to 3.6×10^{-1} A/m, with a mean of 2.0×10^{-2} A/m). Several peaks of higher NRM intensity exist in some depth intervals in Unit II. The high-intensity peaks remained even after 30 mT AF demagnetization, suggesting that it is unlikely that they are caused entirely by drilling-induced remagnetization. Paleomagnetic measurements indicate that the silty claystone with fine sandstone in Unit III (771.62–800.00 mbsf) has NRM intensity ranging from 3.2×10^{-4} to 1.1×10^{-1} A/m, with a mean of 1.7×10^{-2} A/m. Variations in magnetic susceptibility generally follow variations in NRM intensity (see "Physical properties").

Since the beginning of DSDP in 1968, paleomagnetists have been aware of remagnetization acquired during drilling and/or recovery of cores (Stokking et al., 1993). This remagnetization is characterized by NRM inclinations that are strongly biased toward a steep downward inclination that can be removed at initial stages of demagnetization. In Hole U1380C, however, we were able to use this remagnetization to correct the orientation error for one discrete sample.

As shown in Figure F34A, the drilling overprint from Sample 344-U1380C-51R-2W, 65–67 cm (788.86 mbsf), has a steep upward inclination, which is opposite to the drilling overprint component from all other samples, as well as those from the corresponding section-half interval during the pass-through section measurement (i.e., steep downward; Fig. F34B, F34C). In this case, the overprint component served as a useful check. By putting this discrete sample back to its original cored position, we found that the orientation arrow in this sample was marked 180° away from the correct direction; that is, instead of the –*z*-direction, it was marked in the +*z*-direction and measured on the SRM.

Paleomagnetic demagnetization results

For the recovered sediment core sections, we employed AF demagnetization steps up to 30 mT. AF demagnetization to 5–15 mT was generally effective in removing the drilling overprint magnetization, as shown by inclinations shifting toward shallower values and by a significant decrease in magnetization intensity (Fig. F33). Although the level of AF demagnetization we applied did not always remove the overprint, ChRM directions can generally be isolated from the pass-through measurements. An example of good-quality AF demagnetization results is shown in Figure F35A.

The remanent magnetization of 60 discrete samples from the three lithostratigraphic units in Hole U1380C was investigated using stepwise AF and thermal demagnetization. In most cases, ChRM is revealed after the removal of the drilling-induced component (Fig. F35). Most thermally demagnetized samples show unblocking temperatures between 175° and 250°C, indicating that the main magnetic carriers in these samples have low Curie temperatures.

Magnetostratigraphy

Because a rotary coring technique was used to recover cores in Hole U1380C, we used ChRM inclinations from both discrete and pass-through measurements to define magnetic polarity sequences. As shown in Figure F36, several magnetic reversals were discerned on the basis of changes in inclination sign.

Samples from Unit III are dominated by normal polarity. Within Units I and II, samples mainly have reversed polarity. Some normal polarity samples are also present in the middle part of the hole. Shipboard micropaleontological studies suggest that Core 344-U1380C-50R should be older than 2.39 Ma (see "Paleontology and biostratigraphy"). Consequently, the Matuyama/Gauss Chron boundary (2.581 Ma in Gradstein et al., 2012) is tentatively placed at ~770 mbsf.

Within the Matuyama Chron (Fig. F36), the two relatively short and well-defined normal polarity intervals at ~730–764 mbsf may represent Chron C2r.1n (Reunion Subchron; 2.128–2.148 Ma). The interval (633.91–666.61 mbsf) of Sections 344-U1380C-22R-2, 125 cm, to 26R-1, 60 cm, shows normal inclinations, consistent with this interval possibly being the normal polarity Chron C2n (Olduvai Subchron; 1.778–1.945 Ma). Above 633.91 mbsf, some single normal polarity samples are recognized but do not define any consistent normal magnetozones (Fig. F36). At this time, we are not inclined to correlate them with the geomagnetic polarity timescale because they are defined by limited data points and are tentative. Shore-based paleomagnetic studies will be conducted to improve the magnetostratigraphy at Site U1380.

Anisotropy of magnetic susceptibility

For two representative samples taken from Core 344-U1380C-13R (a major shear zone; see "Structural geology"), anisotropy of magnetic susceptibility (AMS) was measured with the Kappabridge KLY 4S before and after progressive AF demagnetization (up to 180 and 200 mT, respectively). The difference in AMS results before and after AF demagnetization was checked with the two samples, and there was no significant difference found for the K_{min} of these samples. Mean volume magnetic susceptibilities showed only minor changes through demagnetization from 1.356×10^{-4} to 1.381×10^{-4} SI for Sample 344-U1380C-13R-1, 28–30 cm, and from 1.72×10^{-4} to 1.6599×10^{-4} SI for Sample 344-U1380C-13R-4, 62–64 cm. For both samples, the shape parameter is positive, indicating an oblate shape of the ellipsoid. Although it is recommended to make AMS measurements before AF demagnetization (e.g., Jordanova et al., 2007), our preliminary results indicate that we can use AMS after AF demagnetization on sediment layers recovered at Site U1380.

References

Bekins, B., McCaffrey, A.M., and Dreiss, S.J., 1994. Influence of kinetics on the smectite to illite transition in the Barbados accretionary prism. *J. Geophys. Res.: Solid Earth,* 99(B9):18147–18158. doi:10.1029/94JB01187

Bullard, E.C., 1939. Heat flow in South Africa. *Proc. R. Soc. A,* 173(955):474–502. doi:10.1098/rspa.1939.0159

Expedition 334 Scientists, 2012a. Site U1378. *In* Vannucchi, P., Ujiie, K., Stroncik, N., Malinverno, A., and the Expedition 334 Scientists, *Proc. IODP,* 334: Tokyo (Integrated Ocean Drilling Program Management International, Inc.). doi:10.2204/iodp.proc.334.103.2012

Expedition 334 Scientists, 2012b. Site U1379. *In* Vannucchi, P., Ujiie, K., Stroncik, N., Malinverno, A., and the

Expedition 334 Scientists, *Proc. IODP,* 334: Tokyo (Integrated Ocean Drilling Program Management International, Inc.). **doi:10.2204/iodp.proc.334.104.2012**

Expedition 334 Scientists, 2012c. Site U1380. *In* Vannucchi, P., Ujiie, K., Stroncik, N., Malinverno, A., and the Expedition 334 Scientists, *Proc. IODP,* 334: Tokyo (Integrated Ocean Drilling Program Management International, Inc.). **doi:10.2204/iodp.proc.334.105.2012**

Fontanier, C., Jorissen, F.J., Chaillou, G., David, C., Anschutz, P., and Lafon, V., 2003. Seasonal and interannual variability of benthic foraminiferal faunas at 550 m depth in the Bay of Biscay. *Deep-Sea Res., Part I,* 50(4):457–494. **doi:10.1016/S0967-0637(02)00167-X**

Gradstein, F.M., Ogg, J.G., Schmitz, M.D., and Ogg, G.M. (Eds)., 2012. *The Geological Time Scale 2012:* Amsterdam (Elsevier).

Harris, R.N., Sakaguchi, A., Petronotis, K., Baxter, A.T., Berg, R., Burkett, A., Charpentier, D., Choi, J., Diz Ferreiro, P., Hamahashi, M., Hashimoto, Y., Heydolph, K., Jovane, L., Kastner, M., Kurz, W., Kutterolf, S.O., Li, Y., Malinverno, A., Martin, K.M., Millan, C., Nascimento, D.B., Saito, S., Sandoval Gutierrez, M.I., Screaton, E.J., Smith-Duque, C.E., Solomon, E.A., Straub, S.M., Tanikawa, W., Torres, M.E., Uchimura, H., Vannucchi, P., Yamamoto, Y., Yan, Q., and Zhao, X., 2013a. Input Site U1381. In Harris, R.N., Sakaguchi, A., Petronotis, K., and the Expedition 344 Scientists, *Proc IODP,* 344: College Station, TX (Integrated Ocean Drilling Program). **doi:10.2204/iodp.proc.344.103.2013**

Harris, R.N., Sakaguchi, A., Petronotis, K., Baxter, A.T., Berg, R., Burkett, A., Charpentier, D., Choi, J., Diz Ferreiro, P., Hamahashi, M., Hashimoto, Y., Heydolph, K., Jovane, L., Kastner, M., Kurz, W., Kutterolf, S.O., Li, Y., Malinverno, A., Martin, K.M., Millan, C., Nascimento, D.B., Saito, S., Sandoval Gutierrez, M.I., Screaton, E.J., Smith-Duque, C.E., Solomon, E.A., Straub, S.M., Tanikawa, W., Torres, M.E., Uchimura, H., Vannucchi, P., Yamamoto, Y., Yan, Q., and Zhao, X., 2013b. Methods. In Harris, R.N., Sakaguchi, A., Petronotis, K., and the Expedition 344 Scientists, *Proc IODP,* 344: College Station, TX (Integrated Ocean Drilling Program). **doi:10.2204/iodp.proc.344.102.2013**

Jordanova, D., Jordanova, N., Henry, B., Hus, J., Bascou, J., Funaki, M., and Dimov, D., 2007. Changes in mean magnetic susceptibility and its anisotropy of rock samples as a result of alternating field demagnetization. *Earth Planet. Sci. Lett.,* 255(3–4):390–401. **doi:10.1016/j.epsl.2006.12.025**

Kirschvink, J.L., 1980. The least-squares line and plane and the analysis of palaeomagnetic data. *Geophys. J. R. Astron. Soc.,* 62(3):699–718. **doi:10.1111/j.1365-246X.1980.tb02601.x**

Perry, E., and Hower, J., 1970. Burial diagenesis in Gulf Coast pelitic sediments. *Clays Clay Miner.,* 18:165–177. **doi:10.1346/CCMN.1970.0180306**

Sen Gupta, B.K., and Machain-Castillo, M.L., 1993. Benthic foraminifera in oxygen-poor habitats. *Mar. Micropaleontol.,* 20(3–4):183–201. **doi:10.1016/0377-8398(93)90032-S**

Stokking, L., Musgrave, R., Bontempo, D., Autio, W., Rabinowitz, P.D., Baldauf, J., and Francis, T.J.G., 1993. Handbook for shipboard paleomagnetists. *ODP Tech. Note,* 18. **doi:10.2973/odp.tn.18.1993**

Wei, W., Kastner, M., Rosenbauer, R., Chan, L.H., and Weinstein, Y., 2010. Alkali elements as geothermometers for ridge flanks and subduction zones. *In* Birkle, P., and Torres Alvarado, I.S. (Eds.), *Water-Rock Interaction XIII:* London (Taylor & Francis), 223–226.

You, C.-F., and Gieskes, J.M., 2001. Hydrothermal alteration of hemi-pelagic sediments: experimental evaluation of geochemical processes in shallow subduction zones. *Appl. Geochem.,* 16(9–10):1055–1066. **doi:10.1016/S0883-2927(01)00024-5**

Zijderveld, J.D.A., 1967. AC demagnetization of rocks: analysis of results. *In* Collinson, D.W., Creer, K.M., and Runcorn, S.K. (Eds.), *Methods in Palaeomagnetism:* Amsterdam (Elsevier), 254–286.

Publication: 11 December 2013
MS 344-106

Figure F1. Detail of prestack time-migrated seismic Line BGR99-7 centered at Site U1380. Prestack depth migration from C.R. Ranero (unpubl. data). Site U1378 was drilled during Expedition 334 in 2011.

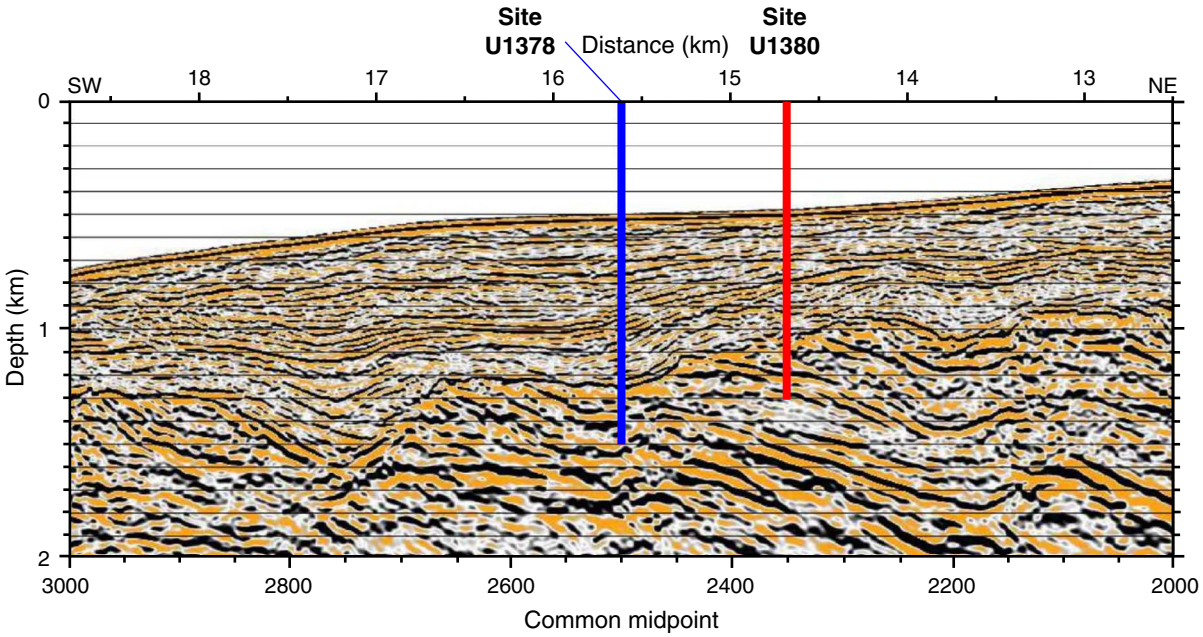

Figure F2. Location of Expedition 344 drill sites. Red diamonds denote Expedition 344 sites (U1380, U1381, and U1412–U1414) and yellow diamonds denote Expedition 334 sites not occupied during Expedition 344 (U1378, U1379). Red lines = 3-D seismic survey, black lines = seismic reflection lines. Numbers along the short and long axes of the 3-D survey represent inlines and crosslines, respectively.

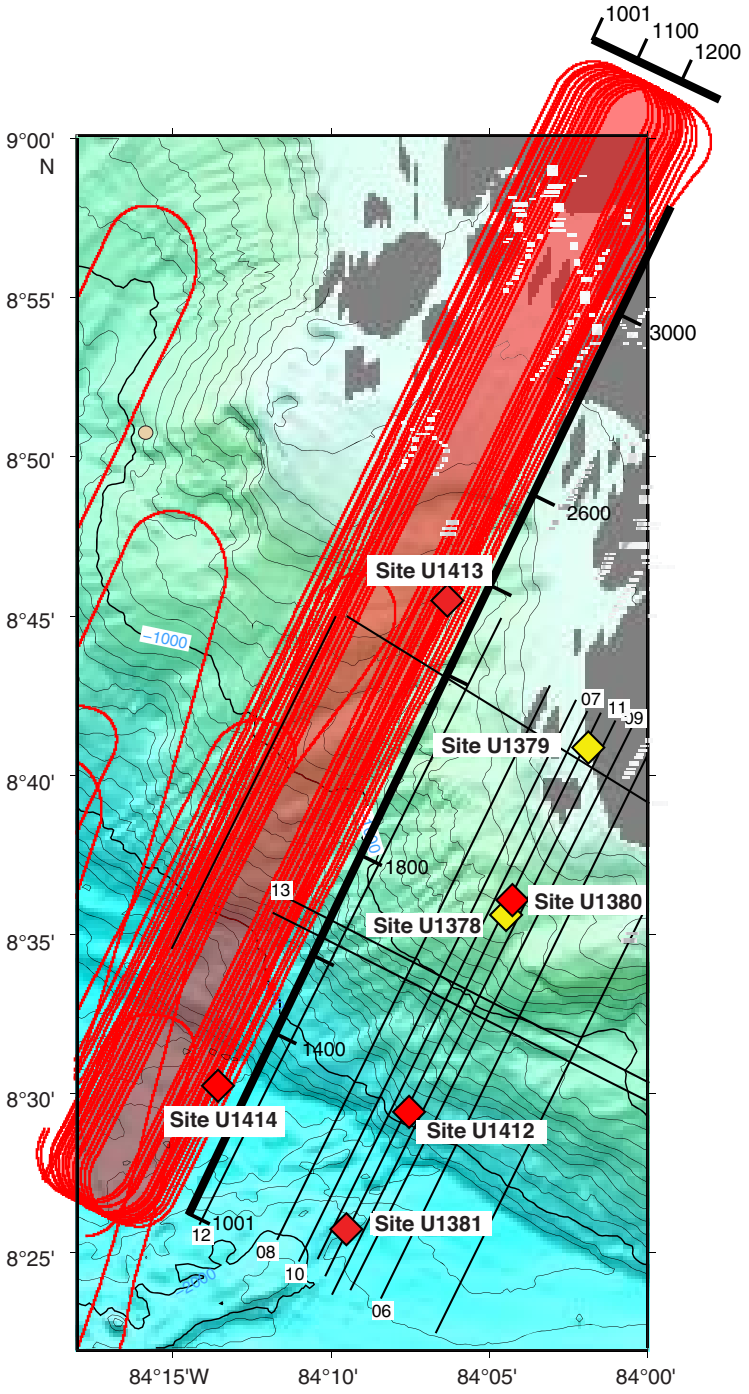

Figure F3. Reentry cone, 16 inch casing string, and 10¾ inch casing string deployed in Hole U1380C. ID = inner diameter. BHA = bottom-hole assembly

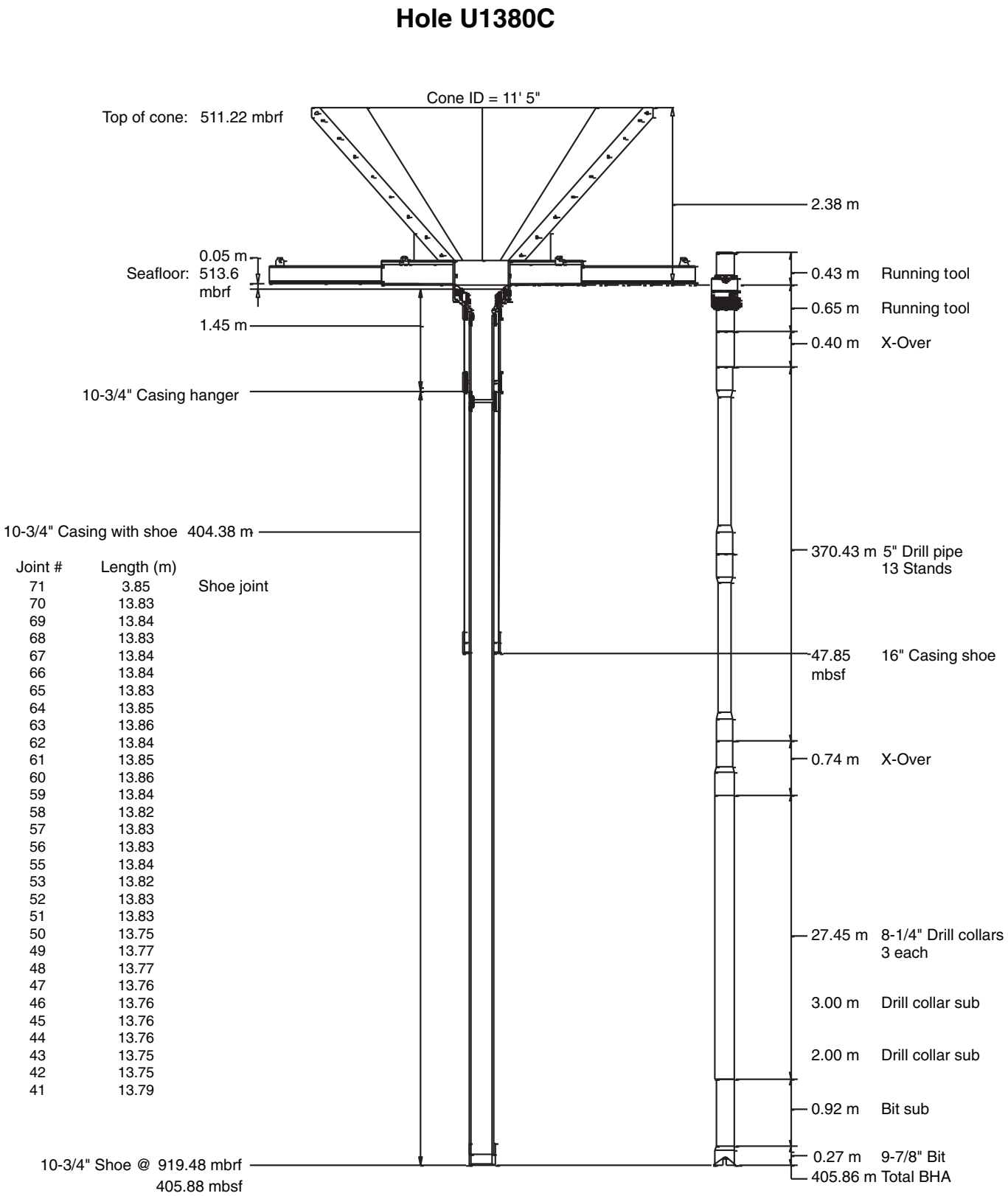

Figure F4. Logging data, Hole U1380C. **A.** Inferred top depth of the 10¾ inch casing string. (Continued on next page.)

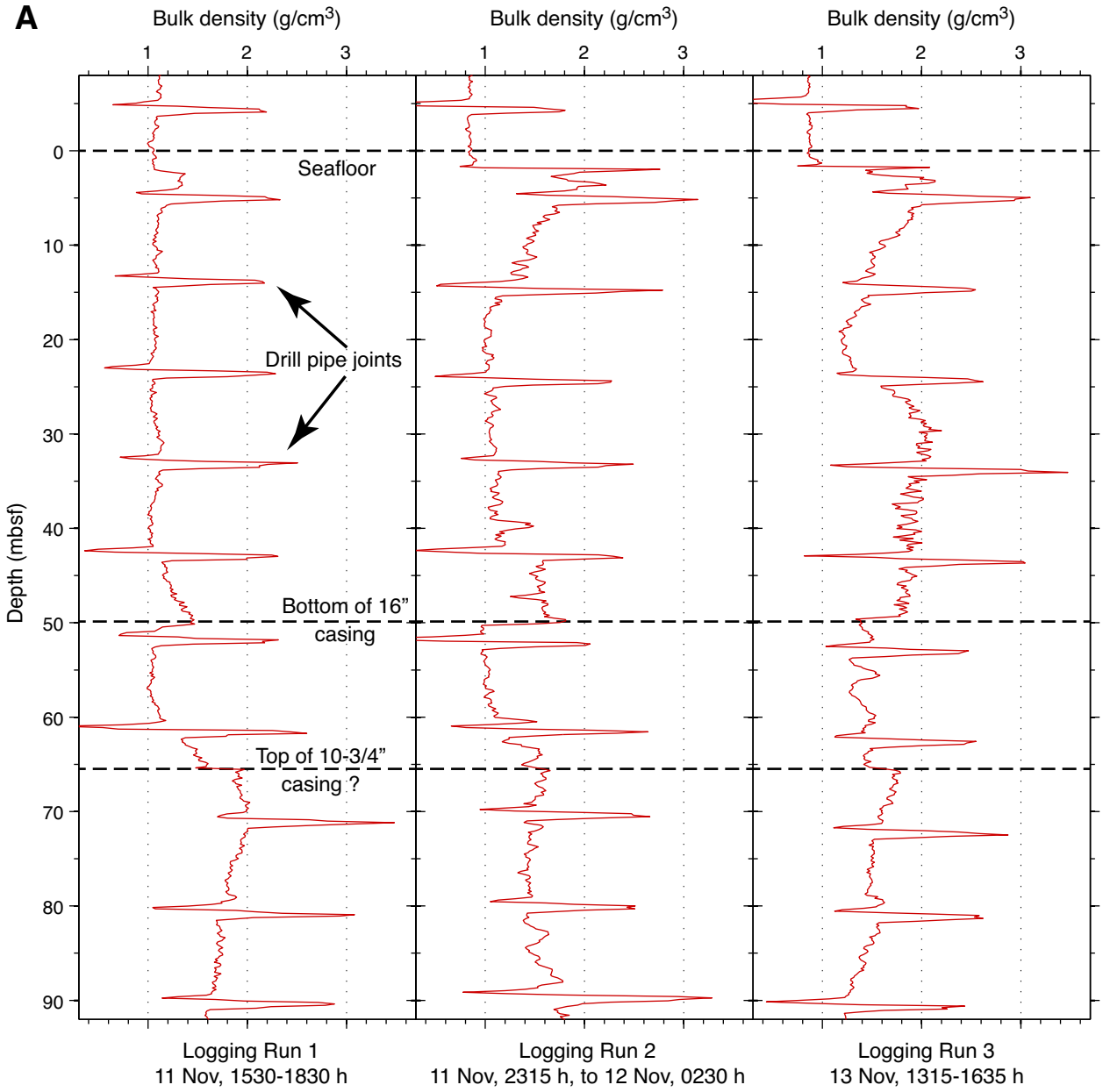

Figure F4 (continued). B. Inferred bottom depth of the 10¾ inch casing string.

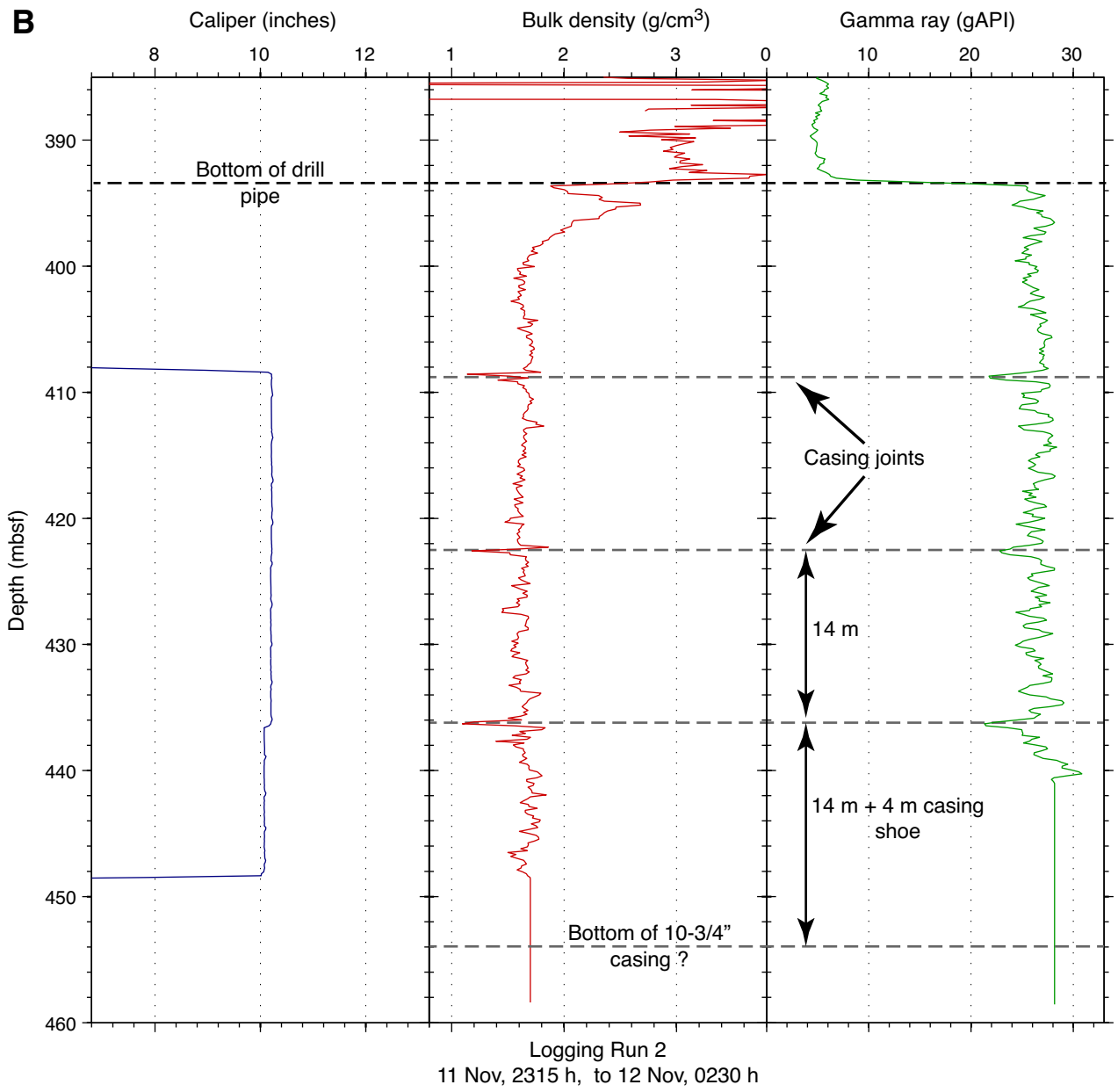

Figure F5. Lithostratigraphic summary of Hole U1380C.

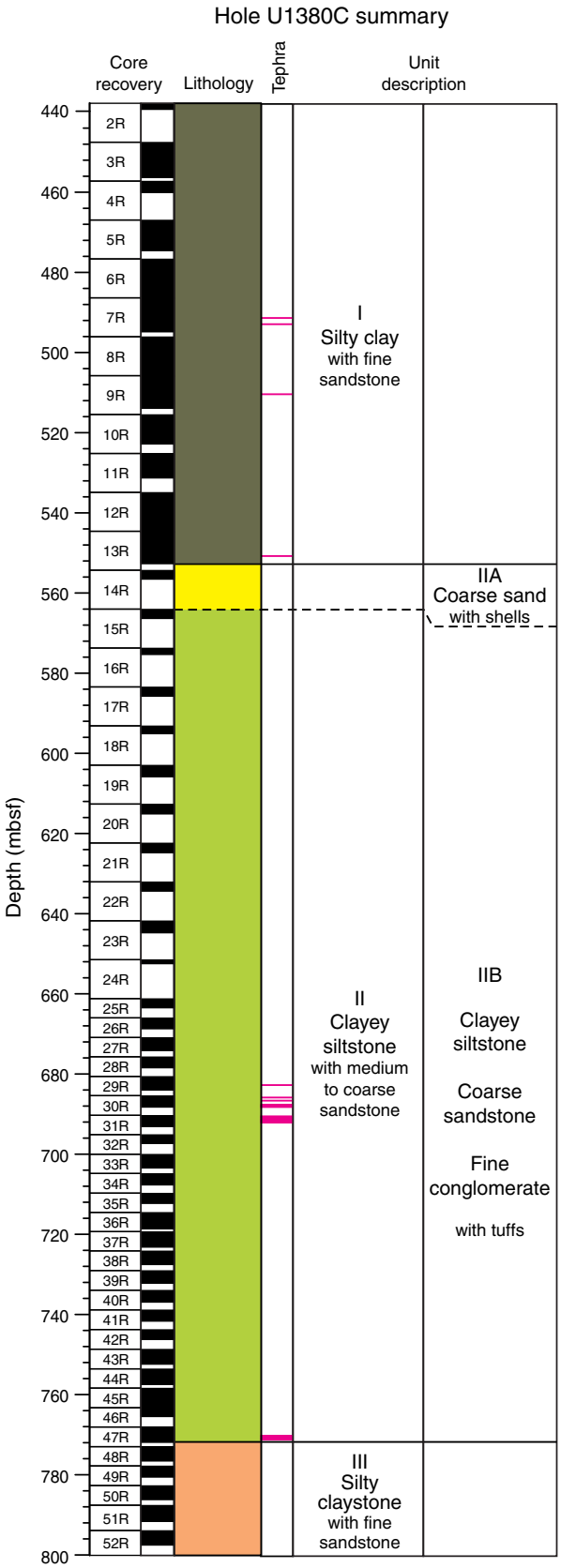

Figure F6. Representative digital image of lithostratigraphic Unit I; dark grayish green massive silty clay (interval 344-U1380C-11R-1A, 56–79 cm).

Figure F7. Representative digital image of Subunit IIA; dark greenish gray medium to coarse sandstone (interval 344-U1380C-14R-2A, 35–49 cm). Note abundant shell fragments.

Figure F8. Digital image of lower contact between fine conglomerate and siltstone in Subunit IIB (interval 344-U1380C-31R-1A, 96–122 cm).

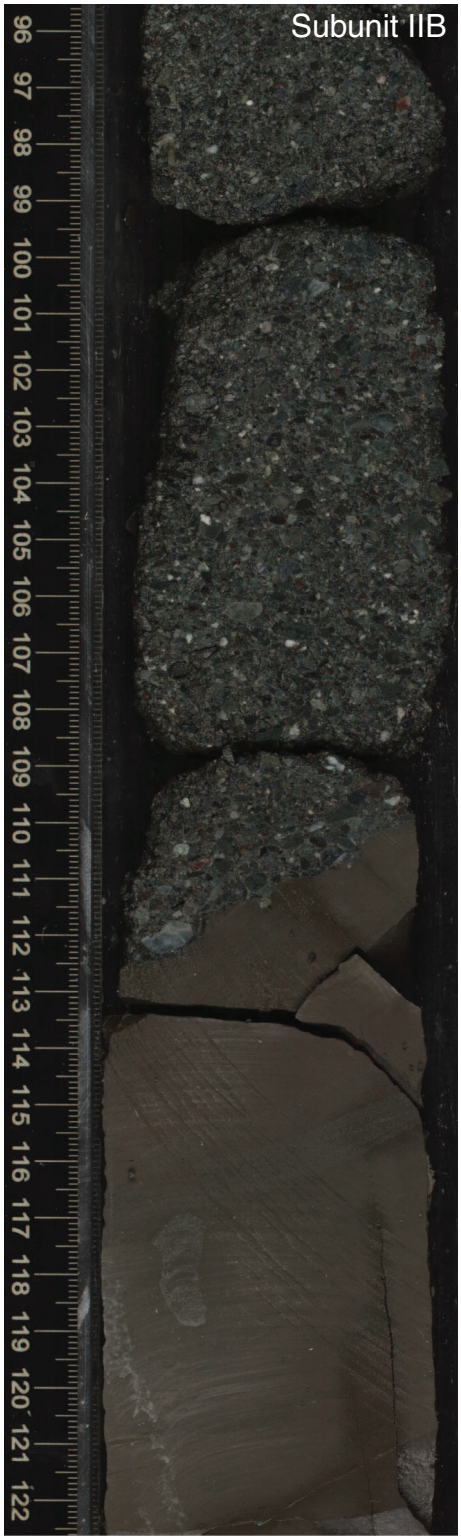

Figure F9. Digital image of load casts and soft-sediment deformation features resulting from liquefaction (interval 344-U1380C-47R-1A, 74–113 cm).

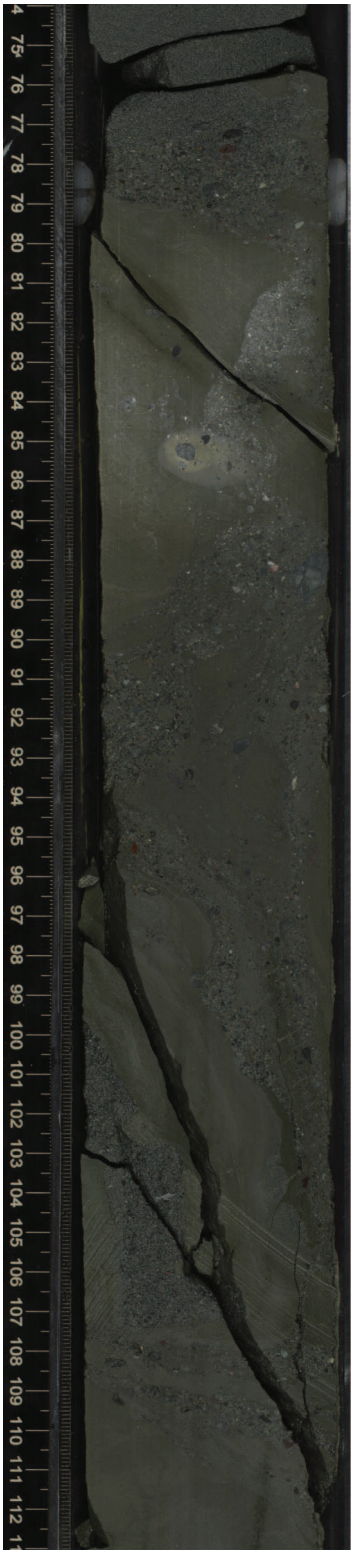

Figure F10. Digital image of sapropel horizons along sandstone laminations (interval 344-U1380C-33R-1A, 41–49 cm).

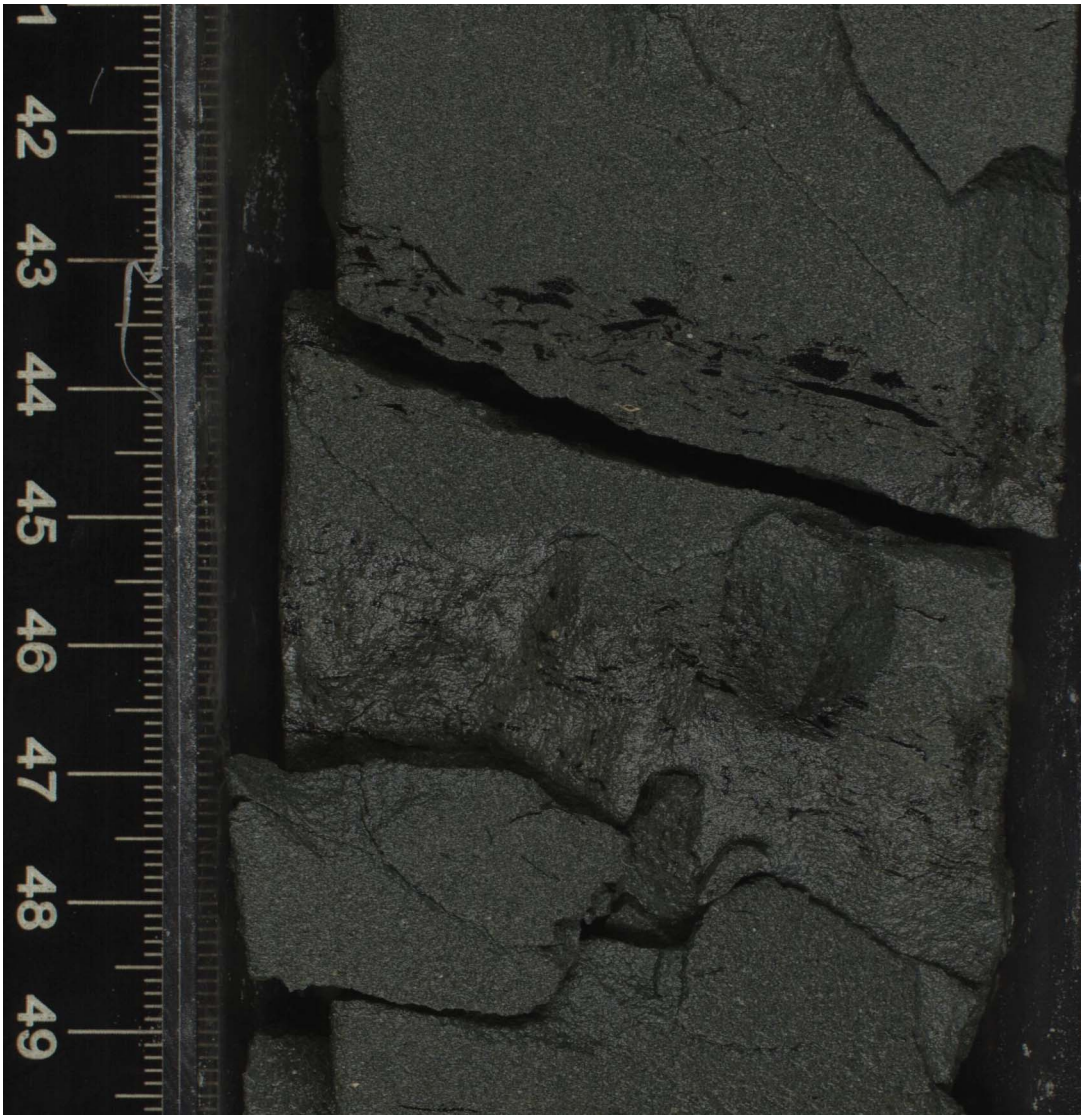

Figure F11. Digital image of pebble-sized conglomerate and rip-up clay clasts (interval 344-U1380C-47R-2A, 59–88 cm).

Figure F12. Digital image of dark greenish gray silty clay with moderate bioturbation that characterizes Unit III (interval 344-U1380C-49R-1A, 96–120 cm).

Figure F13. Typical X-ray diffraction patterns obtained for bulk rock samples, Hole U1380C. A = analcime, C = calcite, Chl = chlorite (clinochlore), H = heulandite, Ho = hornblende, L = laumontite, P = plagioclase, Py = pyrite, Q = quartz, S = smectite.

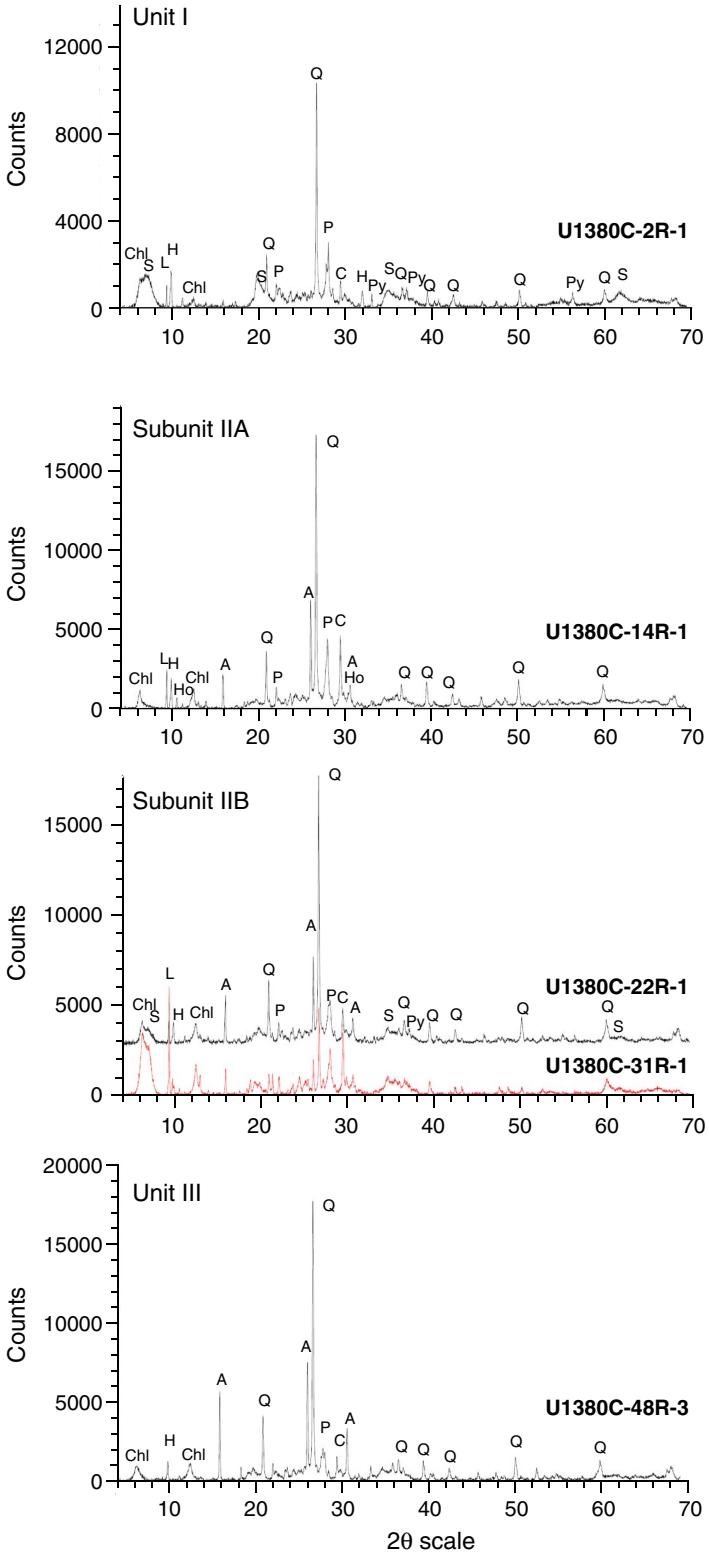

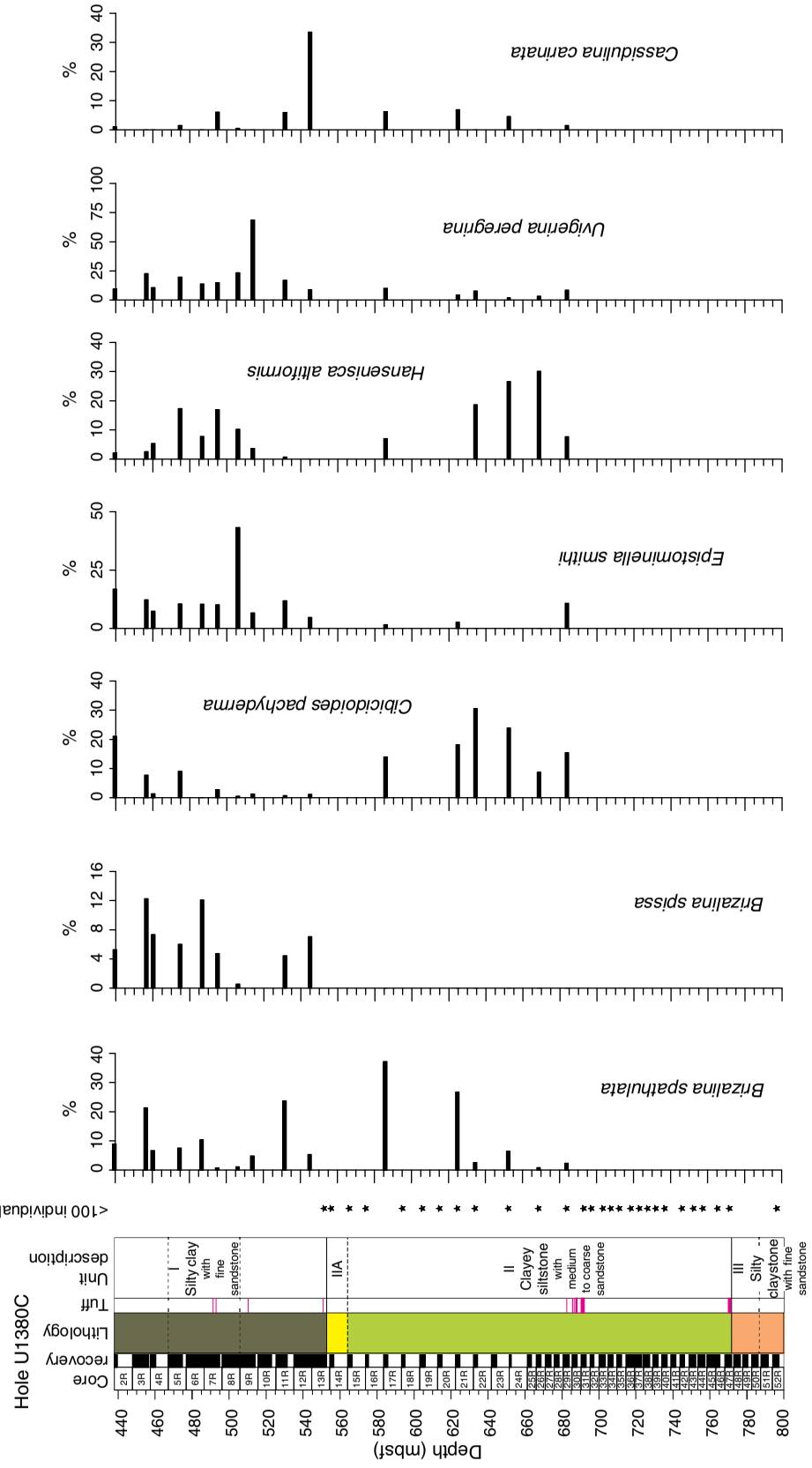

Figure F14. Benthic foraminifer assemblage changes between the upper and lower units of Hole U1380C. Samples containing <100 individuals per sample (marked with an asterisk [*]) were not used for relative abundance calculations.

Figure F15. Plot of bedding dip angles, dip angles of faults, and other fractures as a function of depth, Hole U1380C. Purple bands across figure indicate breccia/fracture zones.

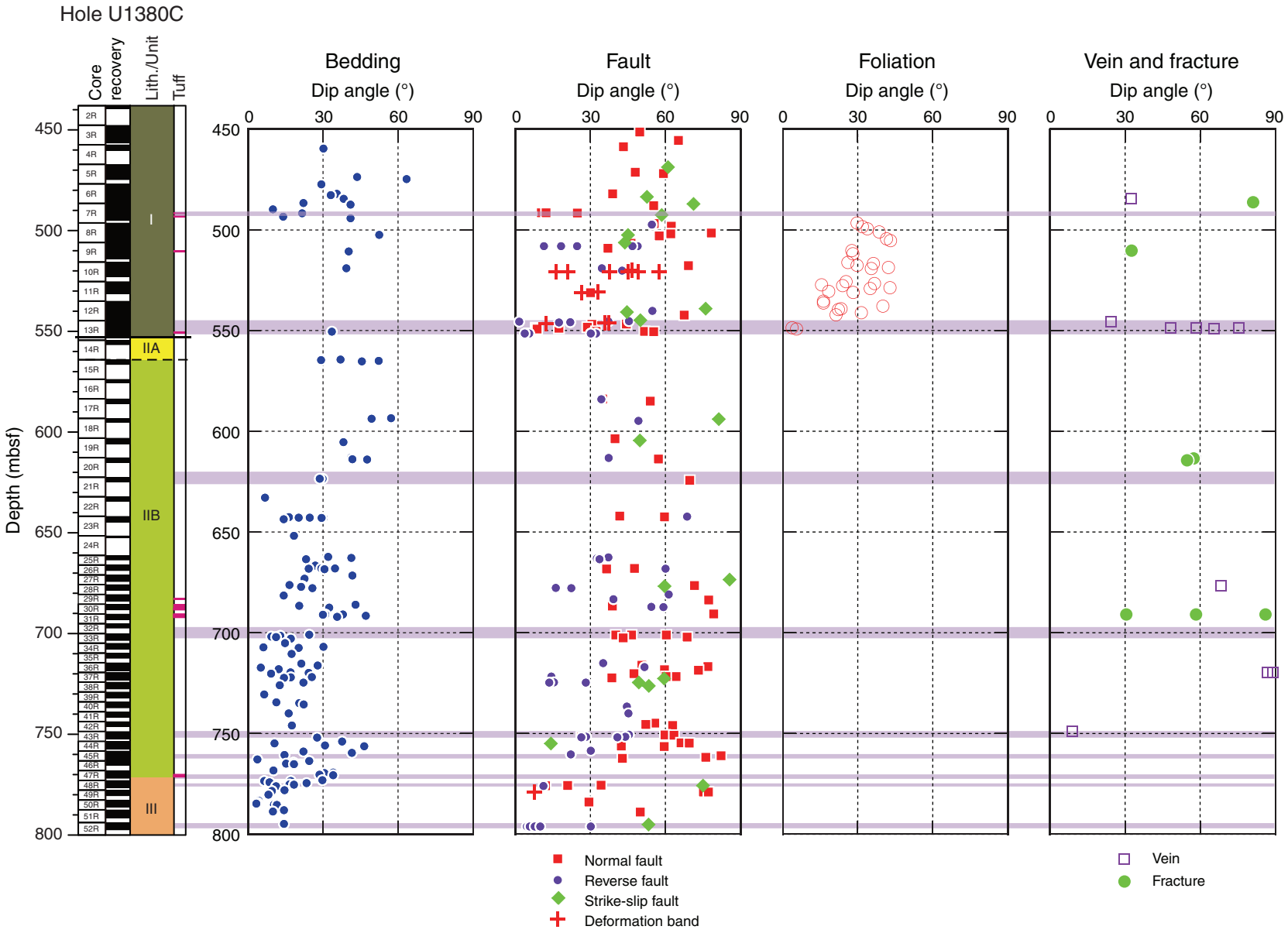

Figure F16. Stereographic diagrams showing (**A**) bedding planes and (**B**) fault kinematics after paleomagnetic correction, Hole U1380C.

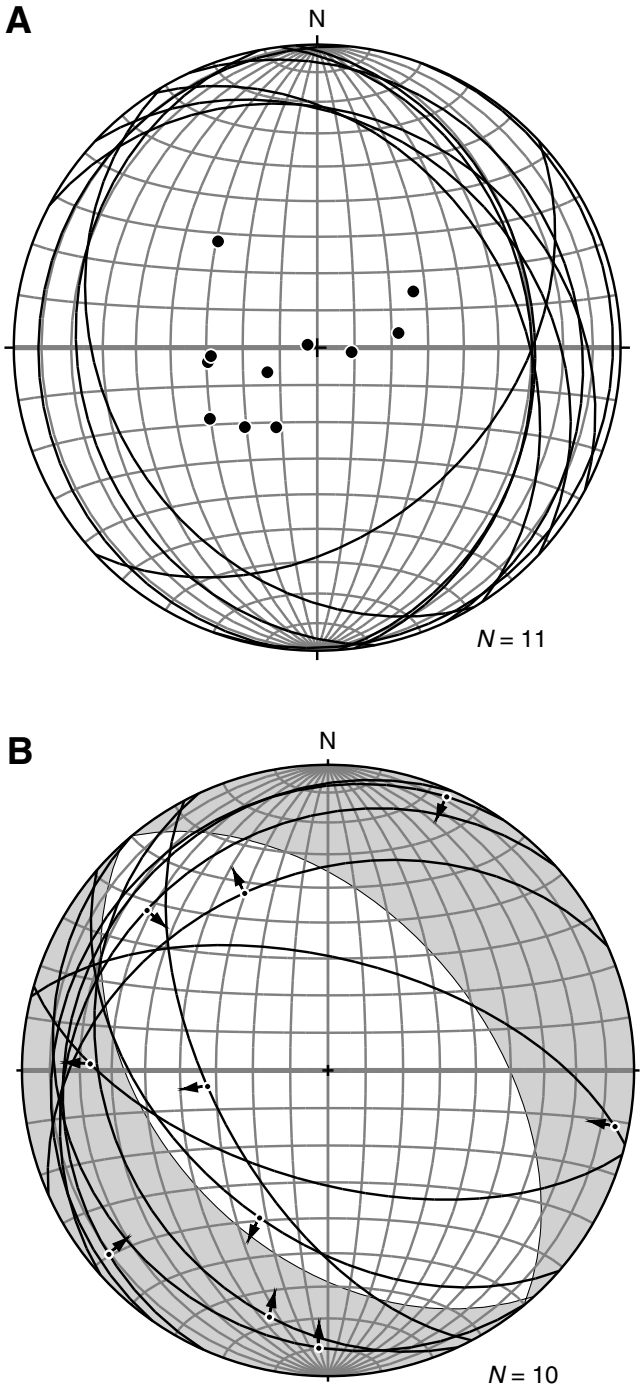

Figure F17. Photograph of fractured and brecciated zones in the lower fault zone between 453.8 and 477.7 mbsf (Sections 344-U1380C-13R-1 through 13R-7). Note the dominant fragment size <1 cm within the brecciated zone and the larger fragments within the fractured zone.

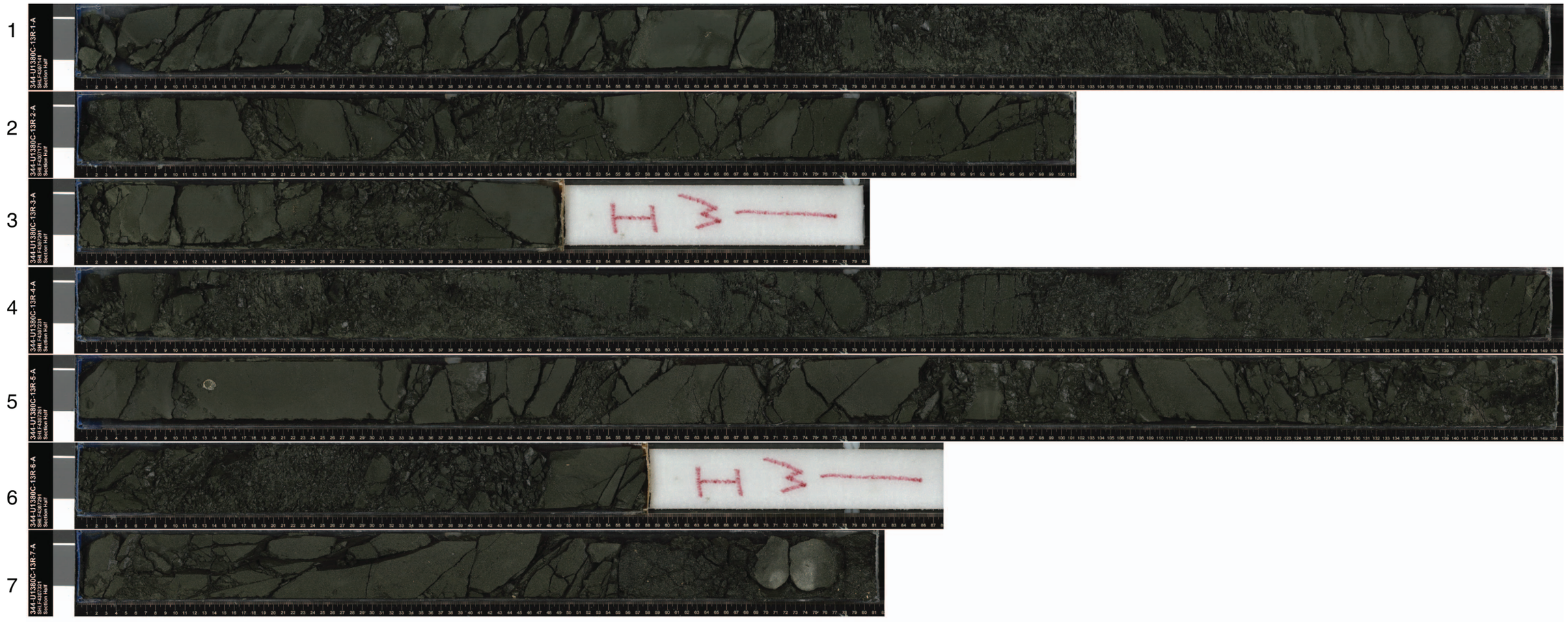

344-U1380C-13R-1 through 13R-7

Figure F18. Downhole profiles of salinity, chloride, sodium, potassium, and sodium/chloride ratio, Hole U1380C. Data collected in Holes U1378B and U1380A during Expedition 334 (Expedition 334 Scientists, 2012a, 2012c) are shown for comparison. Blue arrows = bottom seawater values.

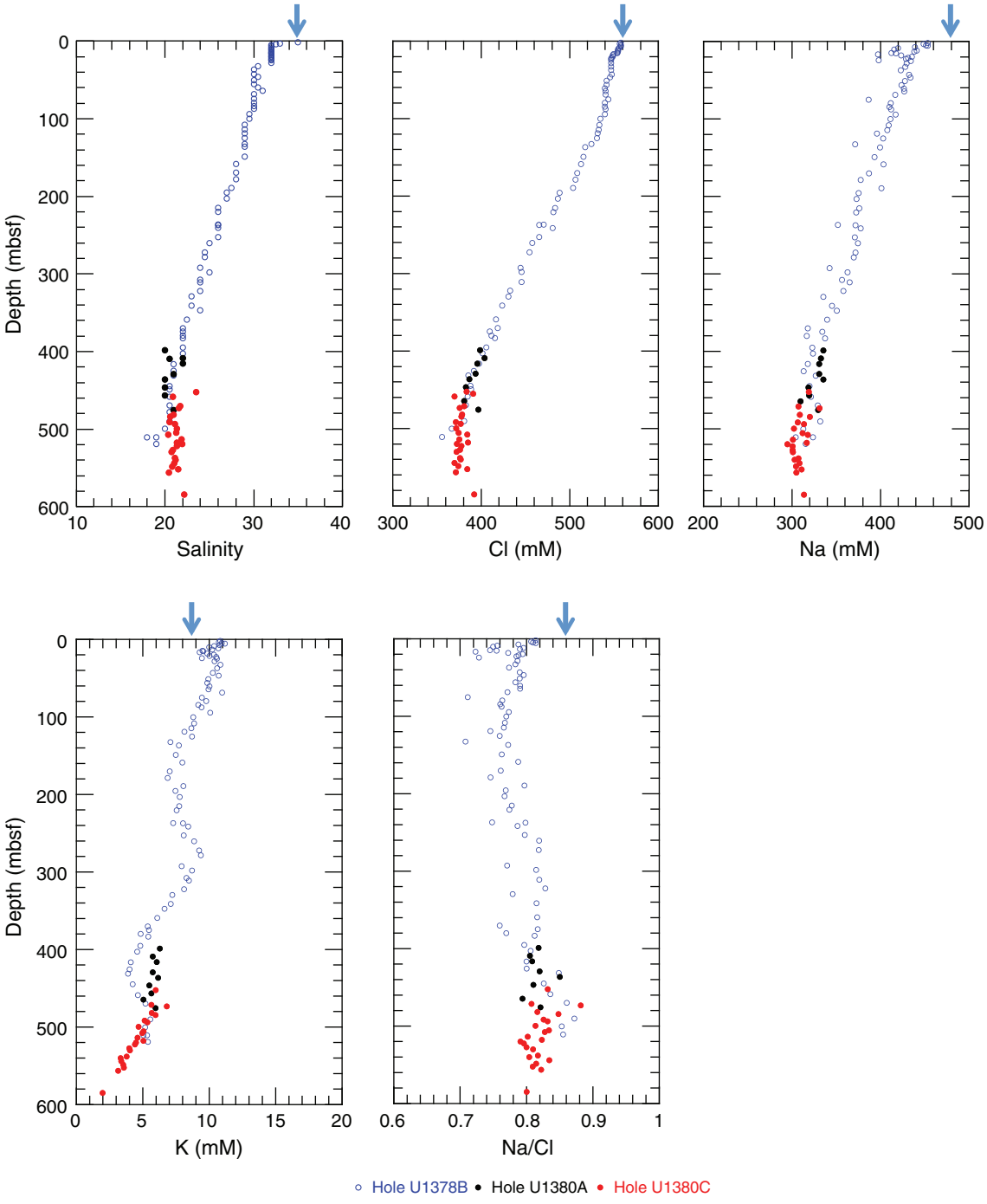

Figure F19. Downhole profiles of alkalinity, calcium, ammonium, and magnesium, Hole U1380C. Data collected in Holes U1378B and U1380A during Expedition 334 (Expedition 334 Scientists, 2012a, 2012c) are shown for comparison. Blue arrows = bottom seawater values.

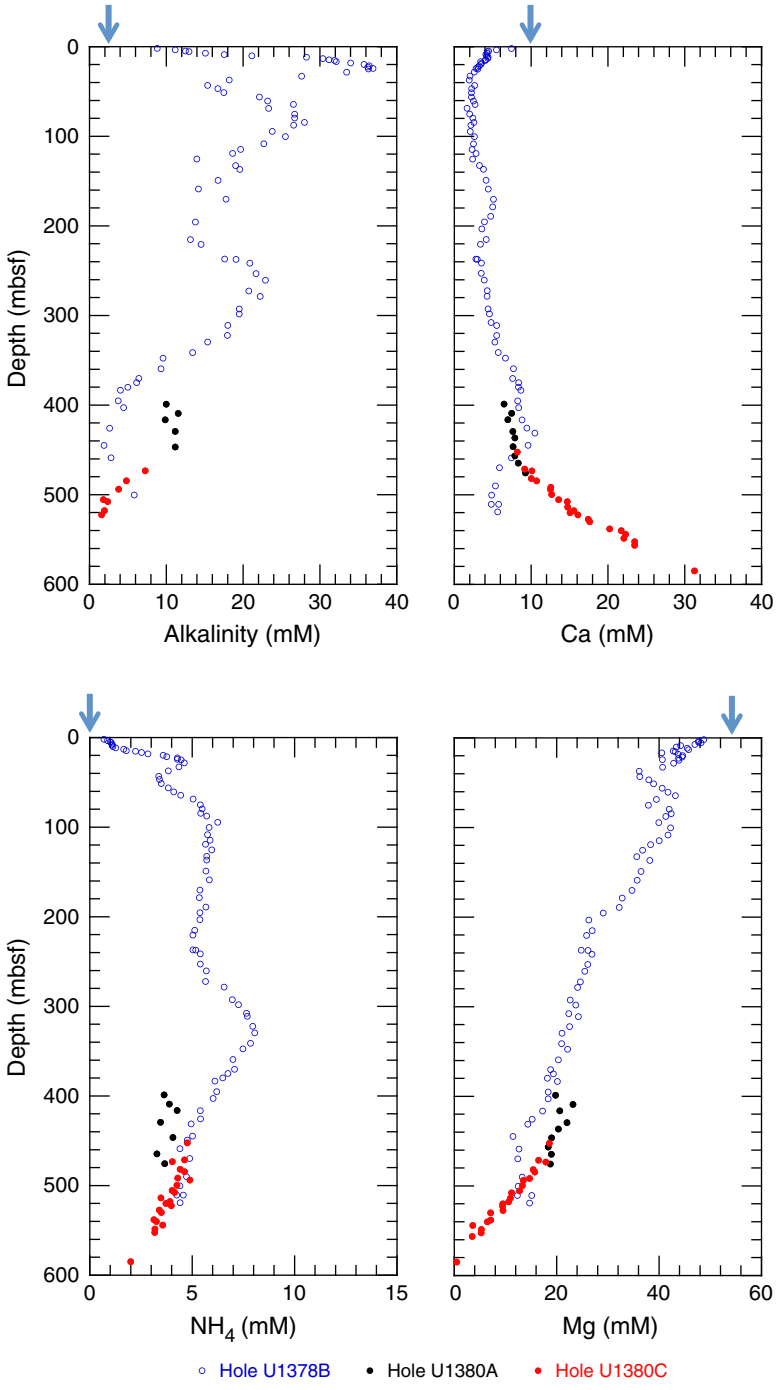

Figure F20. Downhole profiles of strontium, lithium, manganese, silica, boron, and barium, Hole U1380C. Data collected in Hole U1378B during Expedition 334 (M.E. Torres, unpubl. data) are shown for comparison. Blue arrows = bottom seawater values.

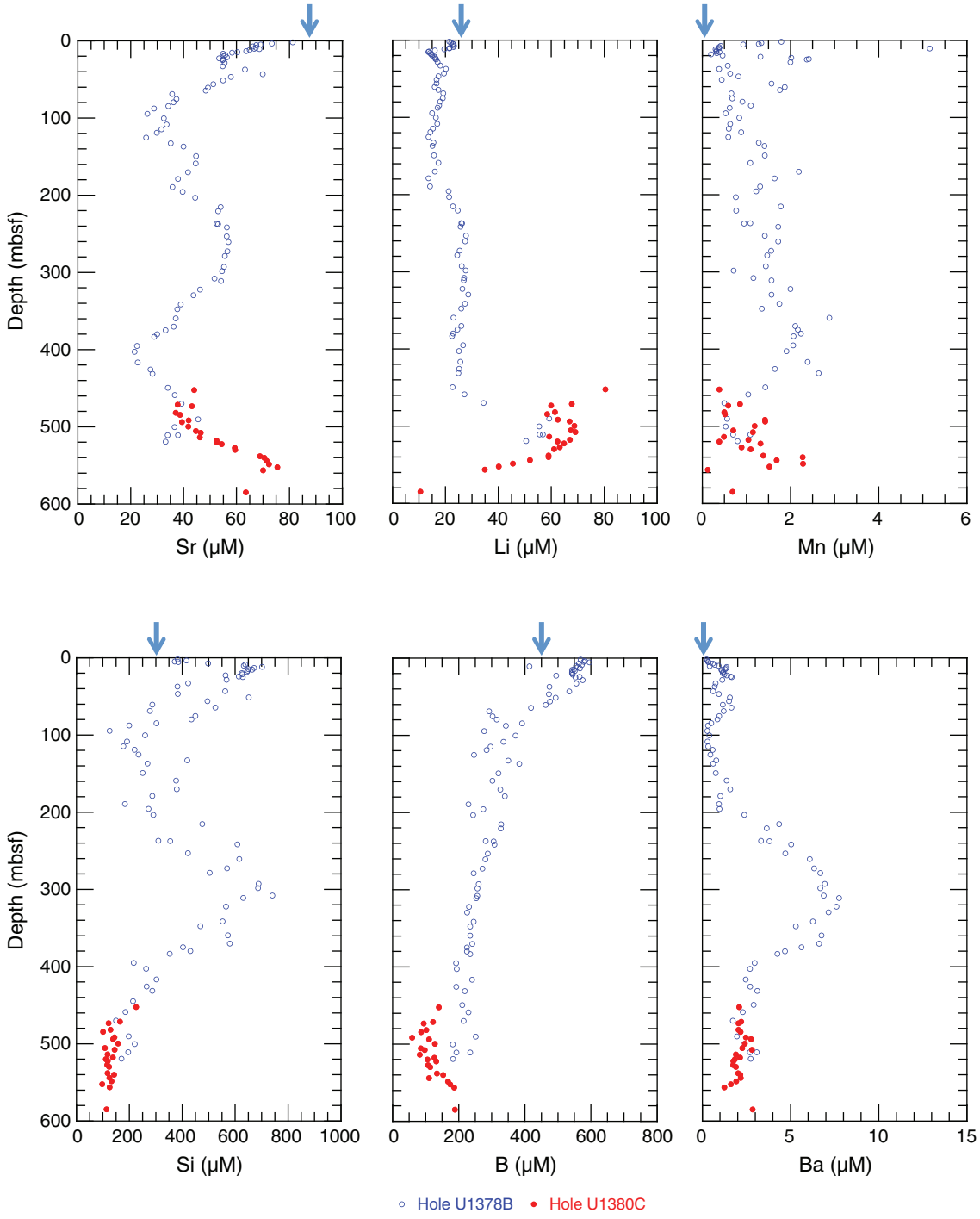

Figure F21. Downhole profiles of C_1/C_{2+} ratios in headspace samples, Hole U1380C. Data collected in Holes U1378B and U1380A during Expedition 334 (Expedition 334 Scientists, 2012a, 2012c) are shown for comparison.

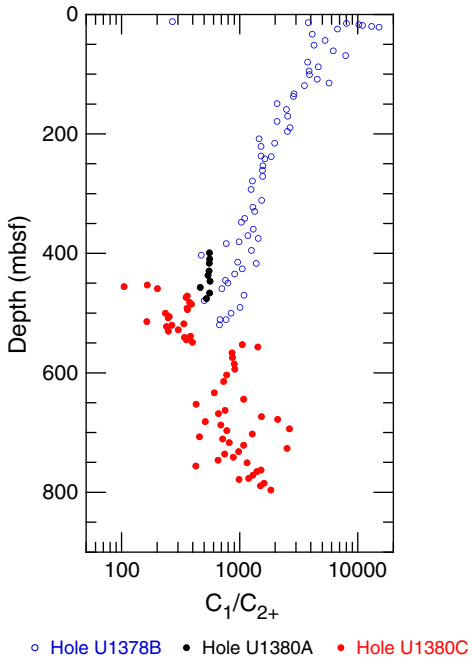

Figure F22. Downhole profiles of hydrocarbons in headspace gas, Hole U1380C.

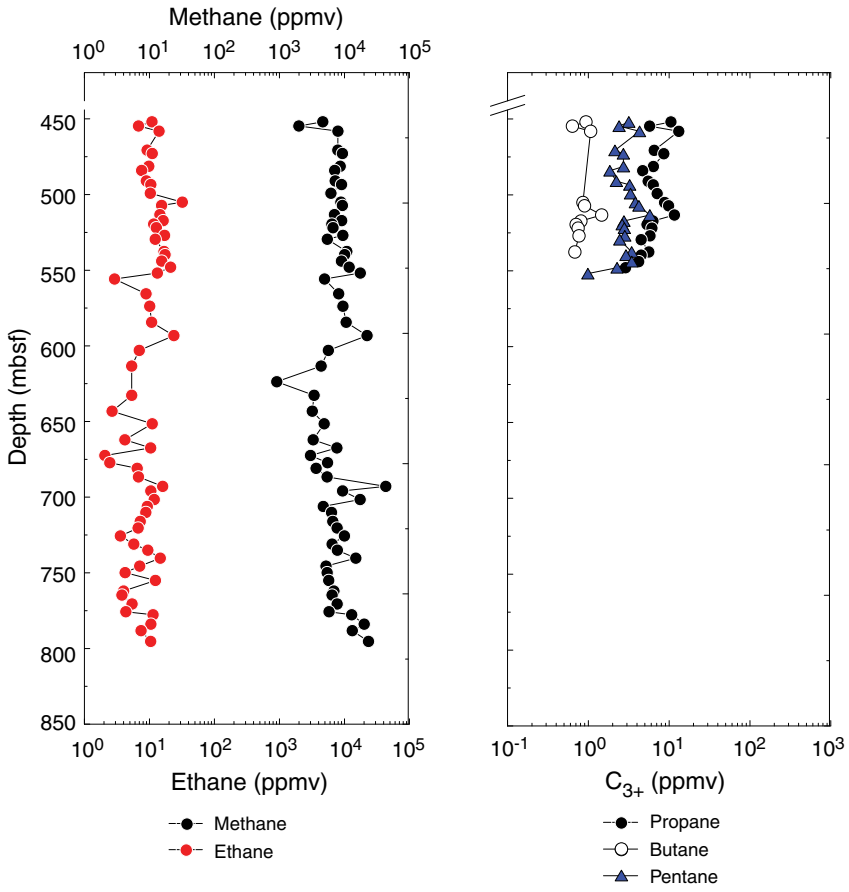

Figure F23. Downhole profiles of total carbon, inorganic carbon, and total organic carbon, Hole U1380C. Dashed lines = lithostratigraphic unit boundaries.

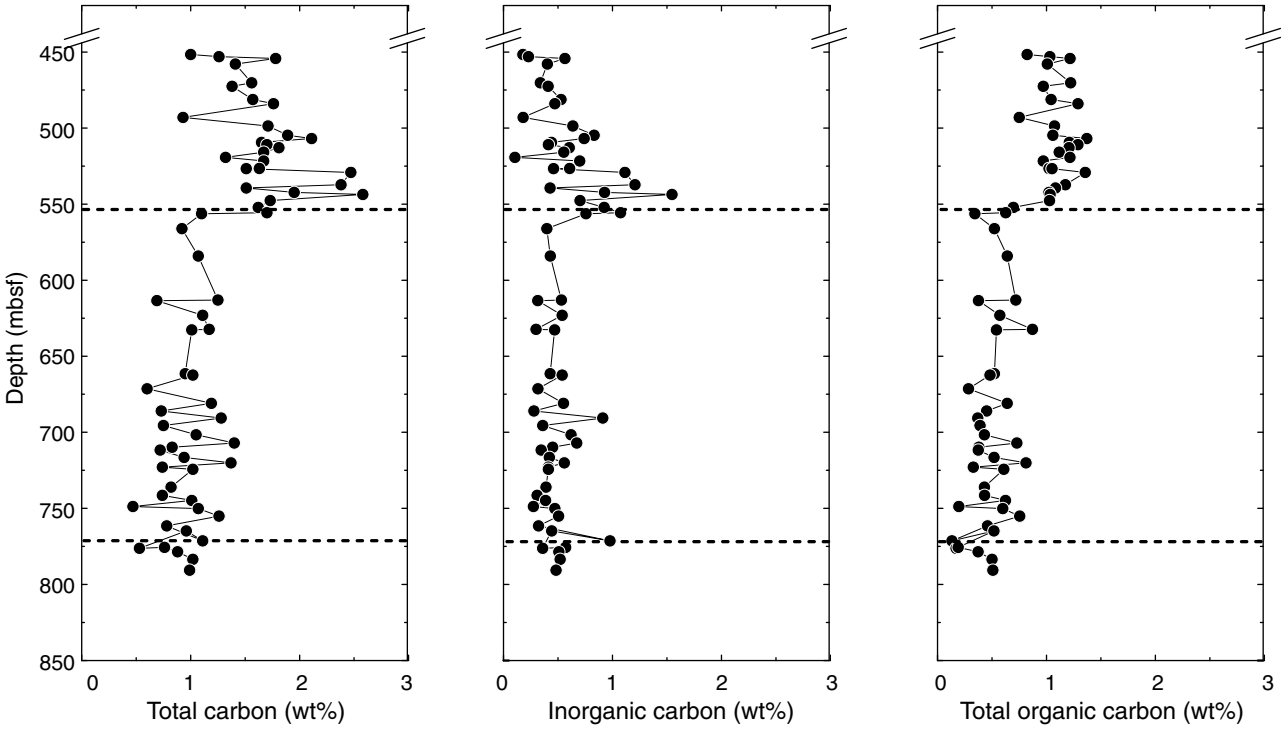

Figure F24. Gamma ray attenuation (GRA) density from the WRMSL and wet bulk density from discrete samples using moisture and density (MAD) mass/volume Method C, Site U1380. Horizontal lines = lithostratigraphic unit boundaries.

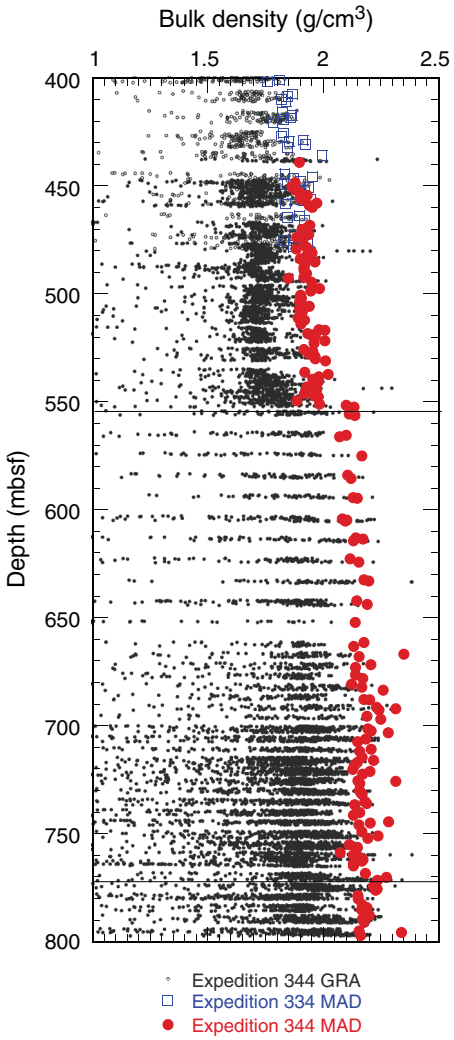

Figure F25. Discrete sample porosity and density using MAD mass/volume Method C, Hole U1380C, with Expedition 334 data. **A.** Wet bulk density. **B.** Grain density. **C.** Porosity. Horizontal lines = lithostratigraphic unit boundaries. Orange line = best-fit exponential porosity-depth relationship for upper 550 m of Sites U1378 and U1380 (porosity = 0.68exp(–0.0008 × depth); R^2 = 0.75).

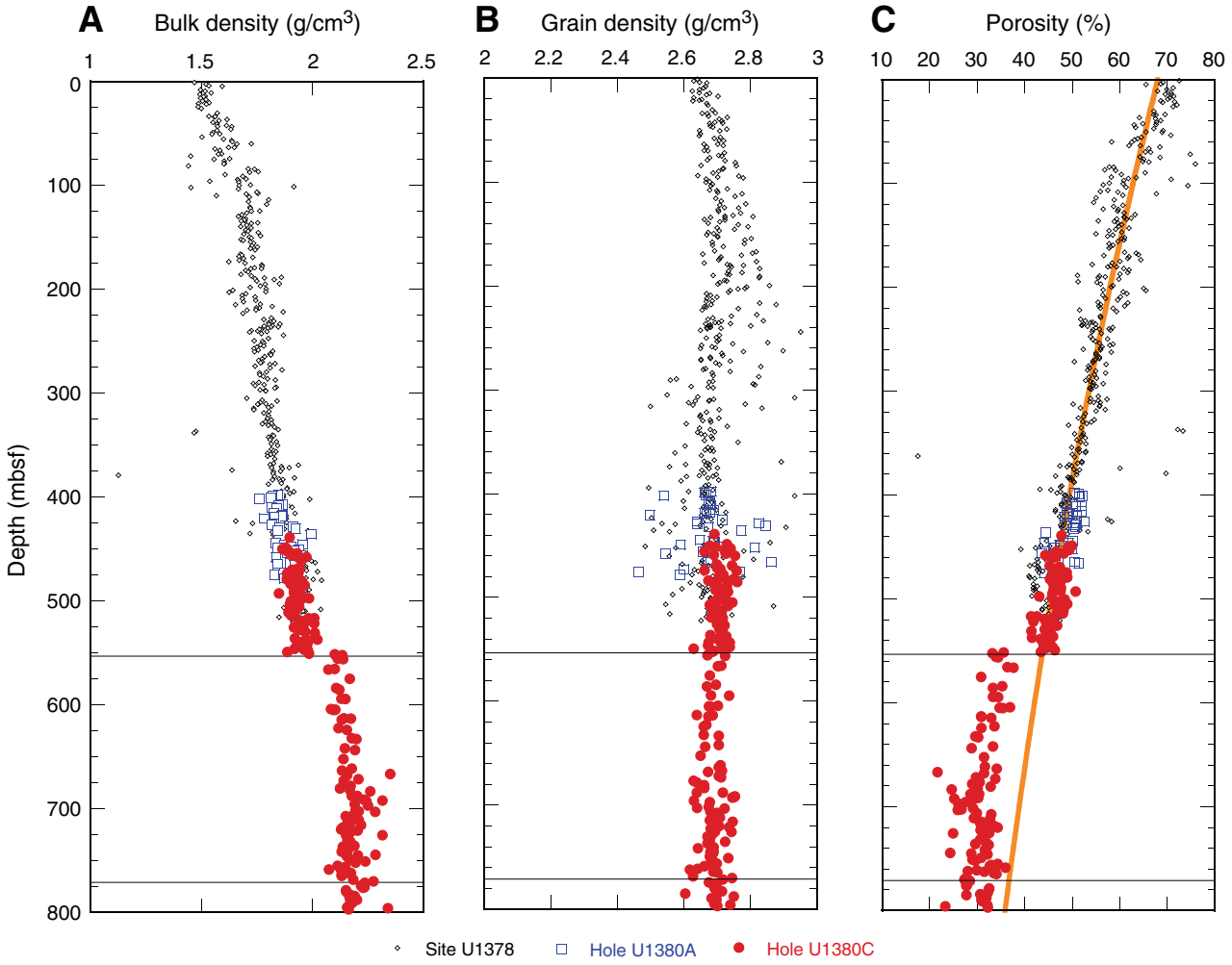

Figure F26. Magnetic susceptibility profiles, Site U1380. WRMSL = Whole-Round Multisensor Logger, SHMSL = Section Half Multisensor Logger. Horizontal lines = lithostratigraphic unit boundaries.

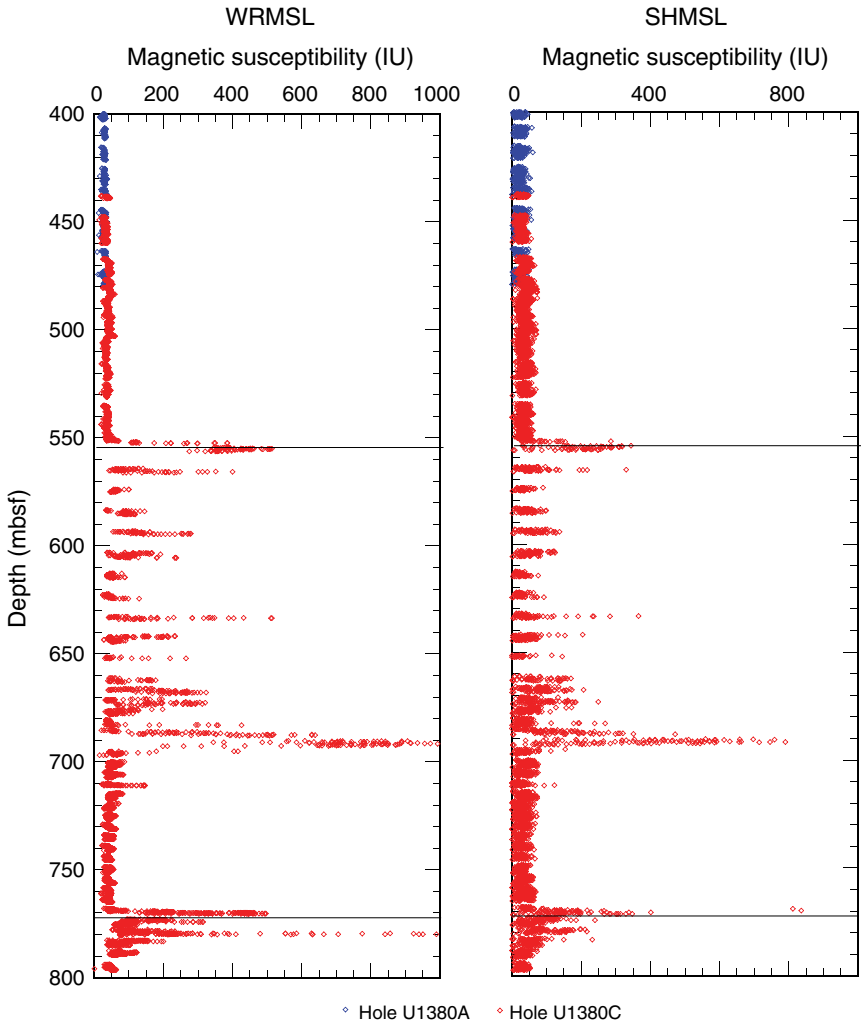

Figure F27. Downhole profiles for natural gamma radiation (NGR), Sites U1380 (red) and U1378 (blue). Horizontal lines = lithostratigraphic unit boundaries.

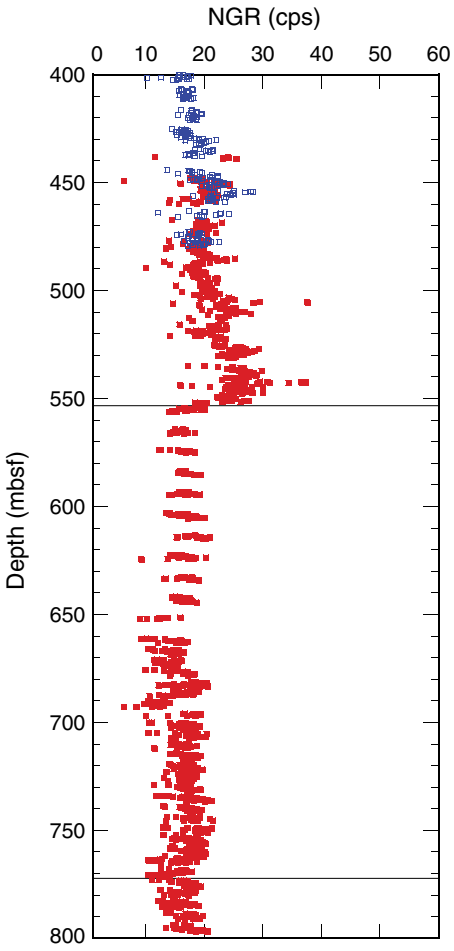

Figure F28. *P*-wave velocity measured on split cores, Site U1380 and Hole U1378B. Horizontal lines = lithostratigraphic unit boundaries.

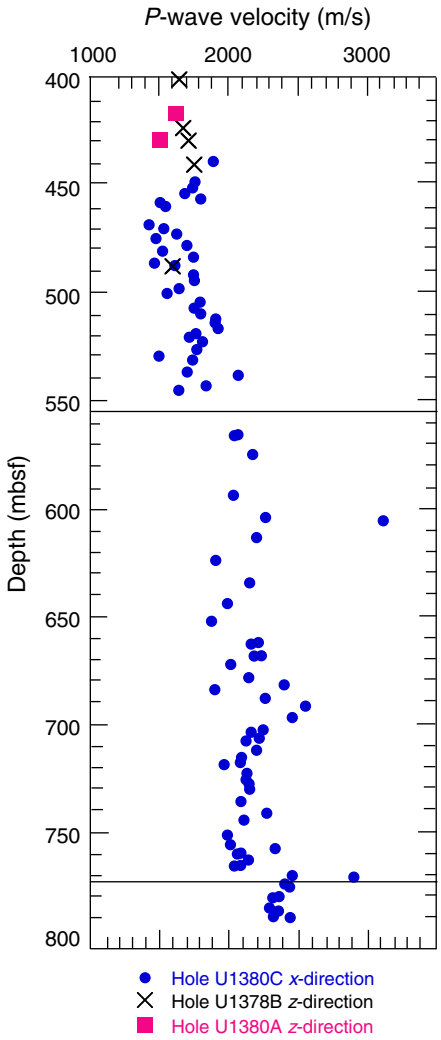

Figure F29. Thermal data, Sites U1380 and U1378. **A.** Thermal conductivity showing best-fit line (TC = 0.72 + 0.00093*x*; *R* = 0.88). **B.** Equilibrium temperatures. Estimated temperature based on linear fit to thermal conductivity (T) or precise thermal conductivity value (T2) with equilibrium temperature. Horizontal lines = lithostratigraphic unit boundaries.

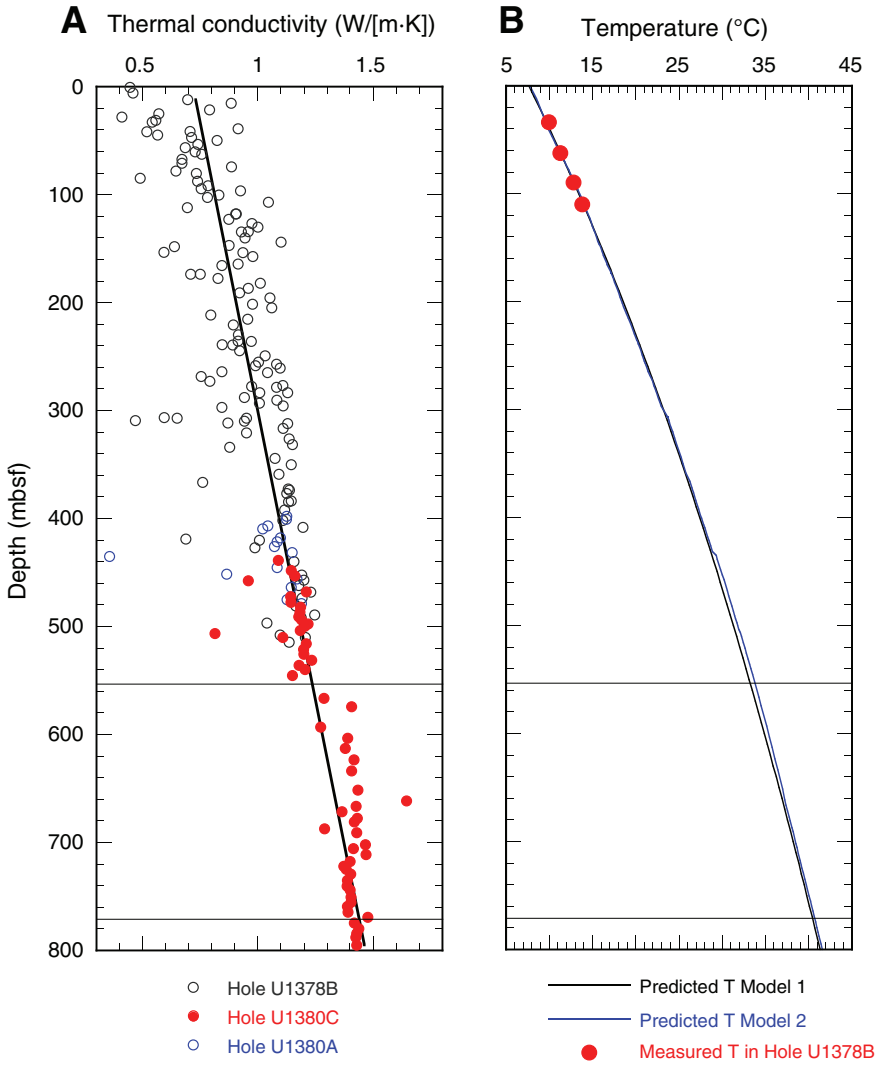

Figure F30. Compressive strength measured using a needle penetrometer, Site U1380. Horizontal lines = lithostratigraphic unit boundaries.

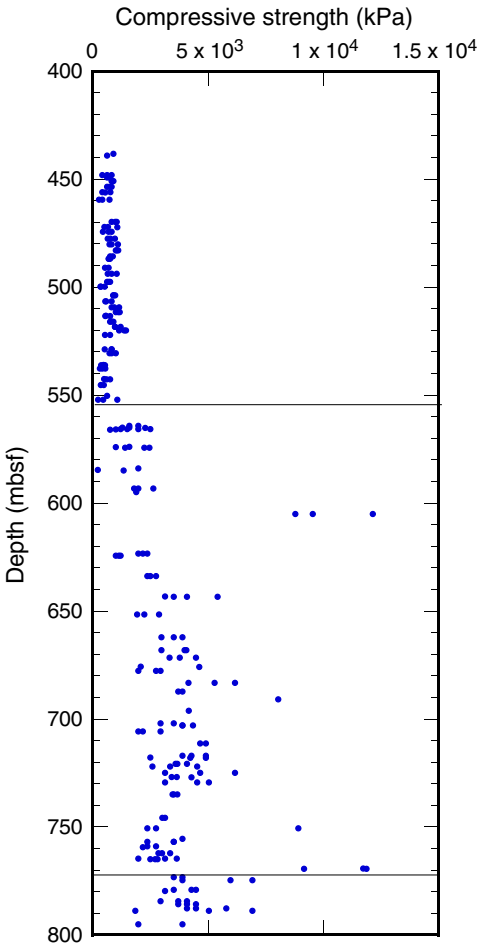

Figure F31. Reflectance L*, a*, and b* profiles, Site U1380. Horizontal lines = lithostratigraphic unit boundaries.

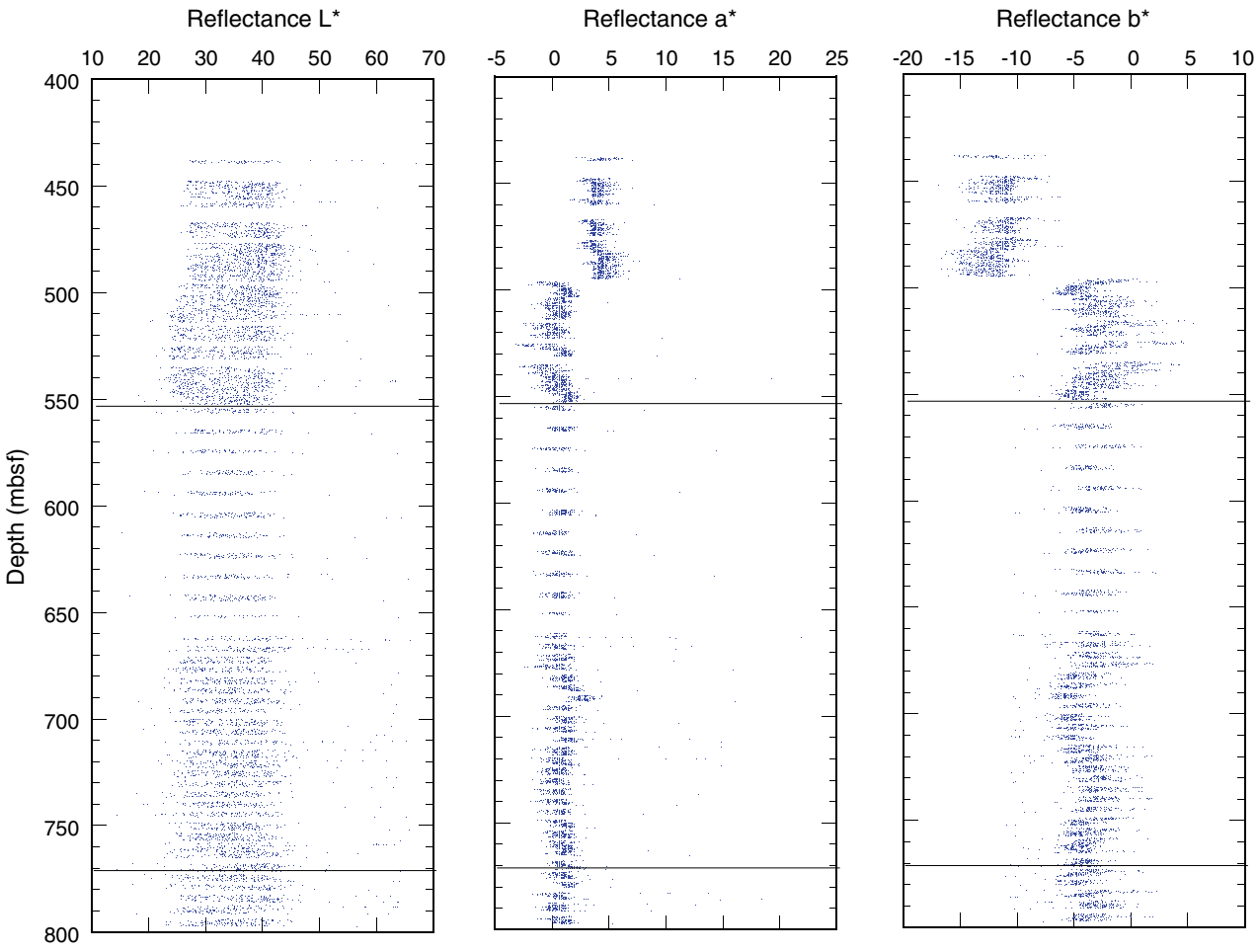

Figure F32. Core-seismic correlation, Site U1380. Dashed lines indicate horizons of core-seismic integration. NGR = natural gamma radiation.

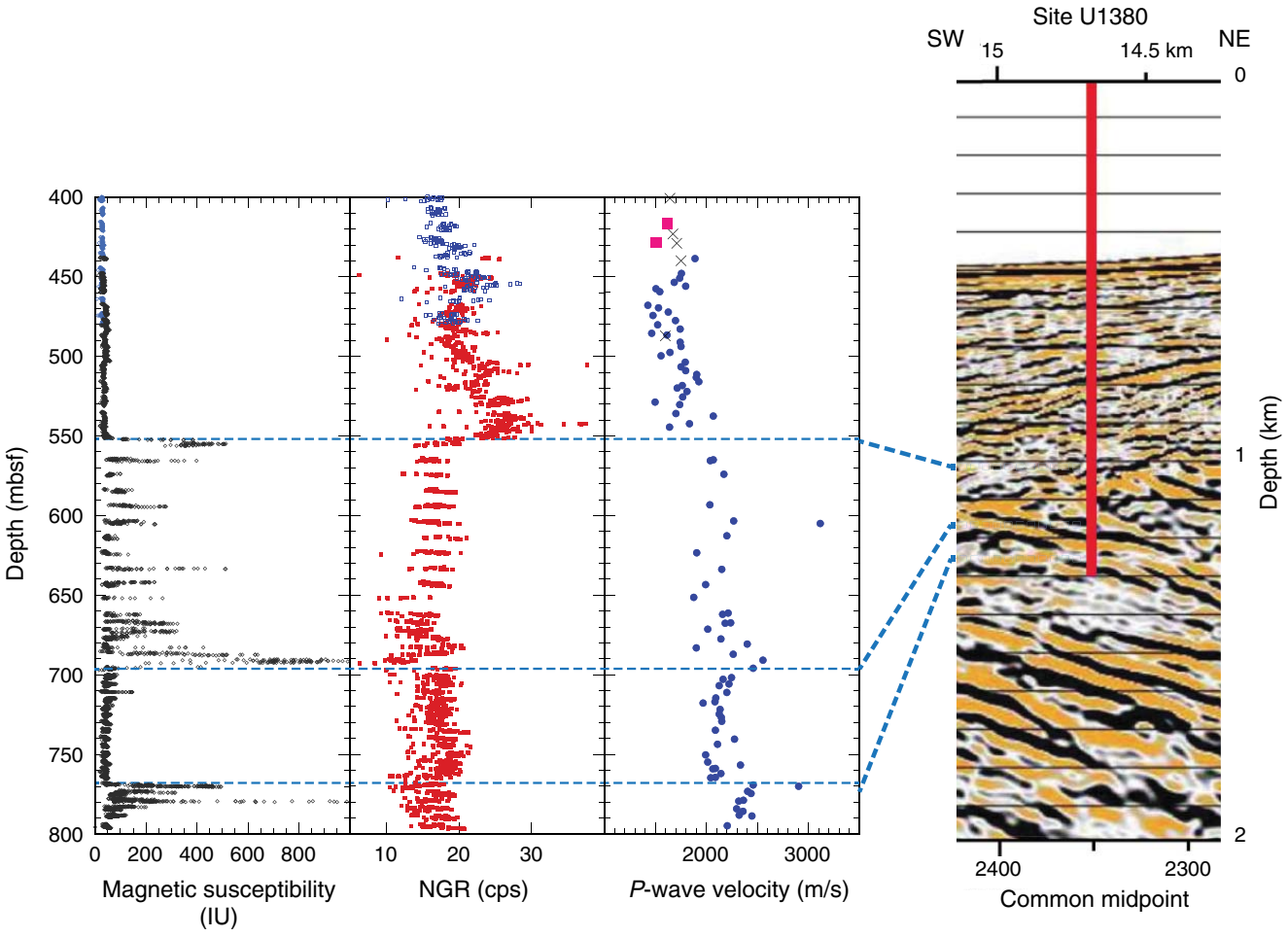

Figure F33. Paleomagnetic measurements on sediment archive-half sections: NRM intensity and inclination after 0 and 30 mT AF demagnetization, Hole U1380C.

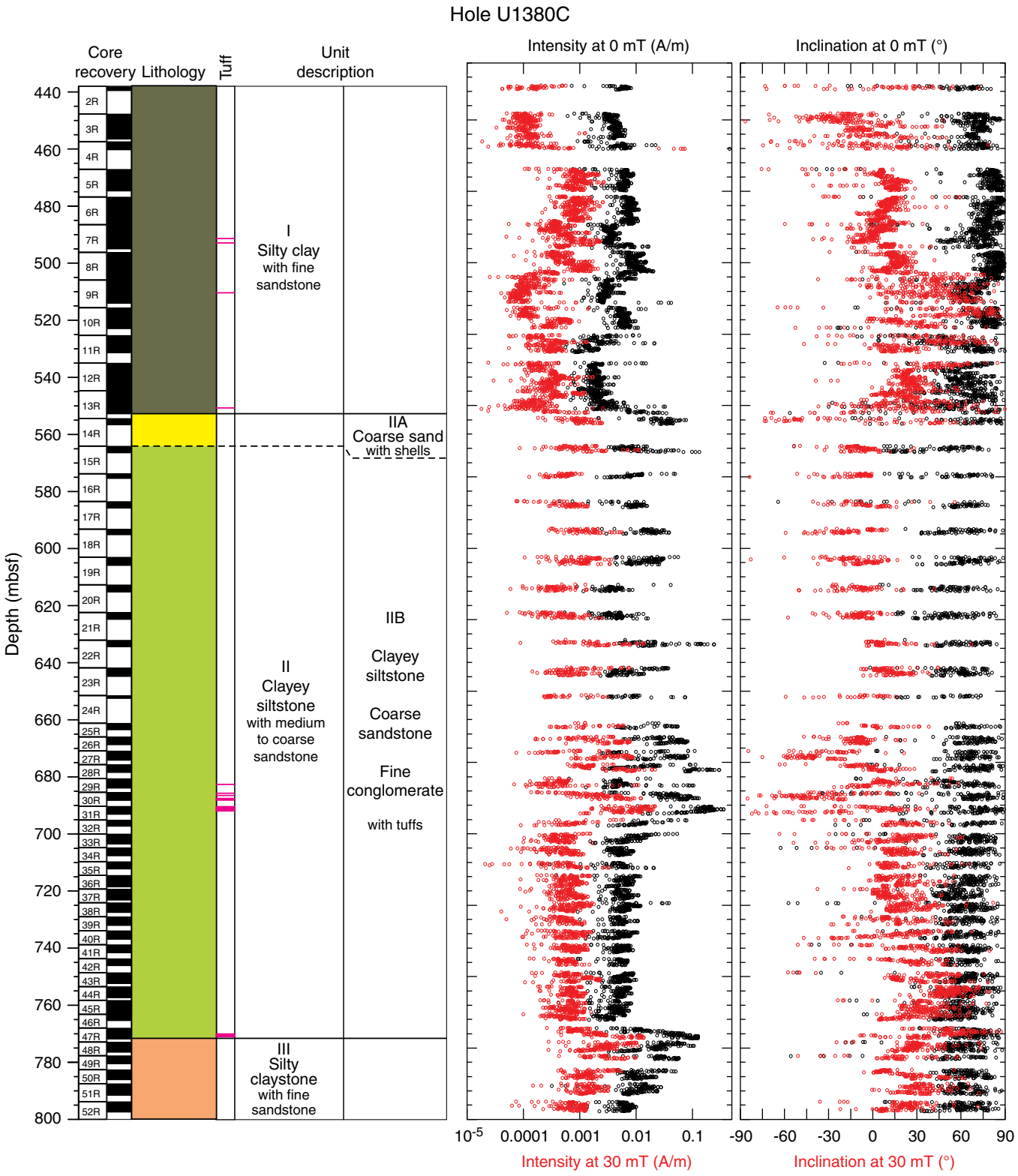

Figure F34. Vector end-point diagrams (Zijderveld, 1967). **A.** Stepwise AF demagnetization displaying a reversed vertical component of magnetization caused by drilling that is removed after 5 mT demagnetization (Sample 344-U1380C-51R-2W, 65–67 cm). **B, C.** Pass-through measurements of Section 344-U1380C-51R-2A corresponding to the depth of the discrete sample in A, showing the removal of a normal vertical component of magnetization, suggesting the sample in A has an orientation error of 180° in the *z*-direction. Open and solid squares = projection of the magnetization vector end-points onto the vertical and horizontal planes, respectively. NRM = natural remanent magnetization.

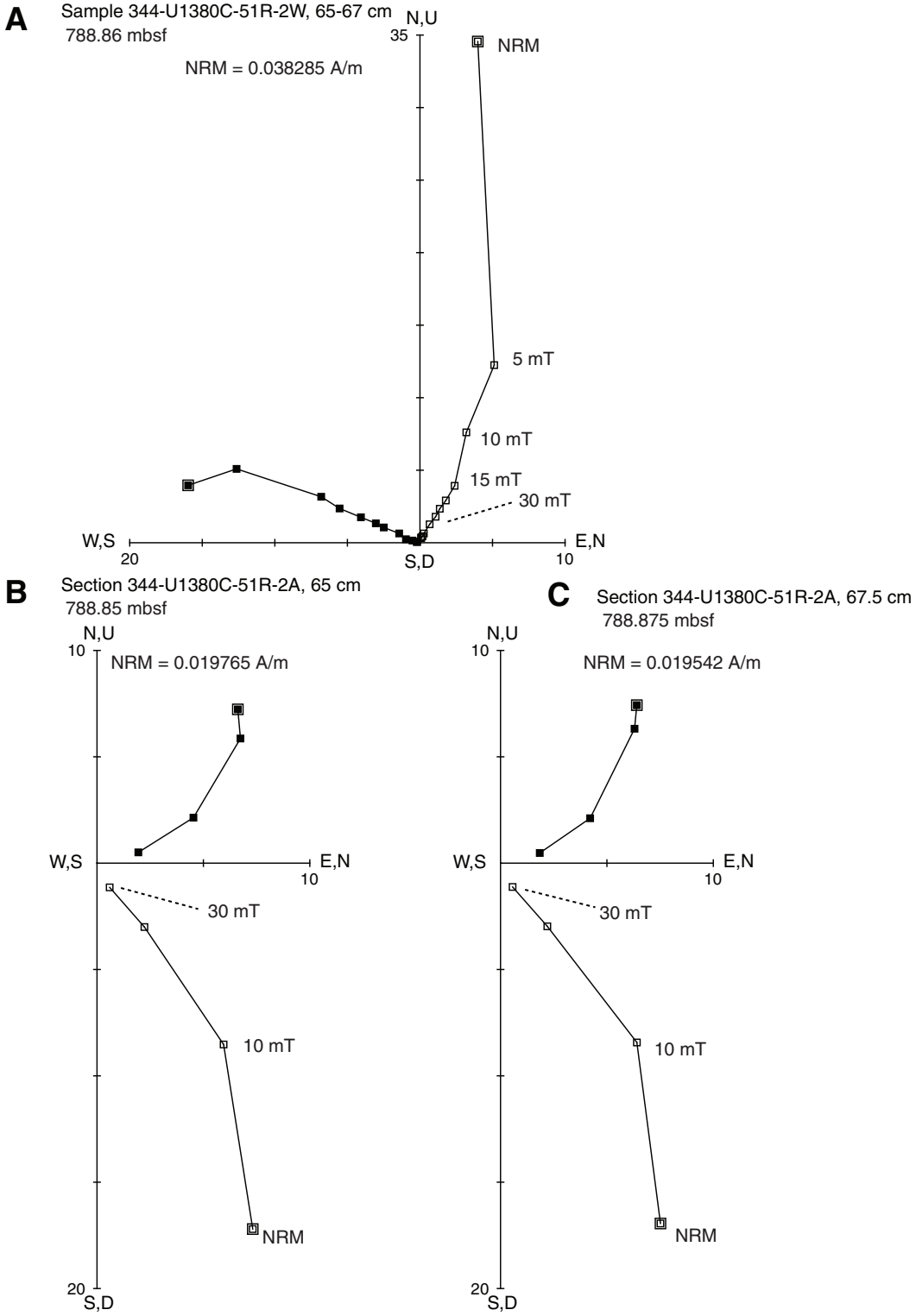

Figure F35. Vector plots for representative samples, Hole U1380C. **A, B.** AF demagnetization showing (A) normal polarity of ChRM (Sample 344-U1380C-43R-2W, 38-40 cm) and (B) reversed polarity of ChRM (Sample 344-U1380C-19R-3W, 8-10 cm). **C, D.** Thermal demagnetization showing (C) normal polarity of ChRM (Sample 344-U1380C-26R-1W, 61-63 cm) and (D) reversed polarity of ChRM (Sample 344-U1380C-21R-1W, 101-103 cm). Open and solid squares = projection of the magnetization vector end-points onto the vertical and horizontal planes, respectively. NRM = natural remanent magnetization.

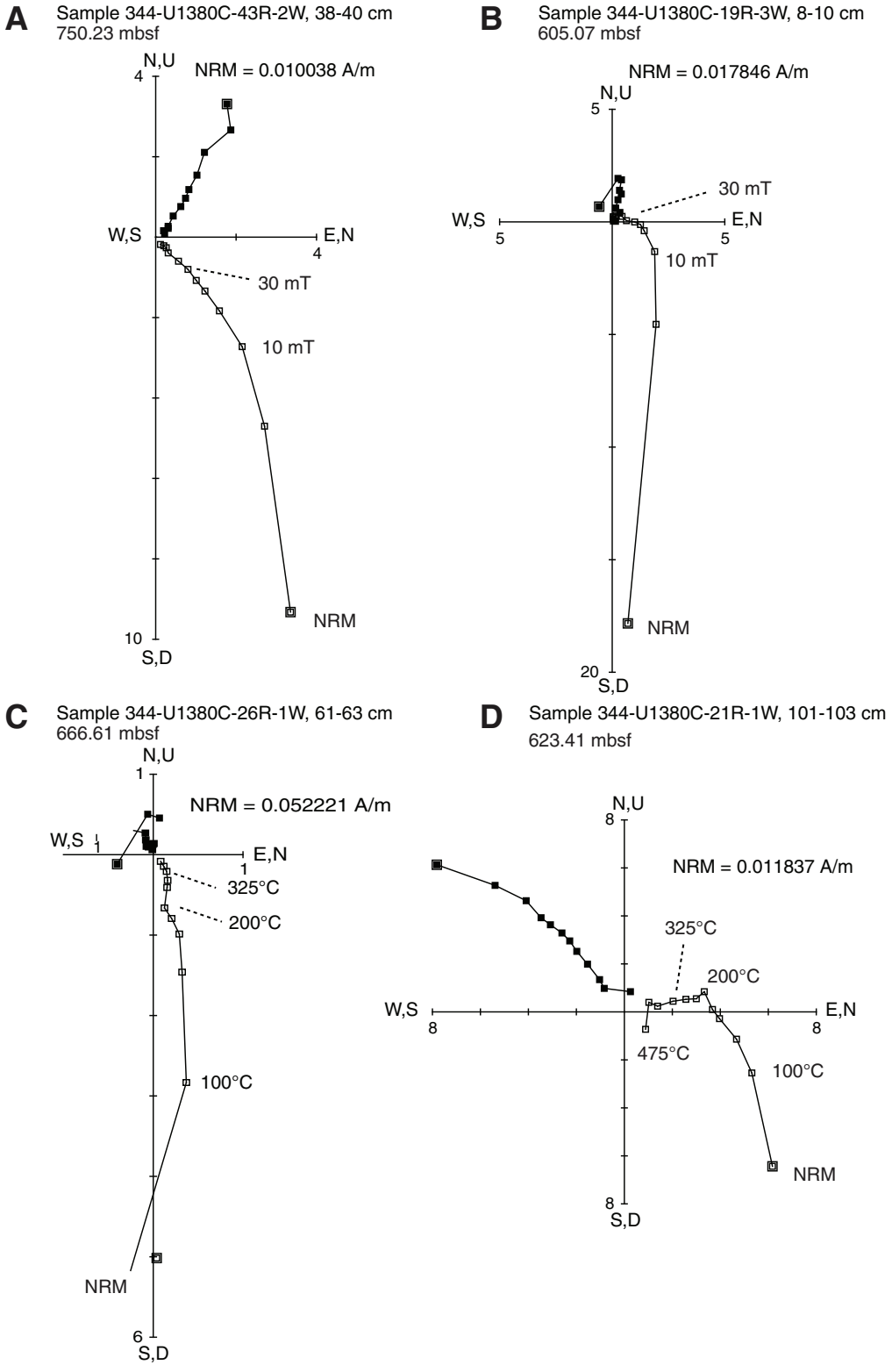

Figure F36. Discrete sample magnetostratigraphy, Hole U1380C. Results of characteristic remanence (ChRM) were determined by principal component analysis (Kirschvink, 1980). Black = normal polarity, white = reversed polarity, gray = uncertain polarity.

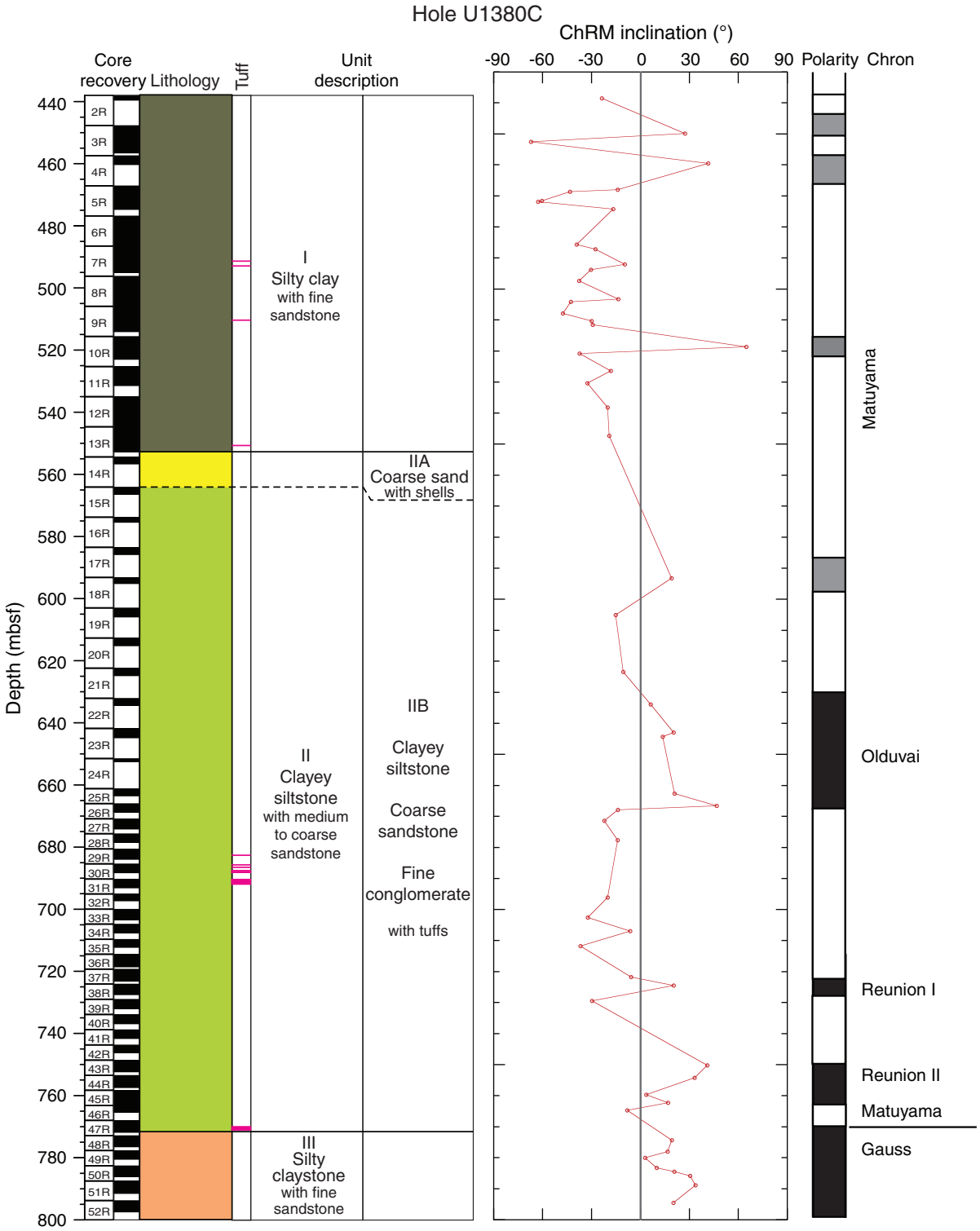

Table T1. Site U1380 coring summary. (Continued on next page.)

Hole U1380C
Latitude: 8°35.9879′N
Longitude: 84°4.3918′W
Time on hole (h): 393.5 (16.4 days)
Seafloor (drill pipe measurement from rig floor, m DRF): 513.6
Distance between rig floor and sea level (m): 10.9
Water depth (drill pipe measurement from sea level, m): 502.7
Total penetration (drilling depth below seafloor, m DSF): 800.0
Total length of cored section (m): 362.0
Total core recovered (m): 202.4
Core recovery (%): 56
Total number of cores: 51

Core	Date (2012)	Time UTC (h)	Depth DSF (m) Top of cored interval	Depth DSF (m) Bottom of cored interval	Interval advanced (m)	Depth CSF (m) Top of cored interval	Depth CSF (m) Bottom of cored interval	Length of core recovered (m)	Recovery (%)
344-U1380C-									
11			*****Drilled from 0.0 to 47.9 m DSF*****						
12			*****Drilled from 47.9 to 438.0 m DSF*****						
2R	8 Nov	0130	438.00	447.70	9.7	438.00	439.52	1.52	16
3R	8 Nov	0305	447.70	457.40	9.7	447.70	456.50	8.80	91
4R	8 Nov	0440	457.40	467.10	9.7	457.40	460.26	2.86	29
5R	8 Nov	0610	467.10	476.80	9.7	467.10	474.68	7.58	78
6R	8 Nov	0740	476.80	486.50	9.7	476.80	486.65	9.85	102
7R	8 Nov	0900	486.50	496.20	9.7	486.50	494.98	8.48	87
8R	8 Nov	1015	496.20	505.90	9.7	496.20	506.05	9.85	102
9R	8 Nov	1145	505.90	515.60	9.7	505.90	514.05	8.15	84
10R	8 Nov	1315	515.60	525.30	9.7	515.60	522.94	7.34	76
11R	8 Nov	1450	525.30	535.00	9.7	525.30	531.41	6.11	63
12R	8 Nov	1610	535.00	544.70	9.7	535.00	544.99	9.99	103
13R	8 Nov	1730	544.70	554.40	9.7	544.70	552.77	8.07	83
14R	8 Nov	1925	554.40	564.10	9.7	554.40	556.62	2.22	23
15R	8 Nov	2050	564.10	573.80	9.7	564.10	566.43	2.33	24
16R	8 Nov	2215	573.80	583.50	9.7	573.80	575.42	1.62	17
17R	9 Nov	0120	583.50	593.20	9.7	583.50	585.80	2.30	24
18R	9 Nov	0255	593.20	603.00	9.8	593.20	595.14	1.94	20
19R	9 Nov	0425	603.00	612.70	9.7	603.00	605.89	2.89	30
20R	9 Nov	0615	612.70	622.40	9.7	612.70	615.15	2.45	25
21R	9 Nov	0750	622.40	632.10	9.7	622.40	624.80	2.40	25
22R	9 Nov	0925	632.10	641.80	9.7	632.10	634.41	2.31	24
23R	9 Nov	1115	641.80	651.50	9.7	641.80	644.79	2.99	31
24R	9 Nov	1250	651.50	661.20	9.7	651.50	652.49	0.99	10
25R	9 Nov	1400	661.20	666.00	4.8	661.20	663.48	2.28	48
26R	9 Nov	1530	666.00	670.90	4.9	666.00	668.72	2.72	56
27R	9 Nov	1650	670.90	675.70	4.8	670.90	674.15	3.25	68
28R	9 Nov	1810	675.70	680.60	4.9	675.70	678.44	2.74	56
29R	9 Nov	2005	680.60	685.40	4.8	680.60	683.91	3.31	69
30R	9 Nov	2140	685.40	690.30	4.9	685.40	688.25	2.85	58
31R	9 Nov	2350	690.30	695.10	4.8	690.30	693.10	2.80	58
32R	10 Nov	0130	695.10	700.00	4.9	695.10	697.29	2.19	45
33R	10 Nov	0310	700.00	704.80	4.8	700.00	703.42	3.42	71
34R	10 Nov	0440	704.80	709.70	4.9	704.80	707.65	2.85	58
35R	10 Nov	0630	709.70	714.50	4.8	709.70	712.26	2.56	53
36R	10 Nov	0830	714.50	719.30	4.8	714.50	718.53	4.03	84
37R	10 Nov	1000	719.30	724.10	4.8	719.30	723.15	3.85	80
38R	10 Nov	1125	724.10	729.00	4.9	724.10	727.49	3.39	69
39R	10 Nov	1255	729.00	733.90	4.9	729.00	732.05	3.05	62
40R	10 Nov	1410	733.90	738.80	4.9	733.90	736.86	2.96	60
41R	10 Nov	1540	738.80	743.70	4.9	738.80	741.59	2.79	57
42R	10 Nov	1700	743.70	748.60	4.9	743.70	746.14	2.44	50
43R	10 Nov	1835	748.60	753.50	4.9	748.60	752.32	3.72	76
44R	10 Nov	2005	753.50	758.30	4.8	753.50	757.39	3.89	81
45R	10 Nov	2155	758.30	763.20	4.9	758.30	763.08	4.78	98
46R	10 Nov	2345	763.20	768.00	4.8	763.20	765.38	2.18	45
47R	11 Nov	0150	768.00	772.90	4.9	768.00	771.81	3.81	78
48R	11 Nov	0315	772.90	777.70	4.8	772.90	776.47	3.57	74
49R	11 Nov	0435	777.70	782.60	4.9	777.70	780.48	2.78	57
50R	11 Nov	0605	782.60	787.50	4.9	782.60	786.11	3.51	72
51R	11 Nov	0745	787.50	793.80	6.3	787.50	791.47	3.97	63

Table T1 (continued).

Core	Date (2012)	Time UTC (h)	Depth DSF (m) Top of cored interval	Depth DSF (m) Bottom of cored interval	Interval advanced (m)	Depth CSF (m) Top of cored interval	Depth CSF (m) Bottom of cored interval	Length of core recovered (m)	Recovery (%)
52R	11 Nov	0950	793.80	800.00	6.2	793.80	797.42	3.62	58
			Hole U1380C totals:		800.0			202.35	56

DSF = drilling depth below seafloor, CSF = core depth below seafloor. R = rotary core barrel core, numeric core type = drilled interval.

Table T2. Summary of Hole U1380C lithologic units.

Unit	Subunit	Top depth (mbsf)	Core, section, interval (cm)	Bottom depth (mbsf)	Core, section, interval (cm)	Unit thickness (m)	Major lithology
			344-U1380C-		344-U1380C-		
I		438.0	2R-1, 0	552.72	13R-7, 55	114.72	Silty clay with fine sandstone
II	IIA	552.72	13R-7, 55	564.10	14R-CC, 20	11.38	Coarse shell-rich sand/sandstone
	IIB	564.10	15R-1, 0	771.62	47R-3, 106	207.52	Clayey siltstone with medium to coarse sandstone
III		771.62	47R-CC, 0	800	52R-CC, 19	29.44	Silty claystone with fine sandstone

Table T3. Calcareous nannofossil faunal distribution, Hole U1380C. (Continued on next page.)

Core, section, interval (cm)	Depth (mbsf) Top	Depth (mbsf) Bottom	Preservation	Group abundance	*Calcidiscus leptoporus*	*Coccolithus pelagicus*	*Discoaster asymmetricus*	*Discoaster brouweri*	*Discoaster pentaradiatus*	*Discoaster* sp.	*Gephyrocapsa* (<4 µm)	*Gephyrocapsa* (>4 µm)	*Gephyrocapsa muellerae*	*Gephyrocapsa oceanica*	*Gephyrocapsa sinuosa*	*Helicosphaera carteri*	*Helicosphaera sellii*	*Helicosphaera* sp.	*Helicosphaera* spp.	*Helicosphaera wallichii*	*Pontosphaera discopora*	*Pontosphaera multipora*	*Pseudoemiliania lacunosa*	*Syracosphaera histrica*	*Syracosphaera pulchra*	Comments
344-U1380C-																										
2R-CC	439.47	439.52	M	C	R	R					Freq	Freq	Freq	Freq				Freq				R				Altered coccoliths
3R-CC	456.45	456.50	P	F		R								R				R							R	Altered coccoliths
4R-CC	460.21	460.26	P	F	R						R					R			Freq		R					
5R-CC	474.63	474.68	P	R	R						R								Freq		R		R			
6R-CC	486.60	486.65	P	F	R	Freq					R				Freq	R			Freq	R	R		R	R		
7R-CC	494.93	494.98	P	R							R								R							
8R-CC	506.00	506.05	G	C	Freq	Freq					Freq				Freq	Freq	R		Freq	Freq			R	R		
9R-CC	513.98	514.03	M	F	R	R		R			Freq				Freq		R		R				R			
10R-CC	522.89	522.94	P	R	R	R					R							R								
11R-CC	531.34	531.39	M	F	R	R		Freq			Freq				Freq								R			
12R-CC	544.94	544.99	M	F	R	R					Freq				R								R			
13R-CC	552.72	552.77	G	F		R		R			Freq							R								
14R-CC	556.57	556.62	P	R						R	R						R	R					R			
15R-CC	566.38	566.41	M	R				R			Freq															
16R-CC	575.36	575.41	P	R				R			R															
17R-CC	585.60	585.65	M	F	R	Freq		Freq		C	Freq					R	R		R							
18R-CC	595.08	595.13		B																						
19R-CC	605.84	605.89	P	R	R			R			Freq							R								
20R-CC	615.10	615.15	M	F	Freq	Freq		R			C				Freq			R			R					
21R-CC	624.75	624.80	M	R	R						C				R				R		R					
22R-CC	634.35	634.40	M	R				R		R	Freq				R			R					R			
23R-CC	644.73	644.78	P	R						R					R											
24R-CC	652.29	652.34	M	R				R			Freq										R		R			
25R-CC	663.46	663.48	M	R	R	R				R	R										R					
26R-CC	668.66	668.68	G	C	Freq	Freq		R		R	C				Freq		Freq	Freq						R		
27R-CC	674.11	674.15	P	R				R			R										R					
28R-CC	678.31	678.36	M	R	R	R					C					R		R					R			
29R-CC, 14–20	683.71	683.76	M	F	R			R		R	C						R	R								
30R-CC	688.19	688.24	M	F				R			Freq				Freq		R									
31R-2, 74–75	692.54	692.55	P	R	R						R															
31R-CC	693.04	693.09		B																						
32R-CC	697.24	697.29	P	R	R			R			R															
33R-CC	703.37	703.42	M	R	R						R															
34R-CC	707.60	707.65	M	F				R			C						R	R								
35R-CC	712.21	712.26	P	R				R			Freq															
36R-CC	718.45	718.50	P	R		R				R	R															
37R-CC	723.10	723.15	P	R				R			Freq							R								
38R-CC	727.44	727.49	M	R			R			R	Freq				R				R				R			
39R-CC	731.98	732.03	P	R	R						R															
40R-CC	736.81	736.86	P	R	R		R	R		R	Freq				R											
41R-CC	741.53	741.58		B																						
42R-CC	746.07	746.12	P	R							R															
43R-CC	752.27	752.32	P	R	R			R			R															

Table T3 (continued).

Core, section, interval (cm)	Depth (mbsf) Top	Depth (mbsf) Bottom	Preservation	Group abundance	*Calcidiscus leptoporus*	*Coccolithus pelagicus*	*Discoaster asymmetricus*	*Discoaster brouweri*	*Discoaster pentaradiatus*	*Discoaster* sp.	*Gephyrocapsa* (<4 µm)	*Gephyrocapsa* (>4 µm)	*Gephyrocapsa muellerae*	*Gephyrocapsa oceanica*	*Gephyrocapsa sinuosa*	*Helicosphaera carteri*	*Helicosphaera sellii*	*Helicosphaera* sp.	*Helicosphaera* spp.	*Helicosphaera wallichii*	*Pontosphaera discopora*	*Pontosphaera multipora*	*Pseudoemiliania lacunosa*	*Syracosphaera histrica*	*Syracosphaera pulchra*	Comments
44R-CC	757.34	757.39	M	R				R			Freq					R		R					R			
45R-CC	763.03	763.08	P	R	R						Freq							R					R			
46R-CC	765.33	765.38	P	R				R		R	R															
47R-CC	771.76	771.81	P	R						R	R															
48R-CC	776.41	776.46	P	R						R	R							R								
49R-CC	780.43	780.48	M	R	R	R		R		R	Freq				R		R	R								
50R-CC	785.97	786.02	P	R				R		R	Freq							R					R			
51R-CC	791.41	791.46	M	F	R			R	R	Freq	Freq						R	R			R		R			
52R-CC	797.36	797.41	P	R			R	R		R	R															

Preservation: G = good, M = moderate, P = poor. Abundance: C = common, Freq = frequent, F = few, R = rare, B = barren.

Table T4. Benthic foraminiferal faunal counts, Hole U1380C. (Continued on next page.)

Core, section, interval (cm)	Depth (mbsf) Top	Depth (mbsf) Bottom	Preservation	Group abundance	*Bolivina pseudoplicata*	*Brizalina argentea*	*Brizalina bicostata*	*Brizalina ordinaria*	*Brizalina spathulata*	*Brizalina* spp.	*Brizalina spissa*	*Brizalina subaenariensis*	*Bulimina costata*	*Bulimina marginata*	*Bulimina mexicana*	*Bulimina* sp.	*Buliminella* sp.	*Cassidulina carinata*	*Chilostomella oolina*	*Cibicides* sp.	*Cibicidoides pachyderma*	*Cibicidoides* sp.	*Dentalina* sp.	*Discorbinella bertheloti*	*Discorbinella* sp.	*Epistominella smithi*	*Epistominella* sp.	*Globobulimina affinis*	*Globobulimina auriculata*	*Globobulimina pacifica*	*Globobulimina* sp.	*Globocassidulina globosa*	*Globocassidulina obtusa*	*Globocassidulina* sp.	*Gyroidina* sp.	*Hansenisca altiformis*	*Hoeglundina elegans*	*Laevidentalina aphelis*	*Laevidentalina* sp.	*Lagena* sp.	*Laticarinina pauperata*	*Lenticulina gibba*	*Lenticulina* sp.	*Martinottiella* sp.	*Melonis affinis*	*Mucronina* sp.	*Nonion* spp.	*Nonionella basispinata*	*Oolina globosa*
344-U1380C-																																															
2R-CC	439.47	439.52	M	R				2	17	3	10	6						2	11		40	6				32		1	7				3	3		4						1				2		2
3R-CC	456.45	456.50	M	R				4	33	3	19			1					1		12					19			1						4												2
4R-CC	460.21	460.26	M	R		1	7	4	10	3	11	4		1					4		2				3	11	1	3	7				8	8		8				1					2	3	1	
5R-CC	474.63	474.68	M	R			7	2	10		8	1						2			12			1		14		1	1	1			2		23				1						2		
6R-CC	486.60	486.65	M	R			4	7	12	12	14			1					2							12		2					3	6		9				1		1				1	1	
7R-CC	494.93	494.98	M	R			10	3	1	6	7	2		2		1		9	1		4			1	1	15					2		12	3		25											
8R-CC	506.00	506.05	M	R				4	2	1	1							1			1				1	76							2	1	1	18			1	1							1
9R-CC	513.98	514.03	M	R					8	1						11					2					11	1				2			1		6											
10R-CC	522.89	522.94	P	R										1																	1									1							
11R-CC	531.34	531.39	P	R					32		6			2				8	6		1					16		3	10		2			3	5	1											
12R-CC	544.94	544.99	M	R	11				9	31	12			3				57			2				2	8	1						6	2	2										1		
13R-CC	552.72	552.77	P	R	2			2		1						1		3		2	3	1		18									1								1						
14R-CC	556.57	556.62	P	R					4	4										3	17			3		1															1						
15R-CC	566.38	566.41	P	R			4		6								1	11								2								2	2						1		1				
16R-CC	575.36	575.41	M	R					4									1			1					1					1			2	1						1						
17R-CC	585.74	585.79	M	R	3		2		48			2				2		8			18					2						1				9					2						
18R-CC	595.08	595.13	M	R																	1											1														
19R-CC	605.84	605.89	M	R																	1															1										
20R-CC	615.10	615.15	M	R					4									2			27					4	1							4		9				1		1				
21R-CC	624.75	624.80	M	R					31	9						4		8			21				1	3					1			2							2	5		1	6		
22R-CC	634.35	634.40	M	R					3			1		1							36		1	2										1		22	1	1		1		5		2				
23R-CC	644.73	644.78	M	P														11			2																				1						
24R-CC	652.29	652.34	M	R					7				1		1			5			26								1					6		29						5	5				
25R-CC	663.46	663.51	M	R			2	1	10					1					1															5		2				1					1		
26R-CC	668.66	668.68	M	R			1		1							1					11			1										13		38	1	2				7	5				
27R-CC	674.11	674.15	M	R	1				16									3			9	1		1										4		7						16	3				
28R-CC	678.31	678.31																									1								2											
29R-CC, 14–20	683.71	683.76	M	R	6		2		3					1				2			20			3		14								2		10						3	3			1		
31R-CC	693.04	693.09	M	P																									1												1					
32R-CC	697.24	697.29																																													
33R-CC	703.37	703.42	M	R					16									1																	7								10			
34R-CC	707.60	707.65	M	P			1		3									1			1													3												
35R-CC	712.21	712.26	M	P																																1											
36R-CC	718.45	718.50	M	P																																2						2	2				
37R-CC	723.10	723.15	M	P					8																													1								
38R-CC	727.44	727.49	M	R					3							1					9					8									7						8	3		1			
39R-CC	731.98	732.03	P	P	1								1			1					7		2	1										3		1					1	1					
40R-CC	736.81	736.86	M	P			1		7									1								8									2							1					
42R-CC	746.07	746.12			3				14	1											6					2								3							3						
43R-CC	752.27	752.32	P	P																	5			1		4								1							1	3					
44R-CC	757.34	757.39	P	P																	1				1																	1					
46R-CC	765.33	765.38	P	P																	11														15							1	2					
47R-CC	771.76	771.81	M	R																						2								1	1						1	1					
52R-CC	797.36	797.41	M	R												3					21	5																				6		2		2		

Preservation: M = moderate, P = poor. Abundance: R = rare, P = present.

Table T4 (continued).

Core, section, interval (cm)	Depth (mbsf) Top	Depth (mbsf) Bottom	Preservation	Abundance	*Oridorsalis umbonatus*	*Osangularia* sp.	*Parafrondicularia* sp.	*Planulina exorna*	*Planulina ornata*	*Plectofrondicularia* sp.	*Pullenia bulloides*	*Pyrgo murrhina*	*Pyrgo* sp.	*Pyrulina* sp.	*Quinqueloculina* sp.	*Rectuvigerina* sp.	*Scallopostoma ovicula*	*Siphonodosaria lepidula*	*Siphonodosaria* sp.	*Siphouvigerina ampullacea*	*Sphaeroidina bulloides*	*Spiroloculina depressa*	*Spirosigmoilina distorta*	*Spirosigmoilina pusilla*	*Spirosigmoilina tenuis*	*Stainforthia complanata*	*Stainforthia sandiegoensis*	*Stainforthia* sp.	*Stilostomella holoserica*	*Textularia* spp.	*Trifarina* sp.	*Triloculina* sp.	*Uvigerina auberiana*	*Uvigerina peregrina*	*Uvigerina rippensis*	*Uvigerina senticosa*	*Uvigerina* sp.	*Valvulineria glabra*	Others	Total
344-U1380C-																																							
2R-CC	439.47	439.52	M	R				1		3			3					1	2				1			3							18		2		2	1	190
3R-CC	456.45	456.50	M	R	1		1	4					2		2	1	1									8							35				1		155
4R-CC	460.21	460.26	M	R			6					1		1					2						1	10			1		1	1	16				3	4	150
5R-CC	474.63	474.68	M	R						1					1				3							5			2				26				1	6	133
6R-CC	486.60	486.65	M	R					1	3																1							16				4	3	116
7R-CC	494.93	494.98	M	R					3																1	6							22				6	5	148
8R-CC	506.00	506.05	M	R					8						1	1			1		2		1		2	2			1	3			41					1	176
9R-CC	513.98	514.03	M	R					2	3		2																					114				2		166
10R-CC	522.89	522.94	P	R																													22						25
11R-CC	531.34	531.39	P	R						2								4								7							23						135
12R-CC	544.94	544.99	M	R				1	1								1	1	1														15				2		170
13R-CC	552.72	552.77	P	R					2																					2			5				1		45
14R-CC	556.57	556.62	P	R					2												1				1														37
15R-CC	566.38	566.41	P	R																	1												14				1		47
16R-CC	575.36	575.41	M	R					1												9										2						3		27
17R-CC	585.74	585.79	M	R		2			5	1											1					8							13				1	1	129
18R-CC	595.08	595.13	M	R																																			2
19R-CC	605.84	605.89	M	R						1											1																		4
20R-CC	615.10	615.15	M	R					14	1																													69
21R-CC	624.75	624.80	M	R					3	1			1								7			2									5		2		1		116
22R-CC	634.35	634.40	M	R	2				9	1			1						2		8												9			9			118
23R-CC	644.73	644.78	M	P																	1																		15
24R-CC	652.29	652.34	M	R	2				2	2			1						1		5										2		2		5			1	109
25R-CC	663.46	663.51	M	R																					1	1					2								28
26R-CC	668.66	668.68	M	R					12	2			2		2						20											1	4				2	2	126
27R-CC	674.11	674.15	M	R	1				4	1			1												1								3			1		2	75
28R-CC	678.31	678.31							1																														4
29R-CC, 14–20	683.71	683.76	M	R					4	3	1				1						15								1	2		2	3	11		10	7			130
31R-CC	693.04	693.09	M	P								3																							1				6
32R-CC	697.24	697.29																																					0
33R-CC	703.37	703.42	M	R					6			11													2						3		9		1				66
34R-CC	707.60	707.65	M	P					1	1																1							6		2	1			21
35R-CC	712.21	712.26	M	P	1										2																								4
36R-CC	718.45	718.50	M	P		1						1																			1		3						12
37R-CC	723.10	723.15	M	P					1																														10
38R-CC	727.44	727.49	M	R	2								1					2			1	1									3		5		1				58
39R-CC	731.98	732.03	P	P	2				3				1								1						1						2					1	30
40R-CC	736.81	736.86	M	P					2																								4		3				29
42R-CC	746.07	746.12			1				3										1		1												12						50
43R-CC	752.27	752.32	P	P	6				1																								2		1	1			27
44R-CC	757.34	757.39	P	P																																			3
46R-CC	765.33	765.38	P	P									1								1										1		2						34
47R-CC	771.76	771.81	M	R	1								1																										8
52R-CC	797.36	797.41	M	R		1			6		7																						3				1		57

Table T5. Uncorrected pore fluid major element concentrations, Hole U1380C.

Core, section, interval (cm)	Depth (mbsf)	Volume (mL)	Salinity	pH	Alkalinity (mM)	SO_4 IC (mM)	Cl titr. (mM)	Cl IC (mM)	Br (mM)	Na (mM)	K (mM)	Ca (mM)	Mg (mM)	NH_4 (mM)
344-U1380C-														
3R-3, 114–144	451.94	25.0	24.0			1.63	390	388	1.35	325	6.18	8.2	20.3	4.45
3R-5, 112–150	454.70	3.0					390							
4R-1, 51–73	458.13	3.0	21.5			1.48	377	381	1.29					
5R-3, 107–137	470.67	15.0	22.5			1.99	390	391	1.28	316	5.92	9.1	18.8	4.26
5R-5, 86–116	472.90	11.0	22.5	8.0	6.76	2.40	387			340	7.04	10.0	20.6	3.65
6R-3, 122–152	481.25	11.5	21.5			1.33	384	385	1.32	314	5.86	9.9	17.0	4.17
6R-5, 120–150	483.97	11.5	21.5	8.2	4.53	2.19	388	392	1.29	329	6.25	10.6	18.4	4.23
7R-3, 120–150	491.00	11.5	22.0			3.52	389	396	1.25	323	5.72	12.1	19.1	3.71
7R-5, 87–107	493.40	14.0	22.5	8.1	3.56	3.42	393	404	1.27	328	5.89	12.1	18.0	4.25
8R-2, 116–146	499.12	12.5	22.5			2.91	386	393	1.26	316	5.20	12.3	17.1	3.77
8R-6, 107–137	504.91	11.0	22.0	8.3	1.80	1.89	383	391	1.29	320	5.36	13.3	15.2	3.72
9R-1, 102–132	507.22	14.5	22.0	8.2	2.30	3.77	401	387	1.28	334	5.61	13.9	16.4	3.55
9R-6, 79–109	513.28	10.0	22.5			1.68	383			309	4.90	14.4	13.3	3.23
10R-2, 35–65	517.25	13.5	22.5	8.2	1.93	2.91	398	403	1.32	329	5.53	14.9	14.7	3.47
10R-4, 53–78	519.53	10.5	22.5			1.48	380	380	1.30	302	4.75	14.7	11.6	3.49
10R-6, 64–90	521.93	18.5	22.0	8.4	1.58	1.63	385	375	1.27	308	4.71	15.6	11.8	3.72
11R-2, 59–89	526.87	17.0	21.5			1.38	382	388	1.30	307	4.25	17.0	11.5	3.20
11R-4, 87–117	529.54	15.0	22.0			3.01	387	386	1.24	316	4.66	16.7	11.7	3.08
12R-2, 79–113	537.55	4.5	22.0			2.09	386	394	1.29	317	4.22	19.4	10.3	2.87
12R-4, 78–108	539.58	19.0	22.5			3.26	392	397	1.25	319	4.08	20.2	11.6	2.84
12R-8, 62–92	543.72	17.5	22.5			3.57	388	396	1.24	325	4.20	20.6	9.6	3.07
13R-3, 50–80	548.02	14.5	21.5			1.58	381	385	1.28	312	3.86	21.3	7.8	2.97
13R-6, 58–88	551.90	12.5	22.0			1.28	390			316	3.85	22.8	7.3	3.00
14R-1, 127–142	555.82	2.0	21.0			1.22	377	379	1.31	310	3.43	22.8	5.5	
17R-1, 63–90	584.40	2.0	23.0			2.24	401	410	1.36	323	2.60	29.4	4.5	1.81
Drilling fluid			32.0	8.2	2.28	26.83	508	508	0.80	436	9.78	9.7	49.1	

IC = ion chromatograph, titr. = titration.

Table T6. Uncorrected pore fluid minor element concentrations, Hole U1380C.

Core, section, interval (cm)	Depth (mbsf)	B (μM)	Li (μM)	Sr (μM)	Ba (μM)	Mn (μM)	Si (μM)
344-U1380C-							
3R-3, 114–144	451.94	152	77.2	46.5	1.94	0.35	211
3R-5, 112–150	454.70	—	—	—	—	—	—
4R-1, 51–73	458.13	—	—	—	—	—	—
5R-3, 107–137	470.67	138	64.8	41.3	2.03	0.78	151
5R-5, 86–116	472.90	116	57.1	47.0	1.86	0.53	109
6R-3, 122–152	481.25	113	59.6	39.3	1.93	0.47	121
6R-5, 120–150	483.97	107	55.9	42.5	1.98	0.46	91.1
7R-3, 120–150	491.00	96	57.9	47.8	2.15	1.2	123
7R-5, 87–107	493.40	139	62.0	45.3	2.41	1.2	119
8R-2, 116–146	499.12	151	64.3	46.5	2.15	1.1	139
8R-6, 107–137	504.91	103	64.5	47.5	2.09	0.64	98.4
9R-1, 102–132	507.22	132	63.4	52.1	2.42	0.98	123
9R-6, 79–109	513.28	98	57.2	48.6	1.77	0.45	109
10R-2, 35–65	517.25	150	62.8	56.1	1.90	0.93	121
10R-4, 53–78	519.53	118	60.4	54.4	1.73	0.36	104
10R-6, 64–90	521.93	144	62.6	56.3	1.63	1.2	110
11R-2, 59–89	526.87	119	61.3	60.7	1.64	0.83	109
11R-4, 87–117	529.54	139	57.3	62.5	1.68	0.97	108
12R-2, 79–113	537.55	150	56.5	70.2	1.86	1.3	107
12R-4, 78–108	539.58	176	55.2	72.4	1.89	2.0	124
12R-8, 62–92	543.72	141	48.8	73.4	1.88	1.5	107
13R-3, 50–80	548.02	176	44.4	73.0	1.80	2.1	123
13R-6, 58–88	551.90	182	39.5	75.8	1.53	1.4	91.6
14R-1, 127–142	555.82	193	34.4	70.7	1.17	0.11	118
17R-1, 63–90	584.40	201	12.0	65.4	2.60	0.62	102
Drilling fluid		349	29.2	87.3	0.15	0	9.89

— = not measured.

Table T7. Sulfate-corrected pore fluid major element concentrations, Hole U1380C.

Core, section, interval (cm)	Depth (mbsf)	Volume (mL)	Salinity	Alkalinity (mM)	Cl titr. (mM)	Cl IC (mM)	Br (mM)	Na (mM)	K (mM)	Ca (mM)	Mg (mM)	NH_4 (mM)	Na/Cl
344-U1380C-													
3R-3, 114–144	451.94	25.0	23.5		383	380	1.44	318	5.95	8.14	18.5	4.74	0.832
3R-5, 112–150	454.70	3.0			390								
4R-1, 51–73	458.13	3.0	20.9		369	373	1.37						
5R-3, 107–137	470.67	15.0	21.7		380	381	1.38	307	5.62	9.10	16.4	4.60	0.807
5R-5, 86–116	472.90	11.0	21.6	7.20	375			330	6.77	10.0	17.8	4.01	0.881
6R-3, 122–152	481.25	11.5	21.0		378	378	1.39	308	5.65	9.95	15.3	4.39	0.816
6R-5, 120–150	483.97	11.5	20.6	4.73	377	381	1.41	319	5.93	10.7	15.6	4.60	0.847
7R-3, 120–150	491.00	11.5	20.5		371	379	1.44	306	5.11	12.5	14.6	4.27	0.825
7R-5, 87–107	493.40	14.0	21.1	3.75	376	389	1.46	313	5.32	12.4	13.4	4.87	0.831
8R-2, 116–146	499.12	12.5	21.3		371	379	1.41	302	4.65	12.6	13.2	4.23	0.813
8R-6, 107–137	504.91	11.0	21.2	1.76	374	382	1.39	311	5.03	13.5	12.7	4.00	0.833
9R-1, 102–132	507.22	14.5	20.4	2.30	384	368	1.49	317	4.92	14.6	11.1	4.13	0.827
9R-6, 79–109	513.28	10.0	21.9		375			300	4.57	14.7	10.9	3.45	0.801
10R-2, 35–65	517.25	13.5	21.3	1.89	384	391	1.48	316	5.01	15.5	10.5	3.89	0.823
10R-4, 53–78	519.53	10.5	21.9		372	373	1.37	294	4.45	15.0	9.39	3.69	0.790
10R-6, 64–90	521.93	18.5	21.4	1.53	377	367	1.36	300	4.38	16.0	9.34	3.96	0.795
11R-2, 59–89	526.87	17.0	20.9		376	382	1.37	300	3.95	17.4	9.43	3.37	0.799
11R-4, 87–117	529.54	15.0	20.7		372	371	1.40	301	4.01	17.6	7.02	3.47	0.809
12R-2, 79–113	537.55	4.5	21.2		376	384	1.40	307	3.75	20.2	7.06	3.11	0.817
12R-4, 78–108	539.58	19.0	21.2		376	381	1.42	302	3.30	21.7	6.36	3.23	0.803
12R-8, 62–92	543.72	17.5	21.0		369	379	1.43	308	3.35	22.2	3.54	3.54	0.834
13R-3, 50–80	548.02	14.5	20.8		373	377	1.36	304	3.49	22.0	5.20	3.16	0.814
13R-6, 58–88	551.90	12.5	21.5		384			310	3.55	23.4	5.18	3.15	0.809
14R-1, 127–142	555.82	2.0	20.5		371	373	1.38	304	3.12	23.4	3.41		0.822
17R-1, 63–90	584.40	2.0	22.2		392	401	1.49	313	1.94	31.2	0.401	1.98	0.800

Titr. = titration, IC = ion chromatograph.

Table T8. Pore fluid minor element concentrations corrected for drilling fluid contamination, Hole U1380C.

Core, section, interval (cm)	Depth (mbsf)	B (μM)	Li (μM)	Sr (μM)	Ba (μM)	Mn (μM)	Si (μM)
344-U1380C-							
3R-3, 114–144	451.94	139	80.3	43.8	2.06	0.38	224
3R-5, 112–150	454.70	—	—	—	—	—	—
4R-1, 51–73	458.13	—	—	—	—	—	—
5R-3, 107–137	470.67	121	67.6	37.6	2.18	0.84	163
5R-5, 86–116	472.90	92.8	59.8	43.0	2.03	0.58	120
6R-3, 122–152	481.25	101	61.2	36.9	2.02	0.49	127
6R-5, 120–150	483.97	85.0	58.3	38.5	2.14	0.50	99.2
7R-3, 120–150	491.00	57.7	62.3	41.8	2.45	1.4	142
7R-5, 87–107	493.40	109	66.8	39.2	2.74	1.4	137
8R-2, 116–146	499.12	127	68.6	41.6	2.39	1.2	156
8R-6, 107–137	504.91	84.4	67.2	44.5	2.24	0.69	106
9R-1, 102–132	507.22	96.3	69.0	46.3	2.79	1.1	143
9R-6, 79–109	513.28	80.8	59.1	46.0	1.88	0.48	116
10R-2, 35–65	517.25	125	66.9	52.3	2.11	1.0	136
10R-4, 53–78	519.53	104	62.2	52.4	1.82	0.38	110
10R-6, 64–90	521.93	131	64.7	54.3	1.73	1.3	117
11R-2, 59–89	526.87	106	63.0	59.2	1.72	0.88	115
11R-4, 87–117	529.54	113	60.9	59.3	1.88	1.1	122
12R-2, 79–113	537.55	133	58.8	68.7	2.01	1.4	116
12R-4, 78–108	539.58	152	58.8	70.3	2.13	2.3	141
12R-8, 62–92	543.72	109	51.8	71.2	2.15	1.7	123
13R-3, 50–80	548.02	166	45.3	72.1	1.90	2.3	131
13R-6, 58–88	551.90	173	40.0	75.3	1.60	1.5	96.2
14R-1, 127–142	555.82	185	34.7	69.9	1.22	0.11	124
17R-1, 63–90	584.40	187	10.4	63.4	2.82	0.68	112

— = not measured.

Table T9. Inorganic carbon (IC), total carbon (TC), total organic carbon (TOC), and calcium carbonate, Hole U1380C.

Core, section	Depth (mbsf)	IC (wt%)	TC (wt%)	TOC (wt%)	$CaCO_3$ (wt%)
344-U1380C-					
3R-3W	451.62	0.178	1.00	0.822	1.48
3R-4W	453.05	0.229	1.26	1.03	1.91
3R-5W	454.25	0.564	1.78	1.22	4.70
4R-1W	457.89	0.402	1.41	1.01	3.36
5R-3W	470.22	0.338	1.56	1.22	2.82
5R-5W	472.53	0.409	1.38	0.971	3.41
6R-3	481.21	0.528	1.57	1.04	4.40
6R-5	483.98	0.471	1.76	1.29	3.93
7R-5W	493.00	0.180	0.930	0.750	1.50
8R-2W	498.61	0.636	1.71	1.07	5.31
8R-6W	504.72	0.831	1.89	1.06	6.93
9R-1W	506.88	0.740	2.11	1.37	6.17
9R-3W	509.41	0.440	1.65	1.21	3.67
9R-4W	510.91	0.411	1.70	1.29	3.43
9R-6W	512.90	0.603	1.81	1.21	5.03
10R-1W	515.84	0.553	1.67	1.12	4.61
10R-4W	519.26	0.104	1.32	1.22	0.870
10R-6W	521.64	0.699	1.67	0.971	5.83
11R-2W	526.55	0.607	1.63	1.02	5.06
11R-2W	526.65	0.459	1.51	1.05	3.83
11R-4W	529.15	1.11	2.47	1.36	9.29
12R-2W	537.25	1.21	2.38	1.17	10.1
12R-4W	539.39	0.427	1.51	1.08	3.56
12R-7W	542.29	0.927	1.95	1.02	7.73
12R-8W	543.65	1.55	2.58	1.03	12.9
13R-3W	547.67	0.702	1.73	1.03	5.86
13R-6	552.15	0.924	1.62	0.696	7.71
14R-1	555.65	1.07	1.70	0.626	8.96
14R-2W	556.29	0.757	1.10	0.343	6.31
15R-2W	566.11	0.398	0.920	0.522	3.32
17R-1W	584.11	0.430	1.07	0.640	3.58
20R-1W	613.03	0.531	1.25	0.719	4.43
20R-2W	613.42	0.314	0.690	0.376	2.62
21R-1W	623.08	0.538	1.11	0.572	4.49
22R-1W	632.31	0.299	1.17	0.871	2.49
22R-2W	632.67	0.469	1.01	0.541	3.91
25R-1W	661.47	0.428	0.950	0.522	3.57
25R-2W	662.38	0.538	1.02	0.482	4.49
27R-1W	671.39	0.316	0.600	0.284	2.63
29R-1W	680.96	0.550	1.19	0.640	4.59
30R-1	685.97	0.279	0.730	0.451	2.33
31R-1W	690.61	0.911	1.28	0.369	7.60
32R-1W	695.53	0.360	0.750	0.390	3.00
33R-2W	701.63	0.620	1.05	0.430	5.17
34R-2W	707.03	0.672	1.40	0.728	5.61
35R-1W	709.81	0.451	0.830	0.379	3.76
35R-3W	711.67	0.346	0.720	0.374	2.89
36R-2W	716.50	0.421	0.940	0.519	3.51
37R-1W	720.10	0.558	1.37	0.812	4.65
37R-3	722.90	0.411	0.740	0.329	3.43
38R-1W	724.30	0.412	1.02	0.608	3.43
40R-3W	736.04	0.390	0.820	0.430	3.25
41R-2W	741.44	0.308	0.740	0.432	2.57
42R-2W	744.80	0.386	1.01	0.624	3.22
43R-1W	748.77	0.274	0.470	0.196	2.29
43R-2W	750.13	0.471	1.07	0.599	3.93
44R-2W	755.08	0.506	1.26	0.754	4.22
45R-4W	761.52	0.321	0.780	0.459	2.68
47R-3W	771.35	0.977	1.11	0.133	8.15
46R-2W	764.82	0.442	0.960	0.518	3.69
48R-3W	776.24	0.359	0.530	0.171	3.00
48R-2W	775.65	0.570	0.760	0.190	4.75
49R-1W	778.54	0.508	0.880	0.372	4.23
50R-1W	783.51	0.520	1.02	0.500	4.34
51R-3W	790.64	0.482	0.990	0.508	4.02

Table T10. Concentrations of hydrocarbon in headspace gas samples, Hole U1380C.

Core, section, interval (cm)	Depth (mbsf)	Methane (ppmv)	Ethane (ppmv)	Propane (ppmv)	*n*-Butane (ppmv)	*iso*-Pentane (ppmv)	C_1/C_{2+}
344-U1380C-							
3R-4, 0–5	451.94	4,630	10.9	2.60	0.933	3.16	163
3R-6, 0–5	454.70	1,990	6.79	ND	0.634	2.40	104
4R-2, 0–5	458.13	7,930	14.0	8.59	1.07	4.30	199
5R-4, 0–5	470.67	7,900	9.20	4.43	ND	2.13	356
5R-6, 0–5	472.90	9,300	11.1	1.11	ND	2.71	348
6R-4, 0–5	481.32	8,590	9.77	ND	ND	2.72	374
6R-6, 0–5	484.08	7,070	7.59	1.24	ND	1.85	386
7R-4, 0–5	491.00	7,200	8.96	0.33	ND	2.22	355
7R-6, 0–5	493.40	9,020	10.5	ND	ND	3.24	358
8R-3, 0–5	499.16	6,190	10.3	ND	ND	3.32	233
8R-7, 0–5	505.04	8,810	32.0	3.94	0.855	3.81	250
9R-2, 0–5	507.22	9,280	15.4	ND	0.896	4.22	245
9R-7, 0–5	513.28	7,020	14.5	ND	1.46	5.77	162
10R-3, 0–5	517.25	9,050	16.3	29.6	0.807	2.75	333
10R-5, 0–5	519.53	6,390	11.6	1.97	0.705	2.62	264
10R-7, 0–5	521.93	6,660	12.8	3.27	0.746	2.79	238
11R-3, 0–5	526.99	9,430	17.1	ND	0.765	2.82	299
11R-5, 0–5	529.54	5,450	12.3	ND	ND	2.44	247
12R-3, 0–5	537.63	10,900	16.8	ND	0.680	3.43	379
12R-5, 0–5	539.72	10,000	17.4	ND	ND	2.92	337
12R-9, 0–5	543.98	8,980	15.4	ND	ND	3.45	350
13R-4, 0–5	548.02	11,800	21.1	ND	ND	2.26	395
13R-7, 0–5	551.90	17,500	13.2	ND	ND	0.984	1,040
14R-2, 0–5	555.82	4,930	2.91	ND	ND	ND	1,414
15R-2, 0–5	565.60	8,150	8.86	ND	ND	ND	853
16R-1, 0–5	573.80	9,460	10.1	ND	ND	ND	860
17R-2, 0–5	584.40	10,600	10.8	ND	ND	ND	892
18R-1, 0–5	593.20	22,200	23.8	ND	ND	ND	900
19R-1, 0–5	603.00	5,650	6.97	ND	ND	ND	767
20R-2, 0–5	613.35	4,380	5.33	ND	ND	ND	723
21R-2, 0–5	623.72	908	0.00	ND	ND	ND	—
22R-2, 0–5	632.67	3,410	5.34	ND	ND	ND	604
23R-2, 0–5	643.17	3,200	2.66	ND	ND	ND	1,072
24R-1, 0–5	651.50	4,870	11.06	ND	ND	ND	423
25R-2, 0–5	662.08	3,300	4.18	ND	ND	ND	745
26R-1, 145–150	667.45	7,650	10.4	ND	ND	ND	656
27R-2, 0–5	672.43	3,000	2.06	ND	ND	ND	1,518
28R-2, 0–5	677.20	5,480	2.45	ND	ND	ND	2,078
29R-1, 32–37	680.92	3,660	6.48	ND	ND	ND	507
30R-2, 0–5	686.60	5,400	6.78	ND	ND	ND	685
31R-2, 106–111	692.86	43,200	16.0	ND	ND	ND	2,612
32R-2, 0–5	695.87	9,350	10.5	ND	ND	ND	769
33R-2, 0–5	701.54	17,400	11.8	ND	ND	ND	1,265
34R-2, 0–5	706.13	4,720	9.26	ND	ND	ND	453
35R-2, 0–5	710.08	6,320	8.80	ND	ND	ND	711
36R-2, 0–5	716.00	6,600	7.22	ND	ND	ND	807
37R-2, 0–5	720.35	7,700	6.70	ND	ND	ND	1,068
38R-2, 0–5	725.60	9,980	3.57	ND	ND	ND	2,501
39R-2, 101–106	731.01	6,460	5.74	ND	ND	ND	970
40R-2, 0–5	735.02	7,770	9.44	ND	ND	ND	740
41R-2, 0–5	740.30	14,900	14.7	ND	ND	ND	873
42R-3, 0–5	745.55	5,190	7.09	ND	ND	ND	649
43R-2, 0–5	749.85	5,410	4.22	ND	ND	ND	1,144
44R-2, 0–5	755.00	5,720	12.4	ND	ND	ND	422
45R-4, 94–99	762.01	6,880	4.00	ND	ND	ND	1,503
46R-2, 0–5	764.67	6,440	3.77	ND	ND	ND	1,387
47R-3, 0–5	770.56	7,720	5.40	ND	ND	ND	1,279
48R-3, 0–5	775.69	5,790	4.34	ND	ND	ND	1,183
49R-1, 0–5	777.70	12,900	11.3	ND	ND	ND	976
50R-1, 129–134	783.89	20,100	10.5	ND	ND	ND	1,595
51R-2, 0–5	788.20	13,200	7.43	ND	ND	ND	1,484
52R-2, 0–5	795.30	23,400	10.4	ND	ND	ND	1,821

— = incalculable. ND = not detected.